Modelling the Phase Transition Dynamics of Supercritical Carbon Dioxide in Converging Diverging Nozzles for Carbon Sequestration Applications

ME EFPT MSc Thesis (ME55035)

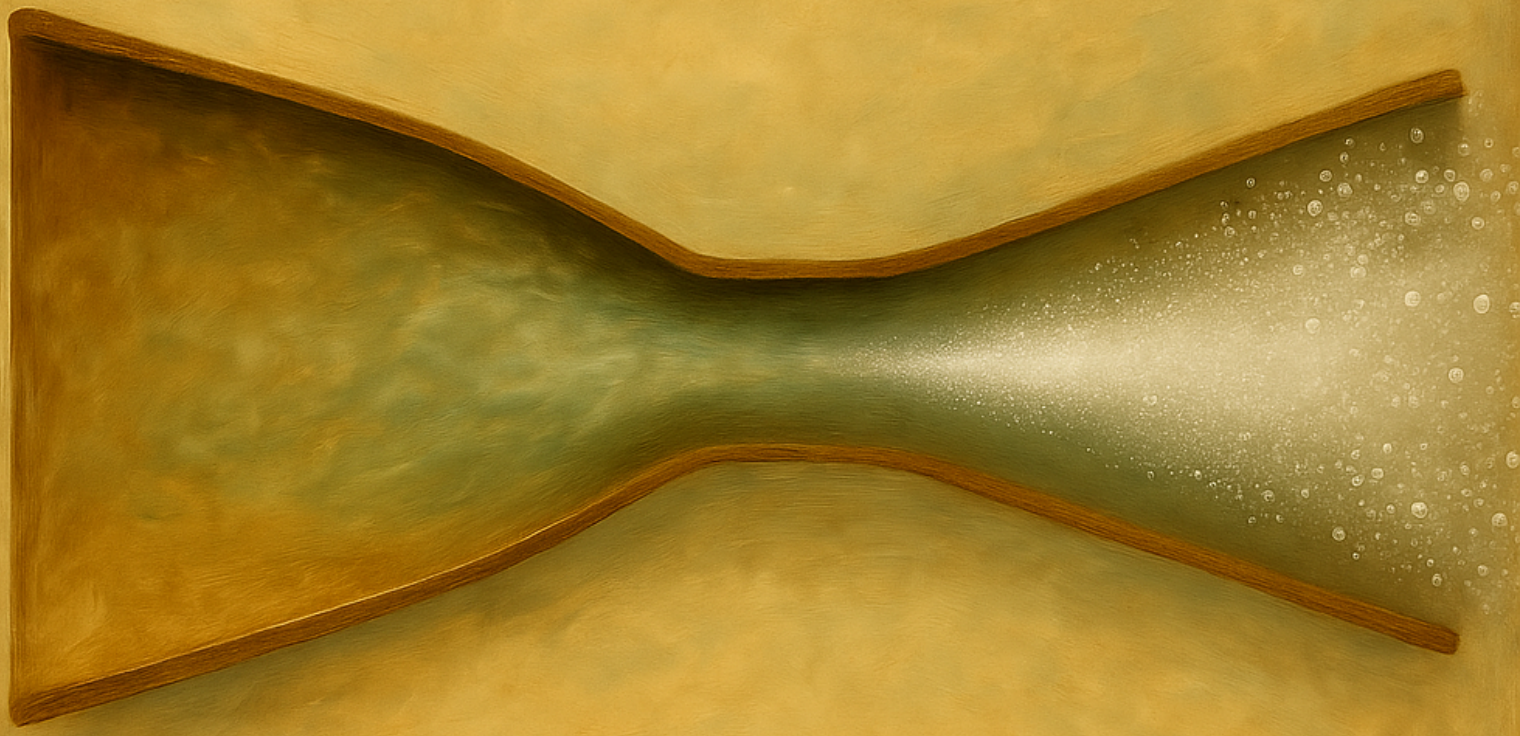

Raagul Arumugam Sureshkumar

TU Delft

TNO
INNOVATION FOR LIFE

Modelling the Phase Transition Dynamics of Supercritical Carbon Dioxide in Converging-Diverging Nozzles for Carbon Sequestration Applications

Report - ME EFPT MSc Thesis (ME55035)

by

Raagul Arumugam Sureshkumar

to obtain the degree of Master of Science

at the Delft University of Technology,

to be defended publicly on Thursday - August 21, 2025 at 02:00 PM.

Student number:	5960541	
Project duration:	October 1, 2024 – July 31, 2025	
Thesis committee:	Prof.Dr. Rene Pecnik	TU Delft, Supervisor
	Dr.ir. Wim-Paul Breugem	TU Delft, Supervisor
	Dr. Aris Twerda	TNO, Supervisor
	Dr.ir. Mathieu Pourquié	TU Delft

This thesis is confidential and cannot be made public until August 21, 2025.

Cover:	Generated using Sora
Style:	TU Delft Report Style, with modifications by Daan Zwaneveld

TU Delft

Preface

I express my deepest gratitude to the **Heat Transfer & Fluid Dynamics** group at **TNO** for trusting me with and offering this thesis internship opportunity. The ten months of internship have been an incredible learning experience and have left a lasting positive impact on me. My heartfelt thanks to **Dr. Aris Twerda** for being an exceptional mentor, for generously sharing valuable technical insights from your rich experience and for the unwavering support throughout this journey. I am also grateful to **Dr. Stefan Belfroid** and **Dr. Dries van Nimwegen** for their constructive feedback during the weekly meetings, which greatly helped in aligning my work in the right direction. Many thanks to **Dr. Aviral Rajora** for the invaluable time and guidance you provided in familiarising me with the simulation framework and helping me get up to speed. My sincere thanks to all my colleagues at TNO for being so welcoming and supportive throughout this journey.

I am profoundly thankful to my supervisors, **Dr. Rene Pecnik** and **Dr.ir. Wim-Paul Breugem** at **TU Delft** for the sustained support throughout the progress update meetings and for the meticulous and constructive reviews, which have been invaluable in refining and shaping this work. I am grateful to the **Process & Energy** department for providing an enriching and inspiring academic experience over the past two years.

I am deeply grateful to **Darshan Raju**, for generously sharing valuable research insights that were of immense support to my work and to **Teja Donnupudi** for providing timely guidance at critical junctures, even amidst a busy schedule.

Sridharan, thank you for being not only an amazing friend but also a great mentor and a pillar of support, standing by me at every step of this journey, right from the initial application to the completion of this thesis. **To all my friends at Delft**, thank you for making this city feel like home and for all the beautiful memories, which I will cherish forever.

Appa, Amma, Grandparents, Mathav and my extended family, thank you for your unconditional love and unwavering support throughout these years. Your sacrifices and encouragement have made it possible for me to pursue this passion and no words can truly convey the depth of my gratitude for all that you have done. To all who have, in any way, contributed to the completion of this thesis, I extend my heartfelt thanks.

Seyyaamal seydha udhavikku vaiyagamum
vaanagamum aatral aridhu.

For help rendered unasked, even the whole world and heaven are not adequate recompense.

- Thirukkural

Raagul Arumugam Sureshkumar
Delft, August 2025

Summary

Aligned with the European Union's ambition to achieve net zero greenhouse gas emissions by 2050, a plethora of carbon dioxide abatement technologies have been developed and are being deployed in industries. Among these, Carbon Capture, Utilisation and Storage (CCUS) technologies play a pivotal role in decarbonising hard-to-abate sectors where CO_2 emissions are inevitable. Geological carbon storage is an effective option for long-term CO_2 sequestration, especially in regions with substantial sub-surface capacity for large scale permanent storage.

In this technology, transporting CO_2 in supercritical conditions enhances the transport efficiency due to its high density and low viscosity. However, the rapid depressurization of supercritical CO_2 across control valves prior to injection into geological storage reservoirs can trigger complex phase transition phenomena, including flashing, cavitation and shock wave formation. This study investigates the expansion dynamics of supercritical CO_2 using converging-diverging nozzles, as a simplified yet representative geometry for control valves, to develop modelling strategies for the depressurization process.

Building on earlier work, the simulation framework was upgraded from modelling dense liquid phase to supercritical phase which is characterised by the sharp thermodynamic gradients in the vicinity of the critical point. This study employs the Span-Wagner Equation of State to capture the real gas behaviour of carbon dioxide. The implementation in *Ansys Fluent* was carried out via a non-uniform lookup table, refined near the critical region and smoothed using the Savitzky-Golay filter to ensure numerical robustness of the solver while preserving the thermodynamic fidelity. Simulations were performed using the Mixture multiphase model in *Ansys Fluent*, incorporating interphase slip velocity to represent mechanical non-equilibrium between the liquid and vapour phases. The phase transition was modelled using the Zwart-Gerber-Belamri (ZGB) cavitation framework tuned to simulate the non-equilibrium phase transition behaviour. Both quasi-one-dimensional and two-dimensional simulations were performed and the results were validated against experimental data from converging-diverging nozzle studies.

The results highlight the significance of metastable effects, sensitivity to cavitation model coefficients and the necessity of incorporating slip velocity between phases to accurately capture the phase transition behaviour. While the quasi-1D simulations provide qualitative trends, 2D simulations resulted in better agreement with the experiments. Overall, this study establishes a scalable and robust simulation framework for modelling the depressurization behaviour of supercritical CO_2, which can be extended to complex geometries such as control valves used in CCS infrastructure.

Contents

Nomenclature

Abbreviations

Abbreviation	Definition
AAPD	Absolute Average Percentage Deviation
CCS	Carbon Capture and Storage
CFD	Computational Fluid Dynamics
CNT	Classical Nucleation Theory
CO_2	Carbon Dioxide
CSS	Continuum Surface Stress
CSF	Continuum Surface Force
D-HEM	Delayed Homogeneous Equilibrium Model
D-HRM	Delayed Homogeneous Relaxation Model
DES	Detached Eddy Simulation
DNS	Direct Numerical Simulation
ECCSEL	European Carbon Dioxide Capture and Storage Laboratory Infrastructure
EMT	Enhanced Mass Transfer
EOS	Equation of State
ETS	Emissions Trading System
EU	European Union
HEM	Homogeneous Equilibrium Model
HFM	Homogeneous Flashing Model
HRM	Homogeneous Relaxation Model
IHE	Isentropic Homogeneous Equilibrium
IPCC	Intergovernmental Panel on Climate Change
LES	Large Eddy Simulation
LUT	Lookup Tables
NEM	Non-Homogeneous Equilibrium Model
NIST	National Institute of Standards and Technology
P_c	Critical Pressure
PRESTO!	PREssure STaggering Option
P-T	Pressure–Temperature
QSS	Quasi-Symmetric Sampling
RANS	Reynolds-Averaged Navier–Stokes
RCSG	Rijswijk Centre for Sustainable Geo-energy
REFPROP	REFerence fluid PROPerties

Abbreviation	Definition
RMS	Root Mean Square
RSM	Reynolds Stress Model
SAS	Scale-Adaptive Simulation
SGF	Savitzky–Golay Filter
SHL	Super Heat Limit
SST	Shear Stress Transport
SW EoS	Span-Wagner Equation of State
T_c	Critical Temperature
TNO	Nederlandse Organisatie voor Toegepast Natuurwetenschappelijk Onderzoek
UDF	User Defined Function
UDRGM	User Defined Real Gas Model
VCC	Vapour Compression Cycle
VOF	Volume of Fluid
ZGB	Zwart–Gerber–Belamri

Symbols

Symbol	Definition	Unit
A	Cross-sectional area	[m^2]
a	Speed of sound	[m/s]
C_p	Specific heat capacity at constant pressure	[J/(kg·K)]
CO_2	Carbon dioxide	[-]
D_H	Hydraulic diameter	[m]
E	Total energy per unit mass	[J/kg]
F	Body force per unit volume	[N/m^3]
F_{vap}	Empirical evaporation coefficient in ZGB model	[-]
F_{cond}	Empirical condensation coefficient in ZGB model	[-]
g	Gravitational acceleration vector	[m/s^2]
h	Specific enthalpy	[J/kg]
h_f	Saturated liquid enthalpy	[J/kg]
h_g	Saturated vapour enthalpy	[J/kg]
H_{1L}	Liquid enthalpy at inlet pressure	[J/kg]
H_{2L}	Liquid enthalpy at outlet pressure	[J/kg]
H_{2G}	Gas enthalpy at outlet pressure	[J/kg]
I	Turbulence intensity	[-]
JT	Joule-Thomson coefficient	[K/Pa]
k	Turbulent kinetic energy	[m^2/s^2]
k_t	Turbulent thermal conductivity	[W/(m·K)]
M	Mach number (u/a)	[-]

Symbol	Definition	Unit
M_{CO_2}	Molar mass of carbon dioxide	[kg/mol]
n	Bubble number density	[1/m^3]
P	Static pressure	[Pa]
P_1	Upstream pressure	[Pa]
P_2	Downstream pressure	[Pa]
P_c	Critical pressure	[Pa]
P_{sat}	Saturation pressure	[Pa]
P_{SHL}	Pressure at superheat limit	[Pa]
P_v	Vapour pressure (saturation pressure)	[Pa]
P_∞	Stiffening pressure in stiffened gas EoS	[Pa]
Q	Volumetric flow rate	[m^3/s]
q	Energy offset in stiffened gas EoS	[J/kg]
R	Universal gas constant	[J/(mol·K)]
R_B	Bubble radius in ZGB model	[m]
R_c	Condensation source term in ZGB model	[kg/(m^3·s)]
R_e	Evaporation source term in ZGB model	[kg/(m^3·s)]
r^*	Critical bubble radius	[m]
Re	Reynolds number	[-]
s	Specific entropy	[J/(kg·K)]
S	Strain rate magnitude	[1/s]
T	Static temperature	[K]
T_c	Critical temperature	[K]
T_r	Reduced temperature (T/T_c)	[-]
u	Velocity magnitude	[m/s]
u_l	Liquid phase velocity	[m/s]
u_v	Vapour phase velocity	[m/s]
u_{slip}	Slip velocity between vapour and liquid phases ($u_v - u_l$)	[m/s]
v	Molar volume	[m^3/mol]
x	Vapour quality (mass-based vapour fraction)	[kg/kg]
Z_c	Critical compressibility factor	[-]
α	Volume fraction of a phase	[-]
α_L	Liquid phase volume fraction	[-]
α_V	Vapour phase volume fraction	[-]
α_{nuc}	Nucleation site volume fraction in ZGB model	[-]
ΔP	Pressure drop	[Pa]
δ	Reduced density (ρ/ρ_c)	[-]
ϵ	Dissipation rate of turbulent kinetic energy	[m^2/s^3]
γ	Ratio of specific heats (c_p/c_v)	[-]
κ	Interface curvature	[1/m]
μ	Dynamic viscosity	[Pa·s]

Symbol	Definition	Unit
μ_t	Turbulent viscosity	[Pa·s]
μ_{JT}	Joule-Thomson coefficient	[K/Pa]
ϕ	Non-dimensional Helmholtz free energy	[-]
ρ	Density	[kg/m^3]
ρ_m	Mixture density	[kg/m^3]
σ	Surface tension	[N/m]
τ	Inverse reduced temperature (T_c/T)	[-]
θ	Relaxation time (HRM model)	[s]

1

Introduction

The European Union has outlined ambitious climate objectives, aiming for net-zero emissions by 2050 and a reduction of at least 55 % in greenhouse gas emissions by 2030. These goals will be achieved through initiatives like industrial carbon management and renewable energy integration. These efforts are vital in the pursuit of emissions reduction in energy-intensive industries and in moving toward a sustainable future [1]. The fossil fuel consumption for energy purposes is projected to reduce approximately by 80% relative to the levels of 2021 [2]. This could be driven through development and integration of renewable energy sources, circularity, industrial symbiosis, energy efficiency, alternative production processes and material substitution, with the reuse of carbon being a key component in achieving this transition. This shift is further leveraged by the reformed EU Emissions Trading System (ETS) imposing stringent measures to make the industrial emissions decline at an accelerated pace to reach the 2030 target. Despite these efforts, a small amount of fossil fuel usage is still expected in 2040, particularly in sectors such as transport, heating and industrial purposes. This emphasizes the ongoing need for industrial carbon management technologies as a part of the broader strategy towards achieving climate neutrality by 2050. Furthermore, additional measures are needed to reduce and manage carbon emissions from hard-to-abate industrial processes [3].

The EU is relatively well positioned in terms of research and innovation with a wide spectrum of CO_2 capture technologies developed by companies. Several policies have already been formulated by EU to aid the capture of CO_2. However, in order to reach the climate neutrality targets, the carbon capture and storage technologies must be significantly scaled up. In the Net Zero Industry Act, the Commission has proposed that at least 50 million tonnes of CO_2 per year can be stored geologically by 2030 [1]. Modelling the 2040 climate target communication suggests that around 280 million tonnes would have to be captured by 2040 with a further increase to 450 million tonnes by 2050 [4] as depicted in Figure 1.1 . To aid the activities, ETS carbon price also provides an incentive to capture CO_2 generated from fossil fuel and industrial process emissions. This incentive is expected to grow as a result of the last reform, as the ETS emissions cap is steadily decreasing further, setting a strong price expectation for carbon in the EU.

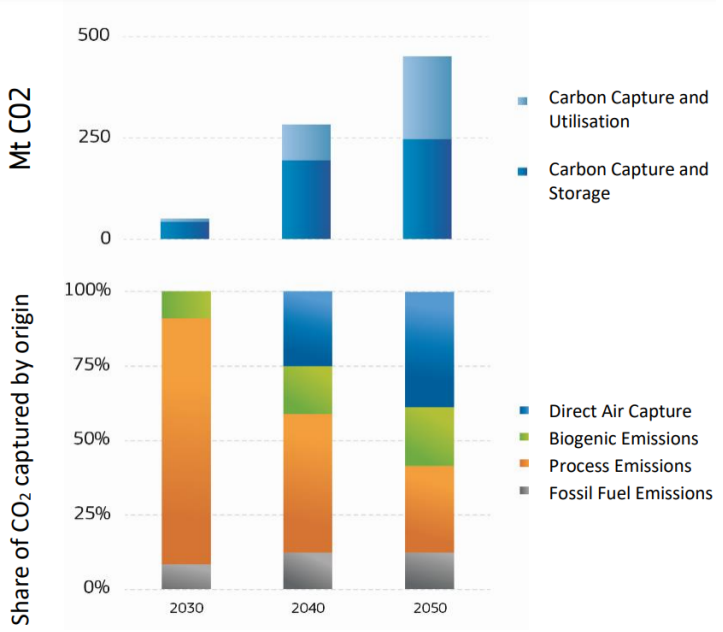

Figure 1.1: Projected volume of carbon dioxide captured for storage and utilisation in the European Union [4]

Enhanced policy frameworks in Europe have strengthened the business case for CCS projects, resulting in a 61% rise in projects in 2023 compared to 2022 Global CCS status report [5]. In the CCS initiatives within Europe, countries such as Denmark, The Netherlands, Norway and The United Kingdom have taken significant steps. The North Sea continues to serve as the primary hub for CO_2 storage in Europe due to the availability of many depleted oil & gas fields and saline aquifers, while potential storage sites are increasingly being identified in Bulgaria, Croatia, southwestern France, Greece, Italy and Romania [6].

The geological characteristics of the Dutch subsoil and the strategic location render The Netherlands highly suitable for underground CO_2 storage. The Netherlands has taken giant leap into the CCS segment with the key projects - Porthos and Aramis aiming to store CO_2 in the depleted oil and gas fields in the North Sea, offshore to the Rotterdam area. The Rotterdam port area contributes to nearly 14% of CO_2 emissions in the Netherlands [7]. This emphasizes the need for implementing effective CO_2 capture and storage solutions in this region, which is critical for achieving the national carbon reduction goals.

1.1. The Porthos Project

Porthos, stands for Port of Rotterdam CO_2 Transport Hub and Offshore Storage. The project is a collaboration between EBN, Gasunie and Port of Rotterdam Authority. The Porthos infrastructure aids to store CO_2 from the industries (Shell, ExxonMobil, Air Liquide and Air Products) situated in the Port of Rotterdam area. The infrastructure includes a 30 km-long pipeline that runs through the Rotterdam port, extending from the eastern end of Oude Maas in the Botlek area, through Europoort, and reaching the compressor station at Maasvlakte. The transport of CO_2 happens through sub-sea pipelines to the existing platforms in the North Sea, approximately 20 km off the coast. From this platform, CO_2 will be pumped into the depleted gas fields situated more than 3 km beneath the North Sea. The map

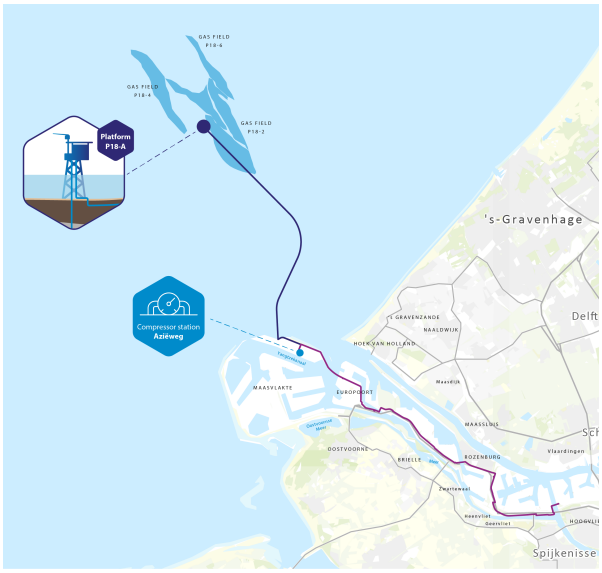

Figure 1.2: Map of Porthos

of Porthos project is depicted in the Figure 1.2. The project has an estimated storage capacity of 2.5 Mton per year (which is equivalent to 1.3 % of annual emissions of 2023 [8]) for a 15 year period, totalling 37 Mton. The gas fields are well situated in a well sealed reservoir of porous sandstone for long term storage stability. The onshore transport system of Porthos is constructed with a long term view point to allow for synergy (E.g: Usage of same compressor station infrastructure) with the future CCS projects like the Aramis project. With the construction works already underway, the system is expected to commence operations from 2026 [9].

1.2. Transportation of CO_2 and Associated Challenges

CO_2 can be transported in gaseous, liquid, dense, or supercritical states, with gaseous transport being less efficient due to its lower volumetric flow rate [10]. To overcome this limitation, CO_2 is generally transported in liquid form for road, rail or ship transport and in supercritical form for pipeline transport [11] as illustrated in Figure 1.3. The supercritical carbon dioxide exhibits the properties of both liquid and gas phase, with the density similar to that of the liquid phase but having high compressibility and low viscosity similar to that of gas phase. The high density facilitates transport of higher mass within the same volume. Pipeline transportation of CO_2 is generally conducted above critical pressure, either in the dense phase (below the critical temperature) or as a supercritical fluid (above the critical temperature), to prevent phase transitions. Dense and supercritical CO_2 enable significantly higher mass transport compared to natural gas pipelines or gaseous CO_2. As a result, smaller pipeline dimensions can be utilized to transport the same mass of CO_2, thereby reducing material costs.

Besides the advantages, the transport of CO_2 in the dense or supercritical phase has certain potential disadvantages. Though the surface transport pipeline is at high pressure - about 80 to 120 bar, the depletion pressure of gas reservoir after production can sometimes be below 20 bar. The CO_2 pressure has to be reduced from the pipeline pressure to the pressure close to the depletion pressure to ensure the integrity of the installations and well. The pressure needs to be just above the depletion pressure to provide the necessary driving force. The pressure reduction is carried out by means of control valves.

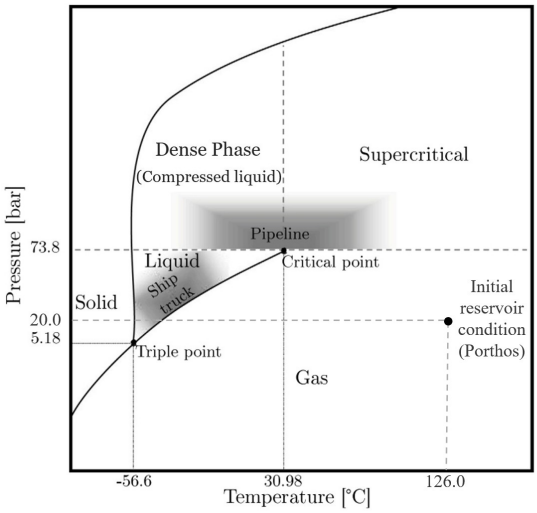

Figure 1.3: Phase diagram of CO_2 depicted with regions for different modes of CO_2 transportation [12]. The plot has been overlaid with the initial reservoir condition of P18 gas fields in Porthos project.

This large pressure reduction must be cautiously and effectively managed for the following reasons,

1. The large pressure drop can cause the pressure of CO_2 to fall below the vapour pressure, leading to flashing, which results in two phase flow in the pipeline. This causes the pipeline to get chocked - a flow phenomenon where the mass flow rate through the valve cannot be increased despite lowering the downstream pressure.
2. It can lead to high flow velocity within the valve body. The liquid particles get carried by the high velocity vapour phase, leading to erosion of valve trim and body materials, if incompatible materials are used. Higher percentage of vapour would lead to more damage.
3. It can translate to significant reduction in temperature of CO_2 due to high Joule-Thomson coefficient. This might lead to low temperature embrittlement and degradation of coatings, if incompatible materials are used [13].

Besides the issues arising due to large pressure drop, the system might encounter transient effects during startup, shut-in, variation in CO_2 production rates and uncontrolled depressurisation which leads to operational challenges [13]. The presence of impurities such as O_2, SO_x, NO_x, H_2 and N_2 can also influence the phase behaviour of CO_2, cause scaling and can cause corrosion in the pipelines. The non-condensable gases can increase the critical temperature and pressure of CO_2, thereby enhancing the possibilities of two-phase flow during transportation, demanding higher operational pressure to maintain the dense or supercritical phase, which increases the compression and transportation costs further. Therefore, it is vital to employ appropriate capture and separation methods to ensure high purity of CO_2 [14].

1.3. Problem Statement

The ambitious climate goals by EU to reduce the greenhouse gas emissions to achieve climate neutrality in 2050 have incentivized industries to explore effective and economically viable options to decarbonize their operations. However, the implementation and scaling of CCS systems has certain under-

lying challenges. As already discussed, CO_2 transportation is preferred in dense or supercritical phase at high pressure to maximize the transport efficiency in pipelines. The transition from high-pressure pipeline conditions (80–120 bar) to the low pressures near depleted gas reservoirs (as low as 20 bar) requires precise control to maintain system integrity. This large pressure drop has following operational challenges,

- **Pressure Management:** The pressure containing and pressure retaining parts of the control should be appropriately designed to handle the high pressure drop happening across the severe service control valve.
- **Flashing and Choked Flow:** Large pressure drops in control valves can cause CO_2 to flash, resulting in two-phase flow. This can result in choking, a scenario where the mass flow rate cannot be increased despite further reductions in the downstream pressure. The reduction of speed of sound in two-phase flows can lead to formation of shockwaves within the valve leading to excessive vibration and detrimental effects.
- **Material Erosion:** The high pressure drop can lead to high flow velocities within the valve body during flashing and can lead to erosion of valve trim and body as illustrated in Figure 1.4.
- **Temperature Effects:** The rapid depressurisation leads to considerable temperature drops, due to the Joule-Thomson effect. This can cause material embrittlement and coating degradation, necessitating the use of specialized materials.

Figure 1.4: Comparison of a normal (left) and flashing damaged top-guided valve plug (right) [15]

Upon literature review it was found that, the phase transition dynamics of supercritical CO_2, particularly, the flashing behavior during rapid pressure drops, are not comprehensively studied. Existing multiphase flow models vary in their ability to predict the behaviour of dense or supercritical CO_2 under non-equilibrium phase transition, with limited experimental validation, restricted to simple geometries such as pipes, nozzles etc. Building on the foundational research conducted by Bob Fluttert [16] on understanding the behavior of CO_2 flow within control valves, few limitations have been identified that establish the rationale for this study. Bob's work utilized Quasi-1D simulations in converging-diverging nozzles using the Enhanced Mass Transfer (EMT) model to examine phase transitions, offering signif-

icant insights into CO_2 flashing and choked flow phenomena. However, the simulation encountered difficulties in accurately modeling flow behavior near the critical point due to steep thermodynamic gradients. As a result, the study was restricted to the dense-phase region—above the critical pressure but below the critical temperature—rather than the supercritical regime. Furthermore, surface tension effects were neglected. Given that CO_2 is predominantly transported in the supercritical phase within the CCS infrastructure, these limitations underscore the need for more advanced modelling approaches and a deeper understanding of CO_2 flow dynamics in control valves.

The fundamental research question of the study will be:

What is the flow behaviour of supercritical CO_2 when passing through a converging-diverging nozzle and how can existing modelling approaches be extended to accurately simulate phase transition phenomena under supercritical conditions?

To address the research questions, the study will:

- Extend the existing EMT framework from dense phase to supercritical conditions, resolving the modelling challenges near critical point.
- Evaluate and identify suitable multiphase flow models and equations of state for accurate and stable prediction of CO_2 behavior near critical point.
- Develop and validate computational models that are scalable to higher dimensional geometries, with a focus on quasi-1D and 2D converging-diverging nozzles as intermediate steps.
- Investigate the physical phenomena associated with flashing and choked flow in CO_2 and the resulting effects.

By this approach, the study aims to provide valuable insights for the design and optimization of control valves, ensuring the safe and efficient transport of CO_2 within CCS infrastructures.

1.4. Rationale and Structure of Study

This study examines the expansion behaviour of supercritical CO_2 through a converging–diverging nozzle, with particular emphasis on phase-transition dynamics, shock formation, and subsequent multiphase flow behaviour.

The simulations in this study were performed using Ansys Fluent. The existing Enhanced Mass Transfer (EMT) framework from the prior work was extended to handle supercritical inlet conditions and flow regimes operating in proximity to the critical point.

Chapter 2 outlines the theoretical background relevant to the physical phenomena investigated in this study. The numerical methodology and simulation setup are detailed in Chapter 3. Chapter 4 presents the results of the simulations along with comparisons to experimental data. Chapter 5 summarises the key findings and conclusions and finally Chapter 6 provides recommendations and directions for future research.

2

Theoretical Background

The uncertainty linked to unforeseen behaviour in CO_2 transport in pipelines can be minimized or even eliminated if effective modelling is done before construction of any pipeline network. This aids in identifying and addressing potential challenges during the deployment and operational phases of the system. Thus, necessary measures can be taken to enhance the reliability and mitigate the operational risks associated. This enhances the reliability and eliminates the operational hazards of the system [17].

Both experimental and numerical methods can be utilized to forecast the behavior of carbon dioxide within control valves. These forecasts are essential for the design of industrial-scale carbon capture and storage (CCS) projects, as outlined in Chapter 1.2. A strong correlation between experimental results and numerical models indicates a solid comprehension of the phenomena involved. This chapter provides an overview of prior research on CO_2 flow and delves into the fundamental physics that underpin its behavior.

2.1. Physical Properties of Carbon Dioxide

Pipeline engineering for hydrocarbon transport has a well-established history, with extensive expertise in oil and gas transportation, including Enhanced Oil Recovery (EOR) processes [18]. However, the transport of CO_2 streams presents additional challenges. Numerous studies have emphasized the need to address a range of specific issues, linked to operating pressure, repressurisation levels and pipe integrity. In contrast to multicomponent hydrocarbon systems, CO_2 has a well-defined triple point (517 kPa at 216.55K) and critical point (7.38 MPa at 304.13 K), as they are usually transported in pure state. However, as elaborated in the section 1.2, the presence of contaminants in the stream can modify the phase behaviour of carbon dioxide. Being a single component system, the depressurisation of carbon dioxide happens along a phase line, as the temperature and pressure are tightly coupled. Whereas the depressurisation of hydrocarbon systems typically happen along a phase envelope.

The Joule-Thomson effect describes the temperature change experienced by a real gas or liquid during isenthalpic expansion [19]. It is quantitatively expressed using the Joule Thomson coefficient and is

defined using the relation,

$$\mu_{\mathrm{JT}} = \left(\frac{\partial T}{\partial P}\right)_H \tag{2.1}$$

The Joule Thomson coefficient may be positive, negative or zero depending on the temperature. At room temperature, the temperature of carbon dioxide decreases due to expansion, indicating a positive Joule Thomson coefficient. The temperature at which the Joule Thomson coefficient is zero is called the inversion temperature. The inversion temperature is a point of inflexion for Joule Thomson coefficient and its sign changes before and after this point. Figure 2.1 shows the Joule Thomson inversion curve for carbon dioxide.

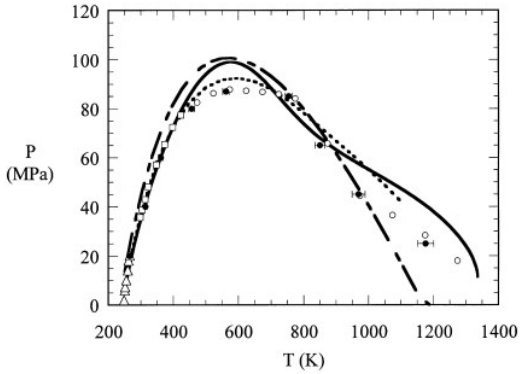

Figure 2.1: The JT inversion curve for CO_2 is depicted, with symbols representing experimental data: triangles correspond to data from [19], squares from [20], and circles from Price's results [21]. The dashed-dotted line represents the prediction using the Peng-Robinson EOS [22], the solid line corresponds to the Pitzer-Sterner EOS [23], and the dashed line indicates the prediction using the Span-Wagner EOS [24]. Additionally, the solid circles represent the results of Monte Carlo simulations.

For carbon dioxide, the Joule-Thomson coefficient averages approximately 1.023 ± 0.13 K/bar, indicating a pronounced cooling effect [21]. This is of high relevance especially during high depressurisation from the high pressure dense supercritical phase, that happens within a control valve.

The depressurisation of pipeline happens during planned events such as pressure reduction through a control valve or during accident such as pipe fracture. Under these circumstances, depressurisation is caused by the depressurisation waves which travels in opposite direction to the direction of flow [25]. The depressurisation wave travels through the pipeline with a wave speed which is equal to $c - u$, where u is the local outflow velocity and c is the local speed of sound [26]. In single-phase systems, speed of sound is primarily a function of the local temperature. There is, however, a high possibility of the system passing into a two-phase regime owing to flashing during depressurisation. In fact, an estimation of the speed of sound in a multiphase system is much more complex than in single-phase systems and depends on the fluid properties and thermodynamic characteristics of the individual phases. The various methods of speed of sound determination in the multiphase systems will be discussed in detail in Chapter 2.5.

Regardless of the methodology utilized, the speed of sound in a multiphase system is always lower than in a single-phase system. This means that the occurrence of two-phase flow will delay the decompression process. The estimation of the speed of sound accurately needs to be supported by appropriate equations of state, which will be discussed in Chapter 2.3.

2.2. Choked Flow & Flashing in Control Valves

With a fixed valve trim area (valve orifice area) and a constant upstream pressure $(P1)$, the flow rate through the valve will typically increase as the downstream pressure $(P2)$ is decreased. This trend is represented by the linear line labeled as ”Ideal” in Figure 2.2. However, in practical scenarios, the flowrate does not increase indefinitely, beyond the choked flow limit. Beyond this limit, further reduction in the downstream pressure have no significant effect on the flow rate.

In liquid systems, choking occurs due to a significant pressure reduction as the fluid moves through the trim (control components) of the control valve. Figure 2.3 illustrates the variation in instantaneous pressure as liquid flows through a control valve. The cross-sectional areas at the valve's inlet and outlet are substantially larger than those at the trim elements such as seat ring, plug and cage. Since the volumetric flow rate must remain constant throughout the valve, the fluid velocity increases significantly at the restricted area (vena contracta) to maintain the same flow rate.

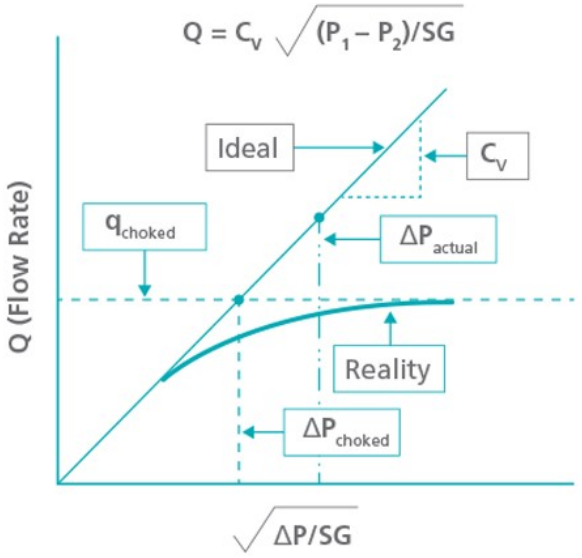

Figure 2.2: Variation of flowrate with respect to pressure drop in control valve [27]

According to Bernoulli's principle, the total energy of the fluid remains constant along the flow path. Consequently, an increase in velocity would result in corresponding decrease of local pressure. Once the fluid exits into the larger outlet piping, the velocity decreases, leading to partial pressure recovery. This sharp pressure drop becomes more pronounced with increasing flow rates.

When the instantaneous pressure at the vena contracta falls below the liquid's vapour pressure as illustrated in Figure 2.3, vapour bubbles begin to form, indicating the onset of boiling. The phase transition from liquid to vapour causes an increase in fluid volume, which causes a restriction to the flow. Further reductions in downstream pressure (P2), would lead to an expansion of the vapour phase, thus reaching a point where no additional increase in flow rate is possible, regardless of further pressure reductions. This phenomenon is referred to as choked flow.

In gas applications, choking occurs when the gas velocity at the valve reaches the speed of sound (sonic velocity). Beyond this point, the formation of a standing shock wave restricts further increases in flow velocity. Consequently, any additional reduction in downstream pressure has no effect on the

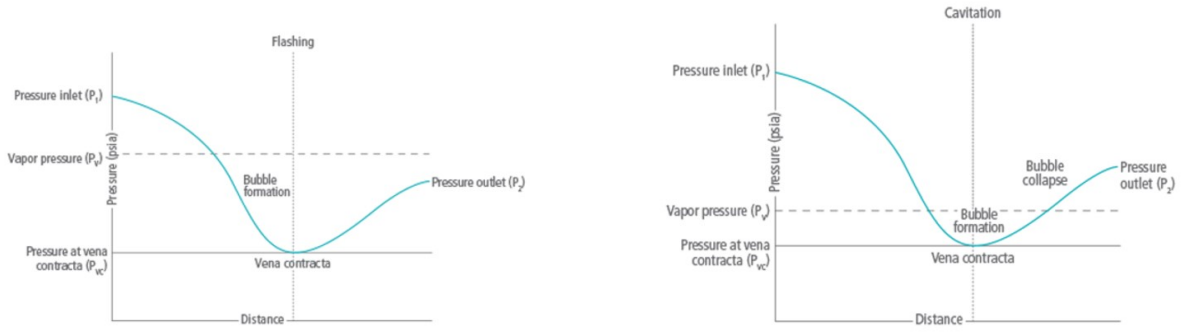

(a) Flashing pressure profile

(b) Cavitation pressure profile

Figure 2.3: Pressure curves of flashing and cavitation liquid within a control valve [27]

flow rate.

The phenomenon of formation of vapour bubbles due to the local pressure venturing below the vapour pressure at the vena contracta is referred to as flashing. Flashing leads to two-phase flow (liquid and vapour) inside the flow. Erosion occurs in flashing because the liquid particles are carried by the high velocity vapour. The higher the percentage of flashing, higher is the percentage of vapour in mixture and more damage occurs. For liquids with single vapour pressure and well defined thermodynamics properties such as water the percentage of flashing (percentage of vapour by weight) can be calculated using the liquid enthalpy at the inlet pressure and liquid and vapour enthalpies.

$$\% \text{ of Flashing } = \left[\frac{H_{1L} - H_{2L}}{H_{2G} - H_{2L}}\right] \times 100 \; = \; x \; \times 100. \tag{2.2}$$

where

H_{1L} is the liquid enthalpy at inlet pressure,

H_{2L} is the liquid enthalpy at outlet pressure,

H_{2G} is the gas enthalpy at outlet pressure and

x is the vapour fraction at the outlet.

Flashing conditions can cause valve damage, but in most cases, it is less critical compared with cavitation. The effect of flashing is more evident under conditions of very low openings of the valve when choking might not occur. With increasing opening, the possibility of flow choking increases, but valve damage decreases because the plug moves away from the seat.

The cavitation phenomenon resembles flashing, except that the recovered pressure downstream of the vena contracta is greater than the vapour pressure of the liquid. The vapour bubbles that are generated by cavitation collapse due to the high pressure, creating vibrations and noise in the control valve. This collapse creates microjets and localized shock waves that can erode the internal components of the valve and the downstream piping, leading to serious damage. It is important to note here that, as identified earlier, cavitation may occur even without fully choked flow in a valve.

The transport of CO_2 in pipelines predominantly happens in the dense liquid phase. Analyzing the

bubble dynamics close to the critical point of liquid CO_2, revealed that the thermal effects notably impact the bubble dynamics. This effect hinders the early motion of the bubble interface, resulting in gradual collapse of CO_2 bubble. This results in less pronounced detrimental effects compared to those typically observed in the flashing process of water [28].

2.3. Equation of State

As elaborated in Chapter 2.1, the decompression wave speed is primarily determined by the speed of sound in the fluid [26]. Hence, accurate estimation of speed of sound is important, which is determined by the choice of Equation of State (EOS). The Equation of State represent the correlation between the state variables such as density, pressure and temperature that enables estimation of the fluid properties under the given operating conditions.

The equation of state for ideal gas, expressed as $P/\rho = RT$ is the simplest form and assumes that there are no interactions between individual gas particles and is suitable for low-molar-mass gases under conditions far from phase transitions. However, its accuracy diminishes near the saturation line, necessitating the use of alternative models designed for real gases. These real gas models take into consideration the different intermolecular interactions occurring within the fluid and have been historically developed as semi-empirical correction terms to address deviations from ideal gas behavior.

Near the critical point, the task of calculating thermodynamic properties becomes substantially more challenging due to sharp thermodynamic gradients. Under such conditions, any approximation that links fluid behavior to that of an ideal gas becomes invalid. Even generalized real gas models may fail to appropriately describe properties in these scenarios, as their inherent simplicity cannot capture the complexities of such environments. Consequently, more sophisticated equations of state are required.

2.3.1. Peng-Robinson Equation of State

The Peng-Robinson EOS is a classical cubic formulation that provides reasonable accuracy for most fluids, especially at high pressure and in the vapour phase. However, within the two-phase region, the model has been shown to predict negative speeds of sound, resulting in unphysical wave propagation phenomena. Hence, usage of Peng-Robinson EOS is typically restricted only to the CO_2 vapour simulation.

$$p = \frac{RT}{v-b} - \frac{a}{v(v+b)+b(v-b)} \tag{2.3}$$

where

p is the pressure of the fluid.

ρ is the density of the fluid.

R is the universal gas constant.

v is the molar volume of the fluid.

$a = 0.45724\frac{R^2T_c^2}{\rho_c}$ represents the intermolecular attraction forces (Van der Waal's force) that exists between molecules.

$b = 0.77796\frac{RT_c}{\rho_c}$ represents the finite volume occupied by the molecules [29].

Being a cubic EOS, the estimation of state properties involves iterative calculations which are computationally intensive. While Peng-Robinson EOS is efficient for vapour phase simulations, its application is not adequate for two-phase simulation. Hence, its utility is limited in accurate modelling of CO_2 in carbon sequestration process.

2.3.2. Stiffened-Gas Equation of State

The Stiffened-Gas EOS is the linearized version of the Mie-Grüneisen EOS, which is widely utilized for steam-water simulations. The stiffened gas EOS is given by,

$$p = (\gamma - 1)(e - q)\rho - \gamma P_\infty \tag{2.4}$$

where

p is the pressure of the fluid.

ρ is the density of the fluid.

γ is the specific heat capacity of the fluid.

e is the specific internal energy.

q is the additional energy offset.

P_∞ is the stiffening pressure.

The absence of iterative process in the estimation of parameters, it offers significantly faster computational performance compared to cubic EOS models [30]. However, the accuracy of the EOS is dependent on appropriate selection of values for γ, q and P_∞. Also, being a linear model, stiffened gas EOS does not provide good accuracy in the vicinity of critical point.

2.3.3. Span-Wagner Equation of State

The Span-Wagner equation of state is considered state-of-the-art for CO_2, offering precise thermodynamic predictions across extensive temperature and pressure ranges - from the triple point temperature up to 1100 K and pressures as high as 800 MPa [31]. The SW EOS is based on the non-dimensional representation of Helmholtz free energy, which can be expressed in the following form [24],

$$\phi(\delta, \tau) = \phi^o(\delta, \tau) + \phi^r(\delta, \tau), \tag{2.5}$$

where

$\phi = \frac{A}{RT}$ is the non-dimensional Helmholtz free energy.

$\delta = \frac{\rho}{\rho_c}$ is the reduced density.

$\tau = \frac{T_c}{T}$ is the inverse reduced temperature.

The final form of SW EOS has been derived through fitting hundreds of parameters with vast dataset

of experimental data and can provide much accurate values than other EOS, particularly near the critical point. Despite the accuracy of EOS, it is highly costly from a computational point of view [32]. Moreover, the SW EOS is not directly integrated into many commercial computational fluid dynamics (CFD) software packages, such as *Ansys Fluent* and *Ansys CFX*.

However, the SW EOS equation is available in the thermodynamic and transport property databases like *REFPROP* and *CoolProp* which provides an alternate way to execute the Span Wagner EOS in *Ansys Fluent*. This can be achieved either by making a direct call to *REFPROP* libraries from *Ansys Fluent* [33]. However this approach was also found to be computationally expensive and would slow down the solution process. This drawback can be overcome by using an alterative approach called the Tabulated EOS approach [16].

2.4. Equilibrium and Non-Equilibrium Phase Transition of Carbon Dioxide

The fundamental topic of interest for this study is the phase change process associated with the super-critical phase carbon dioxide when it experiences a pressure drop. Such expansion process of CO_2 are typically encountered in control valves, converging-diverging nozzles, ejectors in refrigeration system and other flow configurations. Under ideal case, the flow through nozzle is assumed to be adiabatic with negligible frictional losses, ensuring that specific stagnation enthalpy remains conserved. This specific stagnation enthalpy is approximately equal to the specific enthalpy when the flow velocity is relatively small. Under these adiabatic and reversible conditions, the flow is consequently isentropic, meaning that the entropy remains constant throughout the process. During the expansion process, there is a drop in the pressure and temperature of the fluid and the thermodynamic state of the fluid may cross the saturation line, after which the fluid can no longer remain in its initial physical state and transitions into a mixture or a new phase. As illustrated in the Figure 2.4, CO_2 in supercritical state (A) is condensed into liquid state (E). When the expansion process is relatively slow, equilibrium phase transition is expected to occur in the system (i.e) the phase transition happens along the saturation line (along the path A-B-C-E), where the fluid transitions directly without entering metastable states.

However in case of rapidly expanding flows, the high velocity of the fluid prevents phase transition at the saturation line. Instead it ventures into the metastable (sub-cooled vapour) state, delaying phase transition. Instead, the condensation happens here along the path (A-B-D-E). Between points B and D, the fluid is expanding in a regime where, under equilibrium conditions, formation of liquid droplets is expected. However, here the condensation process is delayed either because of lack of nucleation sites or the inability of phase transition to keep up with the rapid expansion process. The system remains in a non-equilibrium metastable state until point D. When there are sufficient nucleation sites or when the system has slowed down, the condensation process happens and the system can no longer remain in metastable state and returns to the saturation line at point E. Thus the non-equilibrium condensation follows the trajectory A-B-D-E.

2.4.1. Limits of Metastability

The limit of metastability (point D in the above case) can be characterized by two different lines in the phase diagram. The theoretical thermodynamic limit of stability beyond which metastable states do not

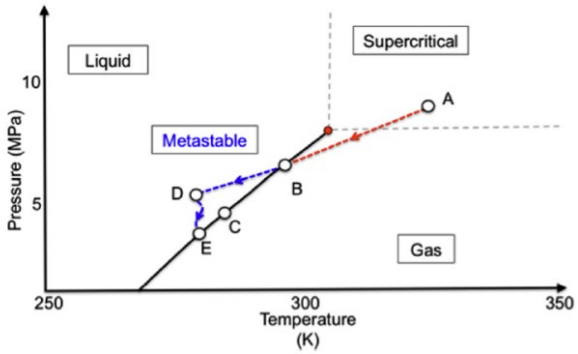

Figure 2.4: Trajectories of equilibrium and non-equilibrium condensation of supercritical carbon dioxide in a P-T diagram [34]

continue to exist and the fluid spontaneously undergoes phase transition, is called as the spinodal limit. The spinodal limit can be mathematically defined as the locus of the all the points where $\left(\frac{\partial_p}{\partial_v}\right)_T = 0$ [35]. It should be noted that the spinodal line is only a theoretical limit and the practical limit of metastability is provided by the Wilson line.

Unlike the spinodal line, the Wilson line has to be experimentally determined for an expansion process, because Wilson line is a flow property and not a fluid property [36]. High velocity flow, for example, can venture deep into the metastable state without onset of phase transition than a low velocity flows under identical conditions. Wilson line is the limit where the nucleation rate is high enough to initiate the phase transition and is characterized by the formation of a visible fog. The spinodal line is located deeper within the two-phase dome than the Wilson line, as confirmed by non-equilibrium condensation experiments conducted on supercritical CO_2 in de Laval nozzles, such as those by Lettieri et al. (Figure 2.5)

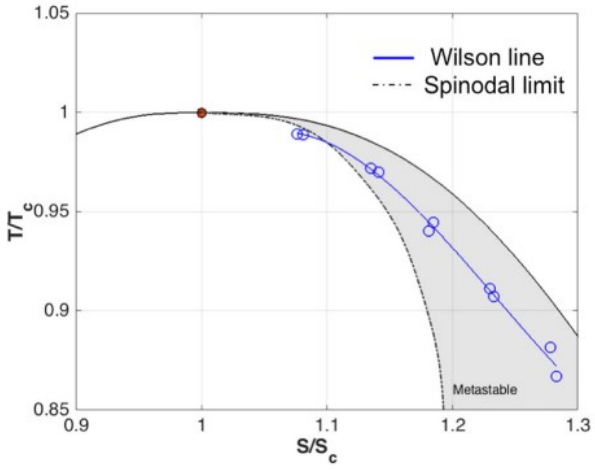

Figure 2.5: T-S diagram depicting the spinodal limit determined using the NIST Span-Wagner EOS and the experimentally determined Wilson line [37]

During isentropic expansion, the flow through the nozzle can either undergo cavitation or condensation depending on the thermodynamic state of the fluid at the inlet. When the inlet entropy of the fluid exceeds the supercritical entropy (cases 1 to 5 in Figure 2.6, the fluid is initially in vapour phase. As the fluid expands, it first enters into the metastable region and remains as a superheated vapour (blue

regions in Figure 2.6). It could be seen that the metastable regions become narrower close to the critical point, illustrating that the metastable effects are less significant close to the critical point of the fluid. Once the metastable limit is reached, the fluid can no longer remain as supersaturated vapour and liquid droplets begin to form. This expansion process leading to formation of liquid droplets is referred condensation (Cases 1 to 5 in Figure 2.6). Conversely, if the inlet entropy is less than the supercritical entropy, the fluid enters in liquid phase. As it enters the metastable liquid phase, it becomes superheated liquid and subsequently, after the metastable limit, vapour bubbles are formed in the liquid which could lead to cavitation in the fluid (Cases A and B in Figure 2.6).

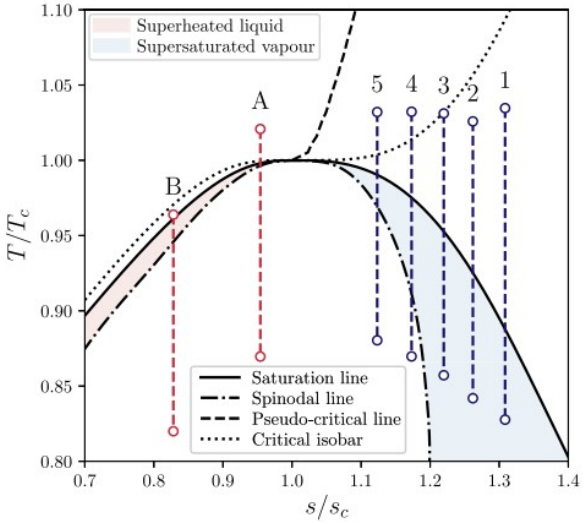

Figure 2.6: Isentropic expansions leading to cavitating and condensing flows depicted in a T-S diagram [38]. Cases A and B from experiments of Nakagawa et al. [39] represent cavitating flow. Cases 1 to 5 from experiments of Lettieri et al. [37] represent condensing flows.

2.5. Speed of Sound

As elaborated in Section 2.1, accurate estimation of speed of sound is critical for modelling phenomena such as depressurisation, shock waves in supersonic flow, and associated processes. In case of single phase flows, the speed of sound is related to how pressure changes with respect to density under isentropic conditions and is given by the following relation [40],

$$c_m^2 = \left(\frac{\partial P}{\partial \rho_m} \right)_S \tag{2.6}$$

The properties, ρ and P here are obtained from the Equation of State being used. When lookup tables generated from *REFPROP* are employed, *Fluent* can access the speed of sound directly from these tables for the specified pressure and temperature which is generally faster instead of calculating dynamically. However, challenge arises with speed of sound calculation for two-phase flows. The *REFPROP* does not provide a speed of sound for a two-phase mixture (i.e., in the dome where liquid and vapor coexist simultaneously). In such cases, the speed of sound becomes a complex thermodynamic property, dependent on the mass fraction of each phase and the local dynamics of the liquid–vapor interface.

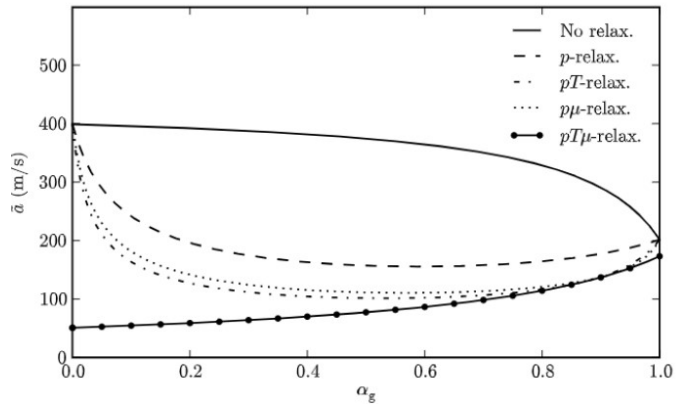

Figure 2.7: Speed of sound with respect to void fraction for CO_2 at 50 bar at full non-equilibrium, partial equilibrium and full equilibrium models [42]. Among the equilibrium models, HEM model ($pT\mu$-relax) and HFM model (p-relax) represent the extremities in the speed of sound values

In case of two-phase flows, *Fluent* computes an effective speed of sound based on its multiphase flow model, for example, the Homogeneous Equilibrium Model (HEM), which combines phase-specific properties into a mixture property using volume or mass fractions. The single phase speed of sound is always higher than the two-phase speed of sound.

The extreme cases of speed of sound is provided by Homogeneous Equilibrium Model (HEM) which assumes instantaneous heat transfer between the phases and the Homogeneous Frozen Model (HFM) which on contrary assumes no instantaneous heat transfer between the phases. The HEM model assumes for mechanical, thermal and chemical equilibrium between phases whereas the HFM model assumes for only mechanical equilibrium between the phases. With an increase in the degree of constraints of the system, the respective speed of sound also decreases [41], [42]. Thus, for example, the speed of sound predicted by the Homogeneous Equilibrium Model (HEM) is smaller than that obtained by the Homogeneous Flow Model (HFM), which relaxes the thermal equilibrium assumption. This is evident from the Figure 2.7.

For Mixture Models, *Ansys Fluent* employs the speed of sound formulation formulated by Wood [43] for post processing the mixture speed of sound, which is given as,

$$\frac{1}{\rho_m c_m^2} = \frac{\alpha_L}{\rho_L c_L^2} + \frac{\alpha_V}{\rho_V c_V^2} \tag{2.7}$$

As per this expression, $\rho_m c_m^2$ represents the harmonic average of bulk moduli of the components weighted by the volume fractions. This definition is derived based on single-phase volumetric behavior and, therefore, does not account for thermal interactions between the components. As a result, it is applicable under the assumptions of HFM and is widely utilized in cases involving multi-component flows that do not undergo chemical reactions. The HEM model was shown to exhibit discontinuity in zero speed of sound in saturation conditions especially for cavitating flows [38].Brennen [44] had also proposed a method to calculate the mixture speed of sound, which is given by,

$$\frac{1}{\rho_m c_m^2} = \frac{\alpha_V}{P}\left[(1-\epsilon_V) f_V + \epsilon_V g_V\right] + \frac{\alpha_L}{P}\left[(1-\epsilon_L) f_L + \epsilon_L g_L\right] \tag{2.8}$$

Here, the terms ϵ_L and ϵ_V are used to account for the fraction of liquid and vapour phases which can instantaneously transfer heat and momentum indicating equilibrium condition. Whereas the proportion of the phases that are not in equilibrium is given by $1-\epsilon_L$ and $1-\epsilon_V$. The following approximations for carbon dioxide have been proposed by Brennen specific to carbon dioxide: The parameters are given as $f_V = g_V \approx 1$, $f_L \approx 0$, $\epsilon_L \approx \alpha_V$, and $g_L \approx 2.1\left(\frac{P}{P_c}\right)^{-0.566}$. Using these approximations in Eq. 2.8 results in the below simplified, mixture speed of sound equation,

$$\frac{1}{\rho_m c_m^2} = 2.1\frac{\alpha_L \alpha_V}{P^{1.566} P_c^{0.566}} + \frac{\alpha_V}{P} \tag{2.9}$$

Brennen's formulation predicts the speed of sound values within the range bound by HEM and HFM models. For cavitating flows, Brennen's formulation, performs well except near the saturation conditions where the speed of sound exhibits discontinuities. This could be overcome by limiting the speed of sound to its single phase value. However, for condensing flows, the speed predicted by Brennen formulation was lower than that of HEM, which is physically inconsistent. It is important to note that the Wood and Brennen equations provide only an accurate "post-process" definition of the speed of sound, which does not influence the final numerical solution. The numerical speed of sound is determined mathematically by the governing system of equations and is directly impacted by the selected Equation of State.

2.6. Experimental References

In the context of CCS infrastructures, the reduction of pressure from pipeline conditions to levels near the depleted reservoir will occur within a control valve. But currently there are no experimental evidences on the flow of supercritical carbon dioxide in control valves. However, numerous experimental studies have investigated the flow of supercritical carbon dioxide through converging-diverging nozzles. These nozzles exhibit fundamental flow characteristics that are analogous to those occurring within a control valve. Specifically, the flow in a control valve is characterized by a pressure reduction (accompanied by flow acceleration) until the vena contracta, followed by a pressure recovery downstream of the vena contracta.

Given this similarity, performing simulation with a converging-diverging nozzle would provide a simplified yet insightful scenario for understanding the flow physics associated with flashing of CO_2. This serves as an initial step in understanding the key mechanisms and can then be scaled to the complex geometries and flow conditions within an actual control valve, which is the actual domain of interest. Hence the experimental and simulation references in this study will primarily focus on converging-diverging nozzles as the foundation for investigating the flashing behaviour of CO_2.

Nakagawa et al. [39] conducted an experimental investigation of supersonic two-phase flow of CO_2 in the diverging section of rectangular converging-diverging nozzles, which is relevant to ejector refrigeration systems. Rectangular stainless steel nozzles were utilized in the experiments due to the ease of fabrication and setup. The typical geometry used in the experiments is shown in Figure 2.8. Nozzles with four different divergence angles, namely 0.076°, 0.153°, 0.306°, and 0.612°, were tested in the experiments.

The experiments employed a CO_2 blow-down apparatus to generate supersonic flow conditions in the

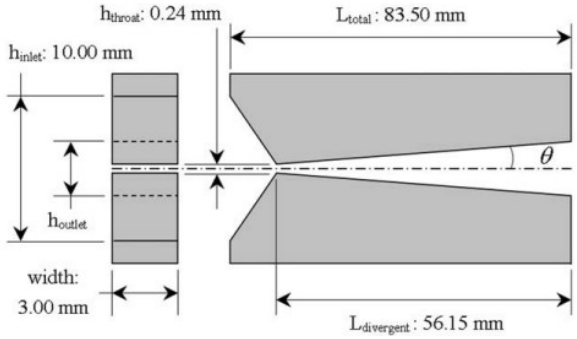

Figure 2.8: Schematic diagram of the experimental setup [45]

nozzle with the inlet static pressure ranging from 6-9 MPa and static temperatures between 20 and 37 °C respectively. The outlet from the nozzle was vented to the atmosphere and the back pressure was not controlled during the experiment. Static pressure and temperature measurements were measured using eleven thermocouples and strain gauges installed along the length of the nozzle. Additionally, saturation pressure was also calculated based on the measured temperature. It was observed that the calculated saturation pressure almost matched the pressure measured from strain gauge as long as the flow remains in two-phase regime, indicating the existence of phase equilibrium. A representative pressure curve recorded from the experiment is shown in Figure 2.9.A simulation was also carried out by using Isentropic Homogeneous Equilibrium (IHE) approach to model the flow. The simulation results showed good agreement with experimental results for divergence angle greater than 0.306°and high inlet temperatures (above 35°C). However, for smaller divergence angles and lower inlet temperatures, large deviations were observed, which could be due to frictional losses and non-equilibrium effects, that cannot be properly captured by the IHE model.

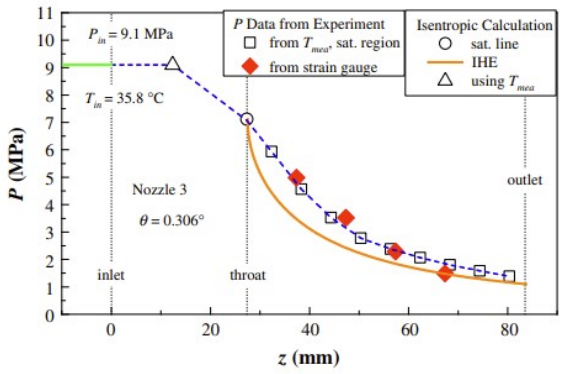

Figure 2.9: Pressure and temperature profiles along the length of the nozzle with a divergence angle of 0.612°, operating at an inlet pressure of 9 MPa and inlet temperature of 37°C. The nozzle outlet was vented to the atmosphere [39].

Nakagawa et al. also investigated shock waves in supersonic two-phase CO_2 flows through converging-diverging nozzles [45]. The study utilized a rectangular converging-diverging nozzle with varying lengths of the diverging section, while maintaining a fixed divergence angle of 0.48 °, as shock waves were observed exclusively at this angle. The experimental setup was integrated into a Vapour Compression Cycle (VCC) where the expansion valve was replaced by a converging-diverging nozzle. The inlet pressure between 9 to 10 MPa and temperatures between 37 to 50 °C were used for the study. A wide range of back pressures (3.6 to 5.9 MPa) was employed to investigate different intensities of shock

waves. In this study also, IHE model was used to calculate the pressure profiles upstream and downstream of the shockwave. While IHE predicted strong and thin equilibrium shock waves, these were not observed experimentally. Instead, relaxation effects dominated the experimental results, showing gradual pressure increases rather than sharp transitions. The experiments identified two types of weak shock waves:

1. **Pseudo-Shock Waves:** Observed in flows with the inlet entropy below the critical value. These waves exhibited a gradual and slight pressure increase as in Figure 2.10a. They were associated with phase change from saturated liquid to two-phase flow and were hypothesized to result from long velocity relaxation times between the liquid and vapor phases.
2. **Dispersed Shock Waves:** Observed when the inlet entropy exceeded the critical value. These waves displayed moderate and gradual pressure increases as in Figure 2.10b. They corresponded to phase change from saturated vapor to two-phase flow and were linked to short velocity relaxation times.

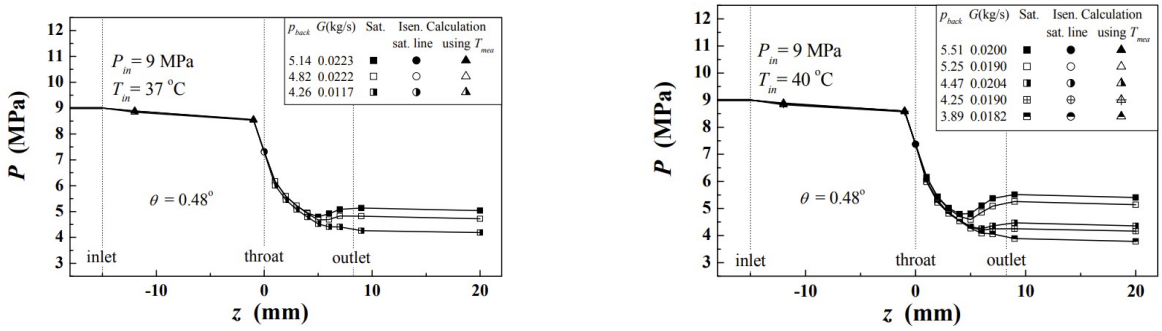

(a) pseudo-shock wave

(b) Dispersed shock wave

Figure 2.10: Comparison of pseudo and dispersed shock waves. pseudo-shock waves were observed for inlet pressure at 9 MPa and temperature at 37 °C and the phase change started from saturated liquid. Dispersed shock waves were observed for inlet pressure at 9 MPa and temperature at 40 °C and the phase change started from saturated vapour [45].

Claudio Lettieri et al. conducted an experimental and numerical investigation to characterize the non-equilibrium condensation of supercritical CO_2 during rapid expansion in a converging-diverging nozzle [37]. The experimental setup utilized a blow-down test rig with a rectangular converging-diverging nozzle equipped with high-pressure-rated optical windows, enabling optical access. The rectangular section aided in approximating the flow to be two-dimensional, which was confirmed using a 3-D CFD. Shearing interferometry was employed for high-resolution density gradient measurements, while static pressure measurements along the nozzle walls using pressure sensors. High-speed optical visualization captured the onset of non-equilibrium condensation as a white fog as illustrated in Figure 2.11. This serves as a marker for the Wilson line, which is the boundary between metastable and equilibrium conditions.

The study determined the Wilson line for temperature ranging from 263 to 295 K and pressures ranging from 26 to 65 bar, close to the critical point. These findings showed that the Span-Wagner EOS model could predict metastable properties with an accuracy of 0.2% at conditions away from the critical point but exhibited discrepancies of up to 2% near the critical region. Experimental observations also indicated that higher expansion rates shifted the Wilson line deeper into the metastable region, delaying condensation onset. Experimental pressure profile from the experiment indicated a bump in the static

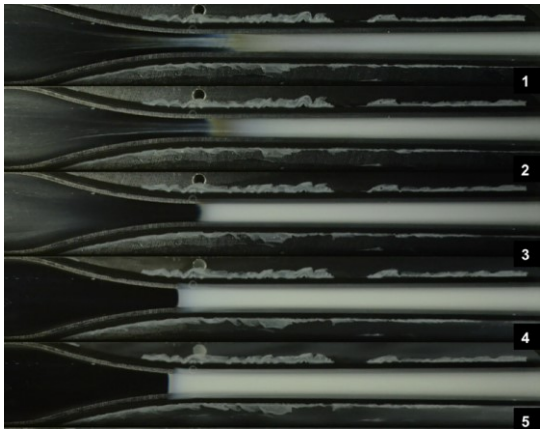

Figure 2.11: High speed footage of the nozzle test section from the five different test runs of Lettieri et al. With increasing the total pressure at a constant temperature and geometric expansion rate, the nucleation onset moved closer to the throat due to smaller metastable zone in the proximity to critical point [37].

pressure as illustrated in Figure 2.12 at the region where condensation onset happened. This was consistent with the condensation onset location observed from the visualization experiments.

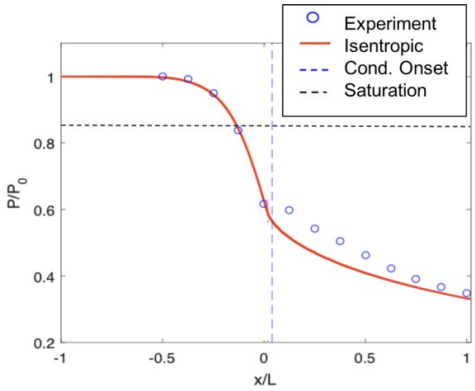

Figure 2.12: Experimental and isentropic simulation pressure profiles for a test case with an inlet total pressure of 80 bar and a total temperature of 310 K. The onset of condensation occurs at a pressure lower than the saturation pressure, illustrating the phenomenon of non-equilibrium condensation [34].

The SINTEF (Norwegian: Stiftelsen for industriell og teknisk forskning) has established a depressurisation facility as a part of European Carbon Dioxide Capture and Storage Laboratory Infrastructure (ECCSEL). The test setup is designed to study the rapid depressurisation of CO_2 in pipelines. This laboratory stainless features 61.67 m long stainless steel pipeline, instrumented with high-frequency pressure and temperature sensors, to capture transient phenomena during depressurisation. It can accommodate pressures up to 20 MPa and temperatures ranging from $5°$C to $40°$C, allowing controlled experiments under a variety of conditions [25]. The experimental data from this facility had been instrumental in the development of Homogeneous Flashing Model (HFM) and Delayed Homogeneous Equilibrium Model (D-HEM) which are elaborated in the section.

The TNO (Dutch: Nederlandse Organisatie voor Toegepast Natuurwetenschappelijk Onderzoek) Rijswijk Centre for Sustainable Geo-energy (RCSG) has recently established the Colorado flow loop, which is an outdoor test loop specifically developed for research of processes that can occur in the transport and injection of pure CO_2 or along with contaminants such as methane, carbon monoxide,

nitrogen, hydrogen, argon, etc. [46]. The system is capable of generating CO_2 flows at pressures up to 100 bar and process temperatures ranging from $-40°$C to $70°$C. The flow loop is primarily being equipped to simulate the CO_2 flow in choke valves, porous media and scenarios involving vapor collapse. With no experimental data available in the literature on CO_2 flow in control valves, this flow test loop presents a valuable opportunity to conduct flow experiments that could enhance the understanding of flow dynamics and support the development of accurate computational models.

2.7. Theory of Converging–Diverging Nozzles

The theoretical understanding of the compressible flow through passages with varying cross-sectional area serves as the fundamental basis for interpreting the phenomena such as choking, shock wave formation and phase change dynamics in converging-diverging nozzles.

While the actual flow fields in such systems are inherently two or three dimensional, the streamwise velocity component dominates over transverse velocity components, thus the governing equations can be approximated to a simplified quasi-1D form. With this approximation, the varying cross section area of the flow passage becomes the principal geometric factor and the flow behaviour can be interpreted using the established relations from the compressible flow theory. The flow in the C-D nozzle is generally treated as isentropic in the absence of discontinuities such as shock waves. However, the entropy increases across the shock waves, when present in the system.

The fundamental relation between the area and velocity in a flow through varying cross sectional area is given by the following relation,

$$\frac{dA}{A} = (M^2 - 1)\frac{dv}{v}, \tag{2.10}$$

where M is the Mach number and v is the axial velocity. This relation captures how velocity responds to changes in area, depending on the flow regime:

- **Subsonic flow** ($M < 1$): Velocity increases in a converging passage ($dA < 0$, $dv > 0$) and decreases in a diverging passage ($dA > 0$, $dv < 0$).
- **Supersonic flow** ($M > 1$): Velocity decreases in a converging passage ($dA < 0$, $dv < 0$) and increases in a diverging passage ($dA > 0$, $dv > 0$).

An important insight from this relation is that the sonic condition ($M = 1$) must occur at the minima of the cross-sectional area which is referred to as the geometric throat. When the flow accelerates to Mach 1 at the throat, the nozzle is said to be choked. It is important to note that while sonic conditions occur at the throat for ideal gas, not every throat necessarily results in choking unless specific upstream and downstream conditions are met. In a converging–diverging nozzle with real gas effects, phase change, shock waves and boundary layer growth, the sonic condition (M = 1) is related to the minimum effective area and the two-phase speed of sound, not necessarily the geometric throat. The sonic plane in this case shifts downstream depending on the thermodynamic state of the mixture and the effective flow area, rather than purely by the nozzle geometry.

For calorically perfect gases (which obeys ideal gas law and the specific heat does not vary with temperature), the area–Mach number relation for choked flow is defined as.

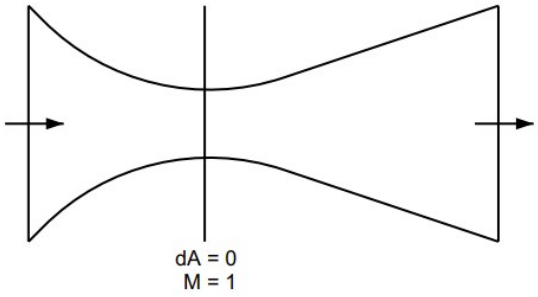

Figure 2.13: Representation of choking happening at the geometric throat of a converging-diverging nozzle [47].

$$\frac{A}{A^*} = \frac{1}{M}\left[\frac{2}{\gamma+1}\left(1+\frac{\gamma-1}{2}M^2\right)\right]^{\frac{\gamma+1}{2(\gamma-1)}}, \tag{2.11}$$

where A^* is the area corresponding to sonic conditions and γ is the ratio of specific heats. This equation can be used to determine the Mach number at any location of the nozzle. This equation yields two solutions for a given $\frac{A}{A^*}$ with one solution being subsonic and other being supersonic and the appropriate solution has to be chosen based on the other known details of the flow field [47].

The mass flow rate through a choked nozzle, assuming a calorically perfect gas is determined exclusively by upstream stagnation pressure (P_0), stagnation temperature (T_0) and the throat area (A_{throat}). It is expressed as:

$$\dot{m} = \frac{P_0 A_{\text{throat}}}{\sqrt{T_0}}\sqrt{\frac{\gamma}{R}\left(\frac{2}{\gamma+1}\right)^{\frac{\gamma+1}{\gamma-1}}} \tag{2.12}$$

The above expression does not involve any downstream flow parameters. This indicates that once the flow is choked, the mass flow rate becomes insensitive to the downstream conditions. A further reduction in back pressure will not alter the mass flow rate unless the upstream stagnation conditions or the throat area is adjusted [47]. This qualitative principle remains valid for non-calorically perfect substances also (e.g. supercritical CO_2, refrigerants).

Depending on the downstream pressure with a fixed inlet stagnation conditions different flow regimes can be observed as illustrated in Figure 2.14.

- **Case a (Subsonic flow throughout):** When then ambient(back) pressure (P_{ambient}) is relatively high, the flow accelerates sub sonically in the converging section but decelerates in the diverging section. The flow remains entirely subsonic and the exit pressure (P_{exit}) equals the ambient pressure (P_{ambient}).
- **Case b (Choking at the throat):** When then ambient pressure (P_{ambient}) is further lowered, the flow reaches $M = 1$ just at the throat. The divergent part is still subsonic and adjusts to the ambient pressure with P_{exit} = P_{ambient} and M_{exit} < 1.
- **Case c (Normal shock in the diverging section):** When the ambient pressure is further lowered, M = 1 is achieved at the throat, followed by the acceleration to supersonic conditions right after the throat. Following this, a normal shock occurs in the diverging section across which the flow jumps

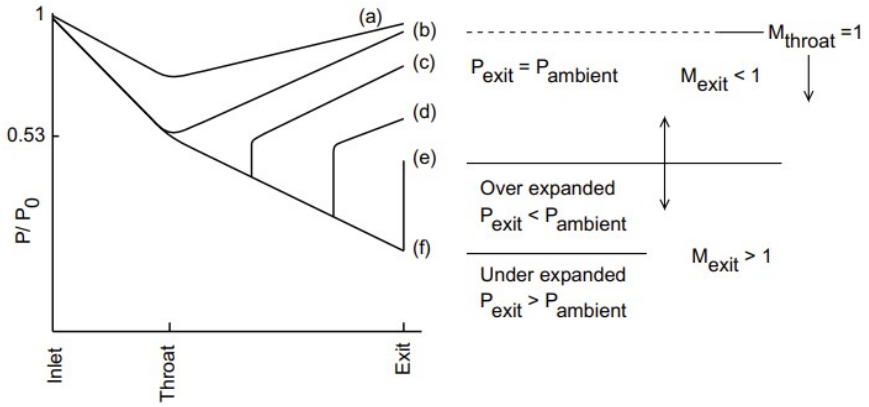

Figure 2.14: Variation of static pressure distribution in a converging diverging nozzle with varying back pressures at a fixed inlet stagnation condition [47].

back to sub-sonic conditions and decelerates to meet the imposed ambient pressure (P_{ambient}) at the exit.

- **Case d (Normal shock further downstream in the diverging section):** With further reduction in the ambient pressure, the location of the normal shock moves further downstream in the diverging section.
- **Case e (Normal shock at the exit of the nozzle):** When the ambient pressure is lowered further, the normal shock will stand right at the exit of the nozzle. At this condition, the flow just before the shockwave would have reached the maximum possible Mach number. The cases c,d and e are referred to as the over expanded cases as the exit pressure is less than the ambient pressure and the flow has to be compressed up to the ambient pressure by a normal shock wave.
- **Case f (Design condition - Shock free):** Lowering the back pressure a little more pushes the shock wave outside the nozzle and the exit Mach number becomes greater than 1.
- **Cases beyond f:** For cases beyond Case f, the flow does not expand enough and the exit pressure is too high $P_{\text{exit}} > P_{\text{ambient}}$. The flow is fully supersonic inside the nozzle and further undergoes expansion outside the nozzle in a typical shock-cell diamond pattern.

The theoretical framework discussed in this section is broadly applicable to compressible flows in varying area passage. However, these relations assume that the working fluid behaves as a calorically perfect gas (ideal gas with constant c_p, c_v and γ). Similar qualitative behaviour of choking and shock formation can be observed for the real gas flows such as for supercritical CO_2 in this case. However, the quantitative relations from the isentropic relations in this section no longer apply.

For supercritical CO_2, the thermodynamic properties should be obtained from the real gas equation of state such as the Span-Wagner equation of state so that the thermodynamic properties vary with the temperature and pressure. When the flow undergoes phase transition and two-phase flow sets in, the sonic conditions is also dependent on the mixture speed of sound and the minimum effective area of the flow and hence the sonic conditions may shift downstream of the geometric throat.

2.8. Multiphase Flow Models

Modelling interphase mass transfer phenomenon in CFD is a quite complex task, presenting significant challenges in numerical implementation. Two widely used approaches are the Euler-Euler approach and the Euler-Lagrange approach. Euler-Euler is the most widely used due to its simplicity and efficiency, where both the phase are represented by continuum flow fields. In contrast, Euler-Lagrange approach is more accurate yet computationally expensive, as here, the nucleating phase (liquid droplets for condensation and vapour bubbles for evaporation) is represented by discrete particles (Lagrangian approach) while the other phase is represented as a continuous flow field (Eulerian approach). However, the usage of Euler-Lagrange approach is very limited in literature for carbon dioxide due to numerical convergence issues arising from the complex interaction between discrete particles and the continuous phase. These challenges are further amplified near the critical point, where steep thermodynamic gradients increase numerical stiffness, making the solver convergence difficult. As a result, Euler-Euler approach has been the commonly preferred method in carbon dioxide phase transition simulations [36].

Within the two-phase models, there are several sub models depending on the manner the phases interact with each other. For the phase change processes with typically short time scales, the phase transition may not occur instantaneously at the saturation line and the fluid would venture into the metastable states. The models that account for this behaviour are referred to as delayed equilibrium models and on contrary the models considering instantaneous phase transition by excluding metastable states are called equilibrium models. There exists another classification based on the existence of mechanical, thermal and chemical equilibrium between the two-phases. The models accounting for equilibrium in these properties are called homogeneous models and those allowing non-equilibrium in atleast one of these aspects are called non-homogeneous models.

A plethora of two fluid models are available and the key models elaborated by De Lorenzo et al. [48] are outlined below,

- **Homogeneous Equilibrium Model (HEM):** Assumes mechanical and thermal equilibrium between the phases and excludes the presence of metastable states.
- **Non-Homogeneous Equilibrium Model (NEM):** Assumes existence of relative velocity between phases while considering thermal equilibrium. This model also excludes the presence of metastable states.
- **Homogeneous Frozen Model (HFM):** Assumes mechanical equilibrium but excludes thermal equilibrium and the excludes the presence of metastable states.
- **Delayed Equilibrium Model (DEM):** Allows for the existence of metastable states and considers only mechanical equilibrium between the phases.

Here, the fluid is assumed to be of single species and no chemical reaction was considered to take place. Hence, chemical equilibrium was not considered in the classification of above models.

The HEM model is the most widely used due to its simplicity and effectiveness for flow conditions near the critical point, where metastability effects are negligible. However, the accuracy of the HEM was found to diminish for the thermodynamic states far from the critical point [49].

The Mixture Model in *Ansys Fluent* is one of the frequently employed Euler-Euler model in CFD. This model treats the phases as interpenetrating continua and solves continuity, momentum and energy equation for the mixture. The model allows for existence of relative velocity between the phases, if the slip velocity is neglected, the model simplifies to a multiphase homogeneous model [50]. The phase change processes can be modelled using built in cavitation and evaporation-condensation models.

Yafei et al. [51] utilised the Mixture Model in *Ansys Fluent* to perform flow analysis in a transcritical CO_2 ejector. The phase change process was modelled using the Zwart-Gerber-Belamri cavitation model and the Lee evaporation-condensation model. The values for coefficients in these models were determined using sensitivity analysis. The predicted mass flow rates were more accurate than the predictions of HEM model. Giuseppe et al. [52] modelled the non-equilibrium condensation process in de Laval nozzles using Mixture Model in *Ansys Fluent*. The nucleation of droplets was modelled using a modified version of Classical Nucleation Theory and the mass transfer rate due to phase change was modelled using modified Hertz-Knudsen equation through a set of User Defined Scalar Transport equations. The study analysed two-phase shock waves in CO_2 flows and their sensitivity to thermodynamic conditions and geometric variations. Guojie et al. used Mixture Model in *Ansys Fluent* and the transport equations were modelled using User Defined Functions (UDF). Four different droplet growth models viz. Gyarmathy, Fuchs & Sutugin, Young and Hertz & Knudsen models were studied for condensing flow in nozzle. The Hertz-Knudsen model predicted rapid nucleation and condensation phenomenon indicated by rapid changes in the pressure profile. This discrepancy might have occurred because Hertz-Knudsen model is generally suitable for multi-component systems. Whereas the remaining three models were nearly consistent and Gyarmathy model exhibited the best agreement with the pressure profile [53]. Romei et al. simplified the Mixture Model into a Barotropic model assuming the thermodynamic properties to be function of pressure only, rather than both pressure and entropy. Both mechanical and thermal equilibrium were assumed and cavitating and condensing flows were simulated. There was good agreement in the pressure profiles between the Mixture and Barotropic models, but the computational cost was found to be much lower in the Barotropic model [38].

The HEM model, due to full equilibrium, was always shown to under predict the critical mass flow rate except in cases where characteristic speed is not a determining factor [54]. Hammer et al. [55] have developed a Delayed Homogeneous Equilibrium Model (D-HEM) which delays the onset of nucleation process until the fluid reaches the Super Heat Limit (SHL) as predicted by the Classical Nucleation Theory (CNT). Post the SHL, the fluid transitions into a full equilibrium state similar to HEM. The critical mass flux predicted by D-HEM was found to be more accurate (2.5% absolute error) than that of HEM model for the experiments of Hesson et al. [56] in orifices and Banasiak et al. [57] in nozzles. The effect of delayed phase transition was achieved using the HEM model itself by Zanzi et al. by using a workaround. The authors utilized experimentally determined Wilson line for phase transition instead of saturation line [36]. This approach resulted in good prediction of condensation onset but there was slight deviation in pressure profiles towards the end of divergent section of the nozzle.

Angielczyk et al. modelled two-phase flow of CO_2 through ejector motive nozzle using Homogeneous Relaxation Model (HRM). HRM belongs to the 4-equation models [58] and it arises from the fact that during phase transition, an instantaneous thermodynamic equilibrium cannot exist between the phases and a delay happens in the process which is quantified by the relaxation time, θ. They modified the Downar-Zapolski correlation [59] using the experimental data from Nakagawa [39] to make the relax-

ation time suitable for CO_2. 1-D simulation with the HRM model was shown to provide more consistent results than HEM model, however both the models exhibited high deviation in pressure profiles for smaller divergence angles [60]. The HRM model was used in a density based solver by Metsue et al. [61]. The study also employed bicubic interpolation scheme in the tabulated EOS which improved the accuracy and speed of interpolation. Various relaxation times (using constant values and correlation from Angielczyk [60]) were used in the simulation and it was found that a single value of relaxation time was not sufficient for the entirety of the nozzle and was also highly case dependent.

A Delayed HRM (D-HRM) model was employed by Wilhelmsen et al. where the delay in phase transition was governed using the limits of metastability predicted by the homogeneous nucleation theory. The crossover between homogeneous and heterogeneous nucleation was found to occur at 285K for CO_2. Below this temperature, heterogeneous nucleation was found to dictate the nucleation process and the nucleation work was calculated by multiplying the homogeneous nucleation work with a work reduction factor (ϕ) which varies from 0 to 1. The D-HRM model was found to perform better than HRM model for choked flow of CO_2 in nozzles [62]. A correlation for the work reduction factor was developed and validated by Banasiak et al. [57].

The relaxation parameter in HRM model relies on empirical coefficients and has to be fitted on a case by case basis but the Homogeneous Flashing Model (HFM) model was found to be much more predictive. Log et al. had proposed the Homogeneous Flashing Model by taking into account the fundamental phenomena in the flashing process viz. homogeneous and heterogeneous nucleation, bubble coalescence, breakup and growth. The homogeneous nucleation process was modelled using the Classical Nucleation Theory (CNT) and the heterogeneous nucleation was modelled considering constant rate of bubble creation and liquid to vapour mass transfer [63]. Heterogeneous nucleation was seen to cause the bubble formation and growth for the cold cases whereas for warm cases both homogeneous and heterogeneous nucleation was found to contribute to the bubble formation and growth. An accurate model for heterogeneous nucleation is required for HFM in order to make it fully predictive. A physics based model for heterogeneous nucleation in water was developed by Shin et al. considering nucleation, growth and bubble departure from cavity, bubble transport to the throat and void development downstream of the throat. The critical mass flow rate predicted with this model was found to be within 3% of the experimental values [64].

While the HEM model remains to be the widely used model for its simplicity, its ability to capture metastable states and delayed phase transition limits its accuracy far from the critical point. The delayed equilibrium and relaxation based models perform well in these conditions, but rely on use of empirical coefficients which has to be fitted on case to case basis, limiting their predictive robustness. The HFM model is a better physics oriented model, considering the nucleation mechanisms but utilises an empirical approach for heterogeneous nucleation. A summary of the common multiphase models is given in Table 2.1. Fully predictive multiphase flow models for CO_2 flashing had to rely on the development of accurate governing equations for heterogeneous nucleation process.

Table 2.1: Summary of common multiphase flow models and their treatment of thermodynamic and phase change behaviours.

Flow Model	Mechanical Equilibrium	Thermal Equilibrium	Metastable State	Metastability Limit
Homogeneous Equilibrium Model (HEM)	Yes	Yes	No	Not Applicable
Non-Homogeneous Equilibrium Model (NEM)	No	Yes	No	Not Applicable
Homogeneous Frozen Model (HFM)	Yes	No	No	Not Applicable
Mixture Model	Subjective	Yes	User defined	User defined
Barotropic Model	Yes	Yes	No	Not Applicable
Delayed-Homogeneous Equilibrium Model (D-HEM)	Yes	Yes	Yes	Superheat limit from Classical Nucleation Theory
Homogeneous Relaxation Model (HRM)	Yes	Yes	Yes	Empirical relaxation time
Delayed Homogeneous Relaxation Model (D-HRM)	Yes	No	Yes	Homogeneous nucleation via Classical Nucleation Theory; Heterogeneous nucleation via work reduction factor
Homogeneous Flashing Model (HFM)	Yes	Yes	Yes	Homogeneous nucleation via Classical Nucleation Theory; Heterogeneous nucleation via constant bubble creation rate

3

Methodology

This chapter details the computational framework developed for modelling the flow behaviour of supercritical carbon dioxide in converging–diverging nozzles. Building upon Bob Fluttert's work [16], enhancements have been introduced to improve the robustness and accuracy of the simulations at supercritical conditions. These include the construction of a non-uniform lookup table for the Span–Wagner equation of state with refinement near the critical point. Following this, corresponding modifications were made to the User Defined Function (UDF) and User Defined Real Gas Model (UDRGM) to incorporate the Span-Wager Equation of State in *Ansys Fluent*.

To address the numerical stability challenges near the critical point, a Savitzky–Golay filtering technique was applied to smooth the thermodynamic property tables while preserving the key physical trends. The Zwart–Gerber–Belamri (ZGB) cavitation model was extended to incorporate turbulence effects and a sensitivity study was performed to study the effects of bubble radius in the cavitation model. Additionally, the effect of surface tension on cavitation behaviour was investigated. The simulation framework was also extended from a quasi-one-dimensional configuration to a two-dimensional domain to better capture the flow physics.

The sections that follow describe the geometry, boundary conditions, meshing strategy, real gas modeling approach, multiphase flow treatment, and numerical methods in detail. An overview of the simulation framework is illustrated in Figure 3.1.

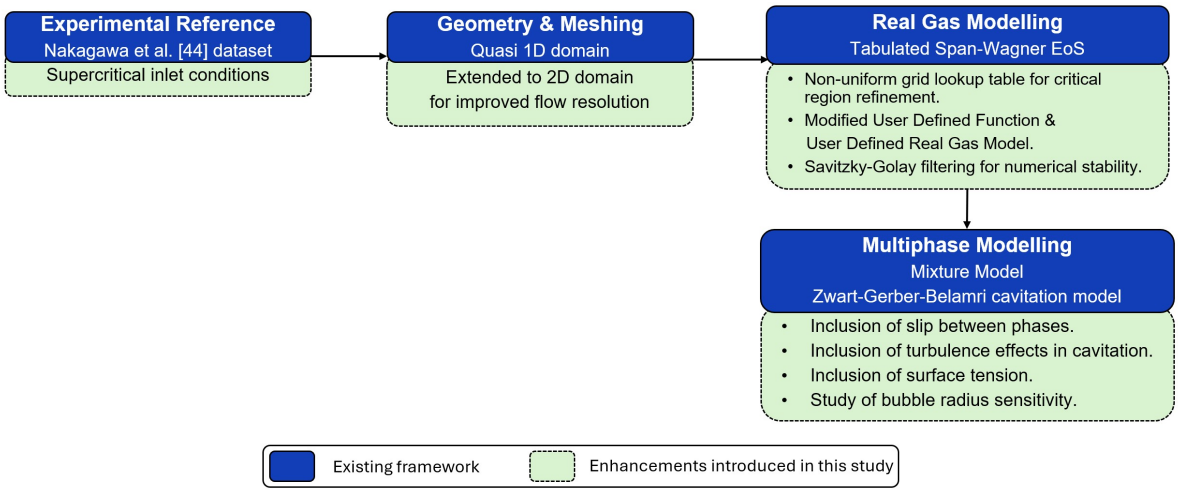

Figure 3.1: Flowchart summarizing the computational methodology developed in this study. The blue boxes indicate the methodology adopted from the predecessor's (Bob Fluttert [16]) framework, while the annotations in green highlight the key enhancements introduced in the present work.

3.1. Mixture Multiphase Model

As discussed in the Section 2.8, the Euler-Euler approach has been chosen for this study owing to its reasonable balance between accuracy and computational efficiency when compared to the Euler-Lagrange approach. Three different Euler-Euler models are available in *Ansys Fluent*: the Volume of Fluid (VOF) model, mixture model and the Eulerian model. Given that the expected flow regime in this case is bubbly, the mixture model is considered the most appropriate due to its simplified yet robust formulation for handling dispersed multiphase flows.

In mixture model, all the phases are treated as interpenetrating continua. This can model multiple phases by solving the continuity, momentum and energy equations for the mixture, along with a volume fraction equation for the secondary phase and the algebraic expression for the relative (drift) velocity. It can be used to model both homogeneous flows (where strong coupling exists between phases and they move with the same velocity) and flows where the phases move with different velocities.

The continuity equation of the mixture is given by,

$$\frac{\partial \rho_m}{\partial t} + \nabla \cdot (\rho_m \mathbf{v}_m) = 0 \tag{3.1}$$

where $\mathbf{v}_m$ is the mass-averaged velocity:

$$\mathbf{v}_m = \frac{\alpha_l \rho_l \mathbf{v}_l + \alpha_v \rho_v \mathbf{v}_v}{\rho_m} \tag{3.2}$$

and ρ_m is the mixture density:

$$\rho_m = \alpha_l \rho_l + \alpha_v \rho_v \tag{3.3}$$

where,

- $\mathbf{v}_m$ is the mass-averaged mixture velocity
- α_l is the volume fraction of the liquid phase
- α_v is the volume fraction of the vapour phase $(\alpha_l + \alpha_v = 1)$
- ρ_l is the density of the liquid phase
- ρ_v is the density of the vapour phase
- $\mathbf{v}_l$ is the velocity of the liquid phase
- $\mathbf{v}_v$ is the velocity of the vapour phase
- ρ_m is the mixture density

The mixture momentum equation is obtained by summing the individual momentum equations for all phases. It can be expressed as,

$$\frac{\partial}{\partial t}\left(\rho_m \mathbf{v}_m\right) + \nabla \cdot \left(\rho_m \mathbf{v}_m \otimes \mathbf{v}_m\right) = -\nabla p + \nabla \cdot \left[\mu_m \left(\nabla \mathbf{v}_m + \left(\nabla \mathbf{v}_m\right)^T\right)\right] + \rho_m \mathbf{g} + \mathbf{F}_{\text{st}} - \nabla \cdot \left(\alpha_v \rho_v \mathbf{v}_{dr,v} \otimes \mathbf{v}_{dr,v}\right) \tag{3.4}$$

where,

- F_{st} is the surface tension force at the liquid–vapour interface,
- μ_m is the viscosity of the mixture, given by,

$$\mu_m = \alpha_l \mu_l + \alpha_v \mu_v \tag{3.5}$$

- $\mathbf{v}_{dr,v}$ is the drift velocity for the vapour phase, defined as,

$$\mathbf{v}_{dr,v} = \mathbf{v}_v - \mathbf{v}_m \tag{3.6}$$

The energy equation for the mixture in its general form is given by,

$$\begin{aligned} &\frac{\partial}{\partial t}\left(\alpha_l \rho_l E_l + \alpha_v \rho_v E_v\right) + \nabla \cdot \left[\alpha_l \mathbf{v}_l \left(\rho_l E_l + p\right) + \alpha_v \mathbf{v}_v \left(\rho_v E_v + p\right)\right] \\ &\qquad = \nabla \cdot \left(k_{\text{eff}} \nabla T - \sum_k h_k \mathbf{J}_k + \overline{\overline{\tau}}_{\text{eff}} \cdot \mathbf{v}_m\right) + S_h \end{aligned} \tag{3.7}$$

where,

- α_l, α_v are the volume fractions of liquid and vapour phases ($\alpha_l + \alpha_v = 1$),
- ρ_l, ρ_v are the densities of liquid and vapour phases,
- $\mathbf{v}_l, \mathbf{v}_v$ are the velocities of liquid and vapour phases,
- E_l, E_v are the total energy of liquid and vapour phases,
- k_{eff} is the effective thermal conductivity of the mixture, given by

$$k_{\text{eff}} = \alpha_l (k_l + k_t) + \alpha_v (k_v + k_t), \tag{3.8}$$

  where k_t denotes the turbulent thermal conductivity, calculated from the turbulence model used in the simulation (SST k–ω),

- $\sum_k h_k \mathbf{J}_k$ is the enthalpy transport due to species diffusion within phase k,
- $\overline{\boldsymbol{\tau}}_{\text{eff}}$ is the effective stress tensor accounting for viscous and turbulent stresses,
- S_h is the volumetric heat source.

In the present study, since carbon dioxide is treated as a single chemical species in both phases, there are no concentration gradients to drive species diffusion. Furthermore, no external volumetric heat source is applied to the system ($S_h = 0$). Consequently, the terms $\sum_k h_k \mathbf{J}_k$ and S_h vanish, and Equation 3.7 simplifies to:

$$\begin{aligned} \frac{\partial}{\partial t}\left(\alpha_l \rho_l E_l + \alpha_v \rho_v E_v\right) + \nabla \cdot \left[\alpha_l \mathbf{v}_l \left(\rho_l E_l + p\right) + \alpha_v \mathbf{v}_v \left(\rho_v E_v + p\right)\right] \\ = \nabla \cdot \left(k_{\text{eff}} \nabla T + \overline{\boldsymbol{\tau}}_{\text{eff}} \cdot \mathbf{v}_m\right) \end{aligned} \tag{3.9}$$

The total energy for the liquid phase is given by,

$$E_l = h_l - \frac{p}{\rho_l} + \frac{|\mathbf{v}_l|^2}{2}. \tag{3.10}$$

The total energy for the vapour phase is given by,

$$E_v = h_v - \frac{p}{\rho_v} + \frac{|\mathbf{v}_v|^2}{2}. \tag{3.11}$$

where, h_l and h_v are the sensible enthalpies for liquid and vapour phases respectively.

In this study, the liquid phase has been considered as the primary phase and the vapour phase has been considered as the secondary phase. The volume fraction of the secondary phase is obtained from the continuity equation of the secondary phase and is given by,

$$\frac{\partial}{\partial t}\left(\alpha_v \rho_v\right) + \nabla \cdot \left(\alpha_v \rho_v \mathbf{v}_m\right) = -\nabla \cdot \left(\alpha_v \rho_v \mathbf{v}_{dr,v}\right) + \left(\dot{m}_{lv} - \dot{m}_{vl}\right) \tag{3.12}$$

In the mixture model, the relative motion between the primary and secondary phases is given by the slip velocity. The slip (or relative) velocity, $\mathbf{v}_{vl}$, is defined as the velocity difference between the secondary phase (v) and the primary phase (l):

$$\mathbf{v}_{vl} = \mathbf{v}_v - \mathbf{v}_l. \tag{3.13}$$

Ansys Fluent uses an algebraic slip formulation in its mixture model. This assumes that a local equilibrium is rapidly established between phases over a small length scale, allowing the slip velocity to be described algebraically. Following the approach by Manninen et al. [65], the slip velocity is computed as,

$$\mathbf{v}_{vl} = \frac{\tau_v}{f_{\text{drag}}} \left(\frac{\rho_v - \rho_m}{\rho_v}\right) \mathbf{a} \tag{3.14}$$

where,

- τ_v is the particle relaxation time of the vapour phase, given by

$$\tau_v = \frac{\rho_v d_v^2}{18\mu_l}, \tag{3.15}$$

- f_{drag} is the drag function accounting for interphase momentum transfer, typically defined using the Schiller–Naumann correlation:

$$f_{\text{drag}} = \begin{cases} 1 + 0.15\,\mathrm{Re}_{vl}^{0.687}, & \mathrm{Re}_{vl} \leq 1000, \\ 0.0183\,\mathrm{Re}_{vl}, & \mathrm{Re}_{vl} > 1000, \end{cases} \tag{3.16}$$

- $\mathbf{a}$ is the acceleration of the dispersed vapour phase.

In turbulent flows, additional dispersion due to turbulent fluctuations is also incorporated. *Ansys Fluent* modifies the slip velocity to include a diffusion term in the momentum equation, resulting in the following enhanced expression:

$$\mathbf{v}_{vl} = \left(\frac{(\rho_v - \rho_m)\, d_v^2}{18\mu_l f_{\text{drag}}} \right) \mathbf{a} - \frac{\eta_t}{\sigma_t} \left(\frac{\nabla \alpha_v}{\alpha_v} - \frac{\nabla \alpha_l}{\alpha_l} \right), \tag{3.17}$$

where,

- η_t is the turbulent diffusivity,
- σ_t is the turbulent Schmidt number (typically $\sigma_t = 0.75$),
- α_v, α_l is the volume fractions of vapour and liquid phases, respectively.

The turbulent diffusivity η_t is calculated as,

$$\eta_t = C_\mu \frac{k^2}{\epsilon} \left(\frac{\gamma_\gamma}{1 + \gamma_\gamma} \right) \left(1 + C_\beta \zeta_\gamma^2 \right)^{-1/2} \tag{3.18}$$

where,

- k is the turbulence kinetic energy,
- ϵ is the turbulence dissipation rate,
- γ_γ is the ratio of the turbulent eddy time scale to the particle relaxation time, incorporating trajectory crossing effects,
- C_μ is the turbulence model constant.

The parameter ζ_γ is defined as,

$$\zeta_\gamma = \frac{|\mathbf{v}_{vl}|}{\sqrt{\frac{2}{3}k}} \tag{3.19}$$

where $\mathbf{v}_{vl} = \mathbf{v}_v - \mathbf{v}_l$ is the relative (slip) velocity between the vapour and liquid phases.

The model coefficient C_β is computed as,

$$C_\beta = 1.8 - 1.35 \cos^2 \theta \tag{3.20}$$

where θ is the angle between the slip velocity $\mathbf{v}_{vl}$ and the velocity of the dispersed (vapour) phase $\mathbf{v}_v$, given by,

$$\cos\theta = \frac{\mathbf{v}_{vl} \cdot \mathbf{v}_v}{|\mathbf{v}_{vl}|\,|\mathbf{v}_v|}. \tag{3.21}$$

When slip velocity is not solved, the mixture model behaves as a homogeneous equilibrium model where all phases move with the same velocity. However, when relative motion is significant (e.g., in bubbly or particle-laden flows), enabling the slip formulation improves the solution by accounting for interphase momentum exchange.

With the governing multiphase framework established, the next step involves incorporating interfacial effects such as surface tension, which significantly influence phase change dynamics.

3.2. Surface Tension Model

The Eulerian multiphase model also enables the inclusion of surface tension effects along the interface between the primary and secondary phases. In the present study, the surface tension of carbon dioxide has been estimated using the Brock and Bird surface tension model, which uses a semi-empirical formulation based on the corresponding-states method [66]. The method utilizes critical pressure, temperature and volume to estimate the surface tension of pure carbon dioxide. This formulation has shown strong agreement with the experimental data, yielding an Absolute Average Percentage Deviation (AAPD) of just 5.13% which is significantly lower when compared to other predictive correlations.

The Brock and Bird correlation for surface tension is given by,

$$\sigma = \left(-0.951 + \frac{0.432}{Z_c}\right)(1 - T_r)^{11/9}\left(P_c^2 T_c\right)^{1/3} \tag{3.22}$$

The terms Z_c and T_r are the critical compressibility factor and reduced temperature respectively and are expressed as,

$$Z_c = \frac{P_c V_c}{R T_c} \tag{3.23}$$

$$T_r = \frac{T}{T_c} \tag{3.24}$$

where T is the absolute temperature and R is the universal gas constant. P_c, T_c and V_c are the critical pressure, temperature and volume of the liquid. The Brock and Bird correlation was implemented through a User Defined Function (UDF) and integrated into the simulation via the surface tension dialog box within the mixture multiphase model interface in *Ansys Fluent*. The source code for the surface tension UDF has been provided in Appendix A.

3.3. Surface Tension Models in Ansys Fluent

Ansys Fluent offers two formulations for modeling surface tension namely, the Continuum Surface Force (CSF) model and the Continuum Surface Stress (CSS) model.

3.3.1. Continuum Surface Force Model

The Continuum Surface Force (CSF) model, originally proposed by Brackbill et al., [67] represents surface tension as a volumetric force distributed across the interface, rather than as a boundary condition. In the simplest case with constant surface tension and purely normal interfacial forces, the pressure jump across the interface is given by,

$$p_2 - p_1 = \sigma \left(\frac{1}{R_1} + \frac{1}{R_2} \right) \tag{3.25}$$

where σ is the surface tension coefficient, and R_1 and R_2 are the radii of curvature in orthogonal directions. The curvature is computed from the local gradients in the surface normal at the interface.

The surface normal $\mathbf{n}$ is defined as the gradient of α_q, the volume fraction of the q^{th} phase and is computed as,

$$\mathbf{n} = \nabla \alpha_q, \tag{3.26}$$

$$\hat{\mathbf{n}} = \frac{\mathbf{n}}{|\mathbf{n}|}, \tag{3.27}$$

$$\kappa = \nabla \cdot \hat{\mathbf{n}}, \tag{3.28}$$

where $\hat{\mathbf{n}}$ is the unit normal vector and κ is the interface curvature.

Using the divergence theorem, the surface force can be converted into a volumetric source term in the momentum equation. The general form of the surface tension force for multiple phases is,

$$\mathbf{F}_{\text{vol}} = \sum_{\substack{\text{pairs } i,j \\ i<j}} \sigma_{ij} \frac{\alpha_i \rho_i \kappa_j \nabla \alpha_j + \alpha_j \rho_j \kappa_i \nabla \alpha_i}{\frac{1}{2}(\rho_i + \rho_j)}, \tag{3.29}$$

where σ_{ij} is the surface tension coefficient between phases i and j, and ρ_i, ρ_j are the densities of phases i and j, respectively.

For a two-phase system, where $\kappa_i = -\kappa_j$ and $\nabla \alpha_i = -\nabla \alpha_j$, this expression simplifies to,

$$\mathbf{F}_{\text{vol}} = \sigma_{ij} \frac{\rho \kappa_i \nabla \alpha_i}{\frac{1}{2}(\rho_i + \rho_j)}, \tag{3.30}$$

where ρ is the volume-averaged density in the cell. Although the CSF model is straightforward, it is known to introduce artificial currents in the solution and is valid strictly under the assumption of constant surface tension. For cases involving variable surface tension, additional terms in the tangential direction are required to model surface tension gradients.

3.3.2. Continuum Surface Stress Model

To overcome the limitations of the CSF model, especially for variable surface tension applications, the Continuum Surface Stress (CSS) model is used in this study. Unlike the CSF method, the CSS model incorporates surface tension in a conservative manner by computing the surface stress tensor directly, thereby avoiding the explicit calculation of curvature.

The CSS model expresses the surface stress tensor due to surface tension as,

$$\mathbf{T} = \sigma \left(\mathbf{I} - \hat{\mathbf{n}} \otimes \hat{\mathbf{n}} \right) |\mathbf{n}|, \tag{3.31}$$

Here,

- $\mathbf{I}$ is the unit tensor,
- σ is the surface tension coefficient,
- $\hat{\mathbf{n}}$ is the unit normal vector to the interface,
- $\mathbf{n} = \nabla \alpha$ is the gradient of the volume fraction field.

Alternatively, this can be written in compact form as,

$$\mathbf{T} = \sigma \left(|\nabla \alpha| \mathbf{I} - \frac{\nabla \alpha \otimes \nabla \alpha}{|\nabla \alpha|} \right). \tag{3.32}$$

The volumetric surface tension force is then obtained as the divergence of this stress tensor,

$$\mathbf{F}_{\text{CSS}} = \nabla \cdot \mathbf{T}. \tag{3.33}$$

The CSS method offers distinct advantages over the CSF model, particularly for flows involving variable surface tension such as in the present study, where surface tension is computed based on the Brock and Bird model. Unlike the CSF approach, which requires curvature calculation and becomes inaccurate in under-resolved regions, the CSS method inherently accommodates variable surface tension without any additional source terms. It also avoids numerical instabilities near sharp corners by using a conservative formulation that does not require explicit curvature calculation. Instead, it models surface tension through a surface stress tensor based on volume fraction gradients, which smooths forces and reduces sensitivity to sharp curvature changes. This makes the method more stable and physically accurate in under-resolved regions.

Therefore, due to its robustness and compatibility with variable surface tension inputs, the CSS model was adopted for the surface tension simulations in this work.

Accurate prediction of the flow field in multiphase flows also requires an appropriate turbulence closure model which will be discussed in the upcoming section.

3.4. Turbulence Modeling

The Reynolds-Averaged Navier–Stokes (RANS) approach is employed in this study due to its balance between computational efficiency and physical accuracy. These models solve the time-averaged Navier-Stokes equation, incorporating additional transport equations to account for the effects of turbulence. They are significantly less demanding in terms of mesh resolution and time-step sensitivity than computationally intensive approaches such as Large Eddy Simulation (LES) or Direct Numerical Simulation (DNS). Hence, they are appropriate for steady-state engineering problems.

The internal flow of supercritical carbon dioxide in the converging-diverging nozzle involves boundary layer development and flow separation in the diverging section. While such flows are inherently

unsteady at fine scales, the primary interest of this investigation lies in the accurate prediction of time-averaged flow quantities such as pressure and Mach number distribution, rather than transient turbulent structures. Hence, it was decided that RANS models would be sufficient for this study to capture the flow physics with reasonable computational resources.

Among the subset of RANS models, the two-equation Shear Stress Transport (SST) k–ω turbulence model was used to simulate the turbulent flow characteristics within the nozzle. This model is more accurate than the standard k–ω model for adverse pressure gradient flows.

The SST k–ω model blends the near-wall accuracy of the standard k–ω model with the robustness of the k–ε model in the free-stream region, combining the advantage of both the formulations. This is achieved through a blending function, F_1, which enables a smooth transition between the two formulations. As a result, the model provides enhanced predictive capabilities for flows involving strong shear layers or separations without the need for empirical damping functions or wall functions [68].

The governing transport equations for the turbulence kinetic energy (k) and the specific dissipation rate (ω) in the SST formulation are given by [69],

$$\frac{\partial(\rho k)}{\partial t} + \frac{\partial(\rho u_j k)}{\partial x_j} = P - \beta^* \rho \omega k + \frac{\partial}{\partial x_j}\left[(\mu + \sigma_k \mu_t)\frac{\partial k}{\partial x_j}\right] \tag{3.34}$$

$$\frac{\partial(\rho \omega)}{\partial t} + \frac{\partial(\rho u_j \omega)}{\partial x_j} = \frac{\gamma}{\mu_t} P - \beta \rho \omega^2 + \frac{\partial}{\partial x_j}\left[(\mu + \sigma_\omega \mu_t)\frac{\partial \omega}{\partial x_j}\right] + 2(1 - F_1)\frac{\rho \sigma_{\omega 2}}{\omega}\frac{\partial k}{\partial x_j}\frac{\partial \omega}{\partial x_j} \tag{3.35}$$

Here, P denotes the production of turbulence kinetic energy, μ is the molecular viscosity, and μ_t is the eddy viscosity. In the SST model, a viscosity limiter is included as in Equation 3.36, which resulted in better agreement with experimental measurements of separated flow.

In the Equation 3.35, the blending function F_1 tends to a value of 1 near the wall, behaving as k–ω model and it tends to 0 away from the wall, transitioning into k–ε model.

$$\mu_t = \frac{\rho a_1 k}{\max(a_1 \omega, S F_2)} \tag{3.36}$$

where S is the strain rate magnitude and F_2 is a secondary blending function used to limit the eddy viscosity in the presence of high shear. This formulation enables the SST model to remain responsive in both attached and separated flow regions.

The selection of the SST k–ω model in this work is thus motivated by its proven accuracy in resolving pressure gradients and flow separation, such as those encountered in high-speed nozzle expansions.

3.5. Mass Transfer Models

Under the thermodynamic process conditions considered in this study, carbon dioxide enters the nozzle in a supercritical state. As the supercritical carbon dioxide flows through the converging-diverging nozzle, rapid depressurisation occurs. During this process, the local pressure may drop below the vapour pressure corresponding to the local temperature. This leads to phase transition from liquid phase to

vapour phase. This phenomenon, known as flashing, results in formation of vapour bubbles. Subsequently, in the regions where pressure recovery occurs, such as the downstream of the shockwave, the local pressure may rise above the vapour pressure. This causes the formed vapour bubbles to become unstable and implode, transitioning back into the liquid phase. This phenomenon is referred to as cavitation.

3.6. Zwart-Gerber-Belamri Cavitation Model

To accurately predict the onset of phase transition, Zwart-Gerber-Belamri cavitation model has been employed in this study.

The liquid vapour mass transfer is governed by the vapour transport equation, which is expressed as,

$$\frac{\partial}{\partial t}(\alpha\rho_v) + \nabla \cdot (\alpha\rho_v \mathbf{v}_v) = R_e - R_c \tag{3.37}$$

where,

- v = vapor phase
- α = vapor volume fraction
- ρ_v = vapor density
- $\mathbf{V}_v$ = vapor phase velocity
- R_e, R_c = mass transfer source terms related to the growth and collapse of vapor bubbles, respectively

The mass transfer source terms R_e and R_c account for mass transfer between the liquid and vapour phases and are modelled based on the Rayleigh-Plesset equation which is given by [70],

$$R_b \frac{D^2 R_b}{Dt^2} + \frac{3}{2}\left(\frac{DR_b}{Dt}\right)^2 = \frac{P_b - P}{\rho_l} - \frac{4\nu_l}{R_b}\frac{DR_b}{Dt} - \frac{2\sigma}{\rho_l R_b} \tag{3.38}$$

where,

- R_b is the radius of the vapor bubble
- P_b is the bubble surface pressure
- P is the local far-field pressure
- ρ_l is the density of the liquid phase
- ν_l is the kinematic viscosity of the liquid
- σ is the liquid surface tension coefficient

By neglecting the surface tensions forces and second-order inertial terms, the Rayleigh-Plesset equation simplifies to,

$$\frac{DR_b}{Dt} = \sqrt{\frac{2}{3} \cdot \frac{P_b - P}{\rho_l}} \tag{3.39}$$

By assuming that all the bubbles in the system have a uniform radius, Zwart-Gerber-Belamri expressed the total mass transfer rate (R) using the below relation [71].

$$R = n_b \times \left(4\pi R_b^2 \rho_v \frac{DR_b}{Dt}\right) \tag{3.40}$$

The volume fraction of the vapour (α) is related to the bubble number density (n_b) and the bubble radius (R_b) through,

$$\alpha = n_b \times \left(\frac{4}{3}\pi R_b^3\right) \tag{3.41}$$

Combining the Equations 3.40 and 3.41 yields the expression for net mass transfer,

$$R = \frac{3\alpha\rho_v}{R_b}\sqrt{\frac{2}{3}\cdot\frac{P_b - P}{\rho_l}} \tag{3.42}$$

Replacing the vapour volume fraction (α) with the nucleation site density (α_{nuc}), the evaporation and condensation mass transfer rates can be expressed as follows.

If the local pressure falls below the vapour pressure of the liquid ($P < P_v$) evaporation occurs,

$$R_e = F_{\text{vap}}\frac{3\alpha_{\text{nuc}}(1-\alpha_v)\rho_v}{R_b}\sqrt{\frac{2}{3}\cdot\frac{P_v - P}{\rho_l}} \tag{3.43}$$

Whereas when the local pressure increases above the vapour pressure of the liquid ($P > P_v$) condensation occurs,

$$R_c = F_{\text{cond}}\frac{3\alpha_v\rho_v}{R_b}\sqrt{\frac{2}{3}\cdot\frac{P - P_v}{\rho_l}} \tag{3.44}$$

where,

- R_b is the bubble radius, typically 10^{-6} m
- α_{nuc} is nucleation site volume fraction, typically 5×10^{-4}
- F_{vap} is the evaporation coefficient (default value: 50)
- F_{cond} is the condensation coefficient (default value: 0.01)
- ρ_v is the vapor density
- ρ_l is the liquid density
- P_v is the vapor pressure (saturation pressure)
- P is the local pressure
- α_v is the vapour volume fraction

The evaporation and condensation coefficients (F_{vap} & F_{cond}) govern the rate of phase change processes. Higher values of these coefficients result in an increased rate of evaporation & condensation mass transfer between liquid & vapour phases.

The driving force for the phase transition in this model is the vapor pressure of the fluid, which determines the onset of evaporation and condensation processes. In the present study, the saturation pressure has been provided as the input by using a User Defined Function (UDF). Notably, the default saturation curve terminates at the critical point of carbon dioxide which is at 7.38 MPa and 304.13 K. However, the expansion process considered in this study is happening from a supercritical state, so a boundary to delineate the liquid-like and vapour-like behaviour in the supercritical region is required. This pseudo-boiling curve in the supercritical region is referred to as the Widom line[72].

3.6.1. Construction of Widom Line

The Widom line corresponds to the conceptual boundary in the pressure-temperature ($P-T$) phase diagram that extends from the critical point into the supercritical region and is constructed by connecting the extrema of key thermodynamic functions such as the specific heat capacity.

In the current study, isobaric specific heat capacity (C_p) has been used for the construction of the Widom line. The Widom line has been constructed by evaluating the value of C_p at various pressures and temperatures above the critical point and connecting the points where the maxima of C_p occurs. The methodology of Widom line construction has been depicted in Figure 3.2.

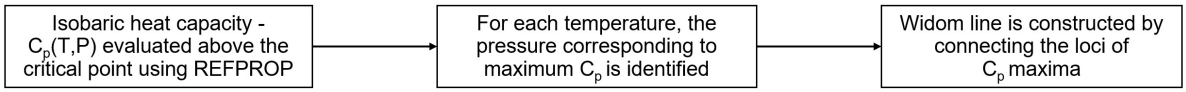

Figure 3.2: Methodology adopted for the construction of Widom line.

Figure 3.3 depicts the combined saturation line and Widom line. The saturation line delineates the liquid and vapour phases in the sub-critical region, whereas the Widom line delineates the regions with liquid-like and vapour-like behaviour in the supercritical region. The combined saturation and Widom line has been used as the vaporization pressure input (the term P_v in Equations 4.8 and 4.9) for the ZGB cavitation model in this study.

Widom line is also known as the pseudo-boiling curve. Although no true phase change occurs across this line, it delineates a boundary separating liquid-like and vapour-like behaviour in supercritical fluids. At pressures and temperatures above the Widom line, supercritical CO_2 exhibits liquid-like characteristics, while below it, vapour-like properties dominate [73]. In this context, the extended saturation curve defined by the Widom line provides a more physically realistic framework for modelling pseudo phase change behaviour during rapid expansion of CO_2 in the nozzle from a supercritical state. The usage of Widom line in the ZGB cavitation model introduces a limitation of artificial vapor formation whenever the expansion path crosses the Widom line in the supercritical region. However, no actual phase transition occurs in this process, as true phase change only takes place along the saturation line. Consequently, the vapor fraction predicted by *Ansys Fluent* cannot be directly interpreted for physical inference. Instead, it must be post-processed based on the enthalpy corresponding to each thermodynamic state, as detailed in the following chapter.

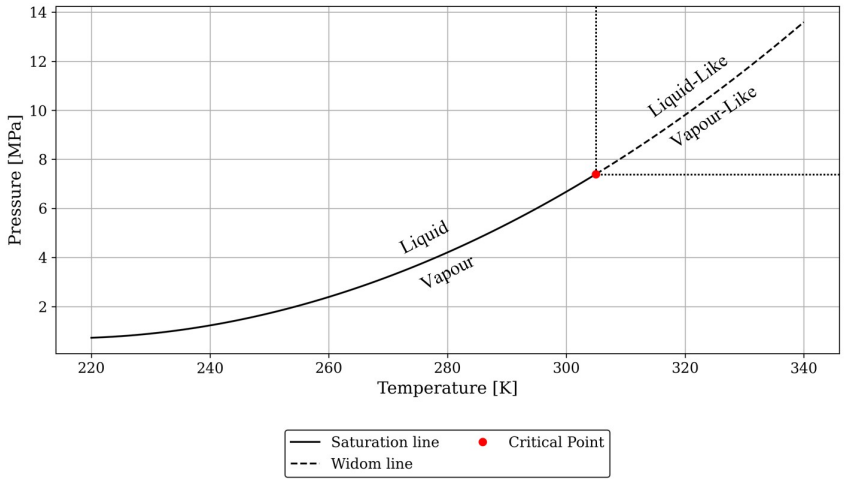

Figure 3.3: Saturation pressure curve and Widom line for carbon dioxide plotted on the pressure–temperature diagram. The saturation line (solid) terminates at the critical point (red marker), beyond which the Widom line (dashed) extends into the supercritical region. The Widom line, constructed as the locus of specific heat maxima, separates the regions with liquid-like and vapour-like behaviour in supercritical CO_2.

The effect of turbulence on the vaporization pressure can be included in the Zwart-Gerber-Belamri model by using the below relationship formulated by Yang et al. [74].

$$P_v = P_{\text{sat}} + \frac{1}{2}\,(\text{coeff})\,\rho_l\,k_l \tag{3.45}$$

where ρ_l and k_l represent the liquid phase density and turbulence kinetic energy, respectively. The term $coeff$ is a calibration constant that adjusts how strongly the turbulence fluctuations influence the local vaporization pressure. The recommended value for $coeff$ is 0.39 by the *Ansys Fluent* theory guide [50], and this value has been used by default.

3.6.2. Bubble Radius in Zwart-Gerber-Belamri Cavitation Model

The ZGB model simplifies the modelling of cavitation process by assuming a constant bubble radius throughout the vaporisation and condensation phases. The minimum possible radius of a bubble can be quantified by the critical radius. Physically, the critical bubble radius represents the minimum size above which a bubble can remain thermodynamically stable and grow, while bubbles smaller than this threshold are energetically unstable and tend to collapse. The critical bubble radius is related to the Super Heat Limit (SHL), saturation pressure and surface tension by the following relation [55]. The Super Heat Limit (SHL) is the maximum temperature up to which the liquid can exist in metastable state before it vaporizes spontaneously.

$$r^* = \frac{2\sigma}{P_{\text{sat}}(T_\ell) - P_{SHL}} \tag{3.46}$$

where,

- r^* is the critical radius of the bubble
- σ is the surface tension coefficient (Brock and Bird correlation has been used in this study)

- $P_{\text{sat}}(T_\ell)$ is the saturation pressure at the liquid temperature T_ℓ
- P_{SHL} is the pressure corresponding to the Superheat Limit (SHL)

Figure 3.4 illustrates the variation of the critical bubble radius with temperature. In the present simulation, the phase change is initiated near the throat region, where the static temperature is approximately 304 K. Accordingly, the critical bubble radius was evaluated to be 1.13×10^{-7} m at this temperature and has been taken as the minimum bubble radius that needs to be used in the ZGB cavitation model.

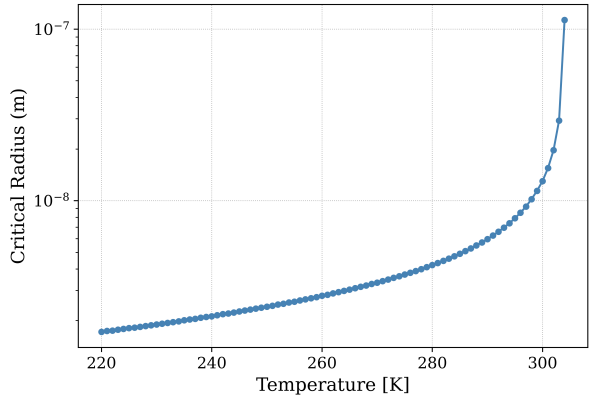

Figure 3.4: Variation of critical bubble radius with temperature calculated using the Equation 3.46. In the current study, the phase change process initiates at the throat around 304 K for which the critical bubble radius is 1.13×10^{-7} m.

3.7. Tabulated Equation of State

As elaborated in the Section 2.3.3, Span-Wagner equation of state has been chosen due to its accurate estimation of thermodynamic properties of CO_2 over a wide range of temperatures and pressures. However, the Span-Wagner EOS is not available in *Ansys Fluent*. Hence, an alternate workaround has been employed, which is the tabulated Equation of State (EOS).

The tabulated EOS method, involves creating lookup tables using the thermodynamic data from *REFPROP* (REFerence fluid PROPerties) database which is developed by NIST (National Institute of Standards and Technology). The properties for CO_2 in NIST has been formulated using the Span-Wagner Equation of State. The tabulated implementation of the Span–Wagner EOS demonstrated a significant computational advantage over direct functional calls, achieving a reduction in computational time by a factor of approximately 66.16 for an identical simulation case [32].

The tabulated EOS can be implemented in *Ansys Fluent* using the User Defined Real Gas Model (UDRGM), which involves using a C program to read the lookup tables. The UDRGM is compiled within *Ansys Fluent* to create the relevant libraries, after which the properties are loaded. During the runtime, UDRGM can interpolate the required properties using a relevant interpolation scheme, such as the bilinear interpolation. However, this method is limited to modelling the properties of a single phase only - either liquid or vapour.

3.7.1. User Defined Real Gas Model (UDRGM)

In the present study, the User Defined Real Gas Model (UDRGM) framework in *Ansys Fluent* has been employed to incorporate real-fluid thermodynamic behavior of vapour phase based on the tabulated equation of state.

The thermodynamic and transport properties of carbon dioxide in the lookup Table is tabulated over a discretized pressure–temperature domain and stored in structured text (.txt) files. The UDRGM was then implemented as a set of C functions to load and interpolate these property tables during runtime within *Ansys Fluent*.

The general structure of UDRGM comprises of,

- A **setup function** that is executed during simulation initialization. This function reads the property tables from disk and stores them in memory as a three-dimensional array, where the dimensions correspond to pressure points, temperature points and all the tabulated properties.
- A **bilinear interpolation** function that takes the local pressure, temperature and an integer index identifying the required property as the input and returns the interpolated value.
- A set of **property functions**, each corresponding to a specific thermodynamic or transport property. These functions act as wrappers that call the interpolation function with the appropriate property index.

The inputs to the UDRGM functions are restricted by *Ansys Fluent* to pressure, temperature and optionally the mass fractions of each species, which confirms the suitability of the tabulated EOS approach. This avoids the need to recalculate property values during each iteration and ensures consistent and efficient access to real-gas data.

For each point on the pressure–temperature grid, the following thermodynamic and transport properties were evaluated separately for both vapour and liquid regions,

- Density, ρ (kg·m^{-3})
- Specific enthalpy, h (J·kg^{-1})
- Specific entropy, s (J·kg^{-1}K^{-1})
- Specific heat capacity at constant pressure, C_p (J·kg^{-1}K^{-1})
- Speed of sound, a (m·s^{-1})
- Dynamic viscosity, μ (kg·m^{-1}s^{-1})
- Thermal conductivity, k (W·m^{-1}K^{-1})
- Molecular Weight, M (kg·kmol^{-1})
- Partial derivatives of density and enthalpy with respect to temperature and pressure,
  - $\left(\frac{\partial \rho}{\partial T}\right)_P$ (kg·m^{-3}K^{-1})
  - $\left(\frac{\partial \rho}{\partial P}\right)_T$ (kg·m^{-3}Pa^{-1})
  - $\left(\frac{\partial h}{\partial T}\right)_P$ (J·kg^{-1}K^{-1})
  - $\left(\frac{\partial h}{\partial P}\right)_T$ (J·kg^{-1}Pa^{-1})

To ensure stability during the simulation, especially in regions close to the saturation boundary or near the triple point, a clipping strategy was implemented. Inputs falling outside the defined table domain were set to the nearest valid bound along each axis independently. For example, if the temperature value exceeded the upper limit of the table, it was clipped to the maximum available temperature, and interpolation proceeded accordingly. This ensured smooth property variation and avoided divergence during the simulation process.

Overall, the UDRGM approach in combination with the tabulated equation of state, provided a robust and computationally efficient means to incorporate real-gas effects into the simulation. However, this method is limited to modeling the properties of a single phase only (vapour phase in this study). The source code of the UDRGM for handling the vapour phase properties is given in Appendix A.

To model the second phase in *Ansys Fluent*, two different approaches have been explored in the literature.

3.7.2. Multispecies UDRGM

The first method depends on using the Multispecies UDRGM functionality. This method is originally meant to be used for modelling multispecies systems rather than multiphase systems. However, Giacomelli et al. have successfully tweaked the functionality to include the properties of both phases under one multispecies UDRGM [75]. However, this method is much more complex to implement.

3.7.3. User Defined Function

The second method relies on using the User Defined Function (UDF) available in *Ansys Fluent*. *Ansys Fluent* allows the user to define the material properties using the `DEFINE_PROPERTY` routine and the specific heat and specific enthalpy properties using the `DEFINE_SPECIFIC_HEAT` routines. The lookup tables are read and stored using the `DEFINE_ON_DEMAND` routine, and the interpolation functions are carried out in the relevant routine meant for the respective property calculation. However, this method imposes a limitation on specific heat, restricting it to be a function of temperature only, rather than both temperature and pressure as in a complete UDRGM. Despite this restriction, the method has been shown to achieve a high level of accuracy in the solutions. The source code for the UDF to handle the liquid phase properties has been provided in the Appendix A.

3.7.4. Lookup Table Construction

The lookup tables for UDRGM and UDF has been generated in Python using the *ctREFPROP* wrapper, which is a convenient way to access the *REFPROP* data. The thermodynamic properties are tabulated as a function of two independent variables and stored in the memory for efficient access. *Ansys Fluent* allows for the use of pressure, temperature and density as the independent variables. In this study, pressure and temperature has been selected as the independent variables. A discretized pressure-temperature (P-T) grid has been constructed over the desired operating pressure & temperature range. The boundaries should be slightly selected in a relaxed manner as the solver would oscillate during the convergence process and during this time it should not go out of bounds which would affect the convergence of the solution. The grid spacing has to be chosen by keeping a right balance between accuracy and computational speed. A finer lookup table will help capture more accurately the gradients in thermodynamic properties, but increases the lookup Table size and the computation cost for table generation and reading. On the contrary, a coarser lookup table will give computational advantage while resulting in a loss of accuracy. Hence, a right balance has to be sought in the grid resolution and its selection will be explained in the following sub-section. The values of thermodynamic and transport properties that were listed in the sub-section 3.7.1 were obtained from *REFPROP* and constructed as lookup tables for both liquid and vapour phases. These properties are essential for accurately modeling the flow of supercritical carbon dioxide.

3.7.5. Handling Two-Phase Regions

To account for the different physical behaviors in the vapor and liquid phases, properties were computed separately in each region. For each point on the P–T grid:

- If the point lies in the single-phase **super-heated vapor** region, vapor properties were computed directly using *REFPROP*.
- If the point lies in the **sub-cooled liquid** region, liquid properties were computed accordingly.
- In regions near the saturation boundary or within metastable zones, *REFPROP* may return physically unstable or undefined values. To avoid this:
  - **Clipping** was applied by adding or subtracting a small pressure offset (± 1 kPa), ensuring that evaluations remain within the stable single-phase region.
  - For **vapor property evaluation near the saturation line**, the pressure was clipped slightly **below** the saturation or vapor spinodal pressure to remain in the superheated vapor region.
  - For **liquid property evaluation near the saturation line**, the pressure was clipped slightly **above** the saturation or liquid spinodal pressure to ensure liquid-phase validity.
- In the **supercritical region** (above both the critical temperature and pressure), no phase distinction is necessary and the properties were computed directly without clipping.

3.7.6. Non-uniform Lookup Table Generation

The thermodynamic properties of CO_2 exhibit relatively smooth variations across most of the pressure–temperature (P–T) domain. However, in the vicinity of the critical point, the properties undergo abrupt variations. This is particularly evident for properties such as the specific heat capacity at constant pressure (C_p), which exhibits pronounced peaks near the critical region. Figure 3.5 illustrates the variation of C_p over the P–T space, with a localized zone of sharp gradients indicated by red regions between approximately 295–310 K and 7.0–10.0 MPa.

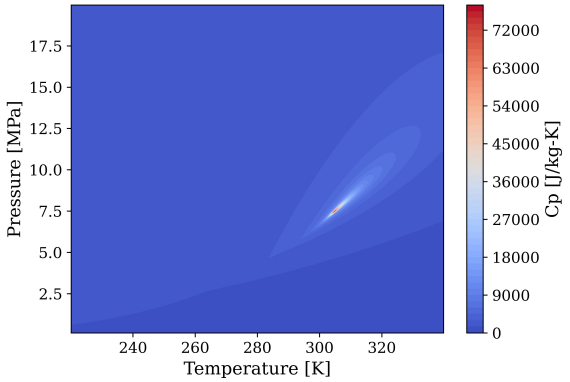

(a) Global distribution of specific heat capacity (C_p) over the P–T grid, showing gradual variation in most regions except in the vicinity of critical point.

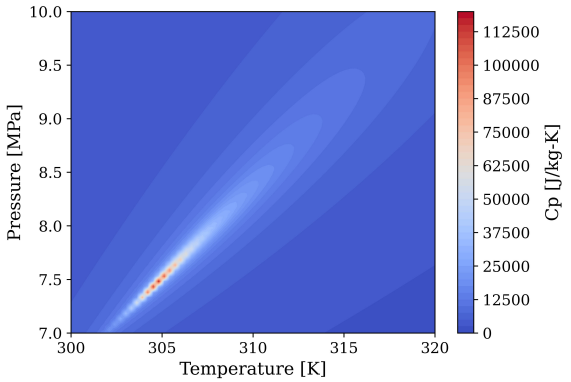

(b) Magnified view near the critical point, illustrating steep gradients in C_p across a narrow P–T band, highlighting the need for a finer P-T grid in this region.

Figure 3.5: Variation of specific heat capacity (C_p) across the P–T domain. Abrupt changes are confined to a localized zone (295–310 K, 7.0–10.0 MPa) near the critical point, highlighting the importance of finer grid resolution to capture these variations accurately.

In the previous work of Bob Fluttert [16], uniform grid of size 400×400 was employed to tabulate the thermodynamic properties. However, simulations using this grid in *Ansys Fluent* encountered numerical instabilities and convergence issues under supercritical inlet conditions. As a result, the inlet temperature was restricted to 300 K, confining the simulations to dense-phase liquid flows rather than the intended supercritical regime.

To overcome this limitation, finer lookup tables were experimented. Only with a lookup table of dimension 2400×2400 (resulting in a temperature resolution of 0.05 K and pressure resolution of 0.008 MPa) a stable single phase simulation was able to be performed in *Ansys Fluent* at a supercritical inlet temperature of 310.15 K. This highlights the importance of higher resolution lookup tables to solve the convergence issues near the critical point as encountered in the previous study.

However, adopting such finer grid lookup tables considerably increased the computational time and the memory requirements. To address this limitation, a non-uniform grid strategy was implemented in the present work. As evident from the Figure 3.5, abrupt variations are localized only in the vicinity of the critical point and the property variations were smoother in the other regions of the P–T grid. By leveraging this behaviour, the non-uniform grid was constructed maintaining a finer resolution within the critical region and a coarser resolution elsewhere.

In the present study, a **700×700 non-uniform grid** was adopted. The region from 300–320 K was resolved using a 400×400 grid to accurately capture the critical gradients, while the remainder of the domain employed a coarser 300×300 grid as shown in Figure 3.6. This configuration achieves a temperature resolution of 0.05 K and pressure resolution of 0.008 MPa near the critical point, comparable to a 2400×2400 uniform grid, while reducing table size by 3.5 times. This non-uniform lookup table effectively capture key thermodynamic features while significantly reducing memory requirements and computational costs. This particularly contributes to improved solver stability in simulations involving supercritical flow regime. The visual representation of the P-T domain has been presented in Figure 3.6 and a summary of the grid configurations and resolutions is provided in Table 3.1.

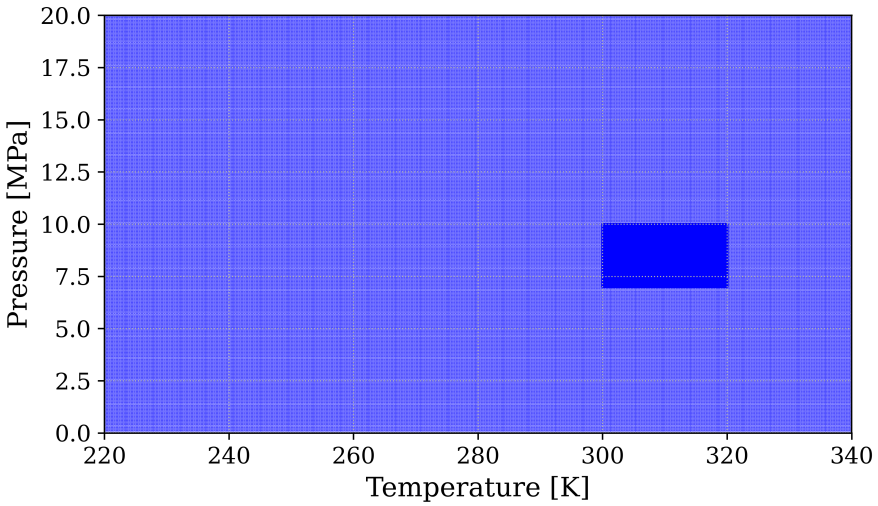

Figure 3.6: Non-uniform pressure–temperature grid for lookup table generation. The non-uniform grid ensures fine resolution in the critical region (300–320 K, 7.0–10.0 MPa) to resolve steep property gradients, while employing coarser spacing elsewhere to minimize memory usage and computational cost. The previously used uniform 400×400 grid lacked sufficient resolution near the critical point, which made supercritical simulations infeasible.

Table 3.1: Comparison of grid configurations and resolutions in the pressure–temperature domain. The 400×400 uniform grid, used in previous work, lacked sufficient resolution near the critical point and led to convergence issues under supercritical inlet conditions. A 2400×2400 uniform grid investigated in the present study, enabled stable solutions for supercritical conditions but at a significant computational cost. The final 700×700 non-uniform grid used in this work preserves fine resolution in the critical region (equivalent to the 2400×2400 grid) while minimizing memory requirements through coarser resolution elsewhere.

Grid Size	Grid Description	Temperature Resolution (K)	Pressure Resolution (MPa)
400 × 400	Uniform grid	0.30	0.049
2400 × 2400	Uniform grid	0.05	0.008
700 × 700	400×400 (critical region)	0.05	0.008
	300×300 (elsewhere)	0.33	0.056

Although the refined non-uniform lookup table facilitated convergence in single-phase simulations with supercritical inlet conditions, divergence was still encountered when the mass transfer model was activated in *Ansys Fluent*. This behaviour was attributed to the spurious peaks in the thermodynamic data. To address this issue, a smoothing algorithm was applied to minimise the sharp variations. Particularly, the smoothing algorithm was designed to preserve the underlying thermodynamic trends and inflection points while ensuring the smoothed data remains physically representative of CO_2 . The smoothing parameters were carefully chosen to avoid excessive smoothing that could distort the characteristic behaviour of CO_2. The methodology is detailed in the subsequent sections.

3.7.7. Smoothing Thermodynamic Properties Using the Savitzky–Golay Filter

The thermodynamic properties of CO_2 exhibit sharp variation in thermodynamic properties in the vicinity of the critical point, as discussed in the previous sub-section. The variation in this region is characterized by abrupt discontinuities and noise-like oscillations when the properties are visualized over a pressure-temperature (P-T) space as shown in Figures 3.7 and 3.8. In simulations with supercritical inlet conditions, the fluctuations cause a significant challenge of numerical instability and convergence issues. This is because when the expansion path from the supercritical to sub-critical state passes close to / through the critical point, where the variation in properties is more pronounced. When the solver encounters these abrupt variations in thermodynamic properties, it experiences difficulty in maintaining numerical stability, leading to residual blow-up and loss of convergence. The smoothing was applied sequentially in both temperature and pressure directions over the P–T grid.

To address this issue, a smoothing algorithm was applied to all the thermodynamic property tables before the generation of lookup Tables. Specifically, the Savitzky-Golay algorithm has been employed for this purpose [76]. This algorithm smooths the data points by fitting a low-degree polynomial to a moving window of the data using linear least squares. Compared to other filtering techniques, Savitzky-Golay smoothens the data by removing the high frequency noise, while preserving the local features such as maxima, minima and inflection points, making it suitable for thermodynamic data where such features are meaningful and must be preserved for accurate flow prediction.

The fundamental principle of the Savitzky-Golay filter is to locally approximate a set of data points within

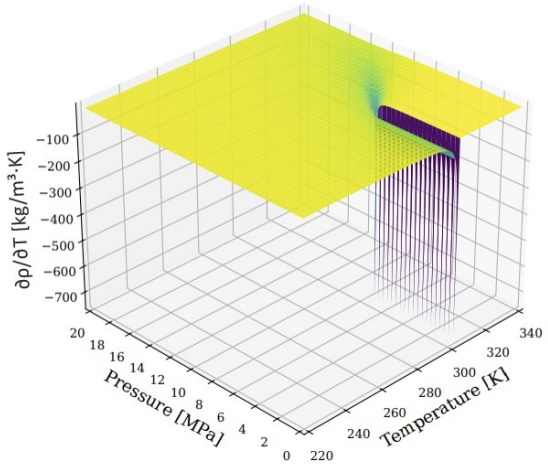

Figure 3.7: Raw contour plot of $(\partial\rho/\partial T)_P$ for CO_2 over the P–T domain. This derivative is loaded to *Ansys Fluent* via the UDRGM framework using the lookup table. It is required by the pressure-based coupled solver to linearize the equation of state and relate density changes to temperature variations during the iterative solution of the governing equations. Sharp gradients and spurious peaks that are evident near the critical point posed numerical stability challenges in the simulation.

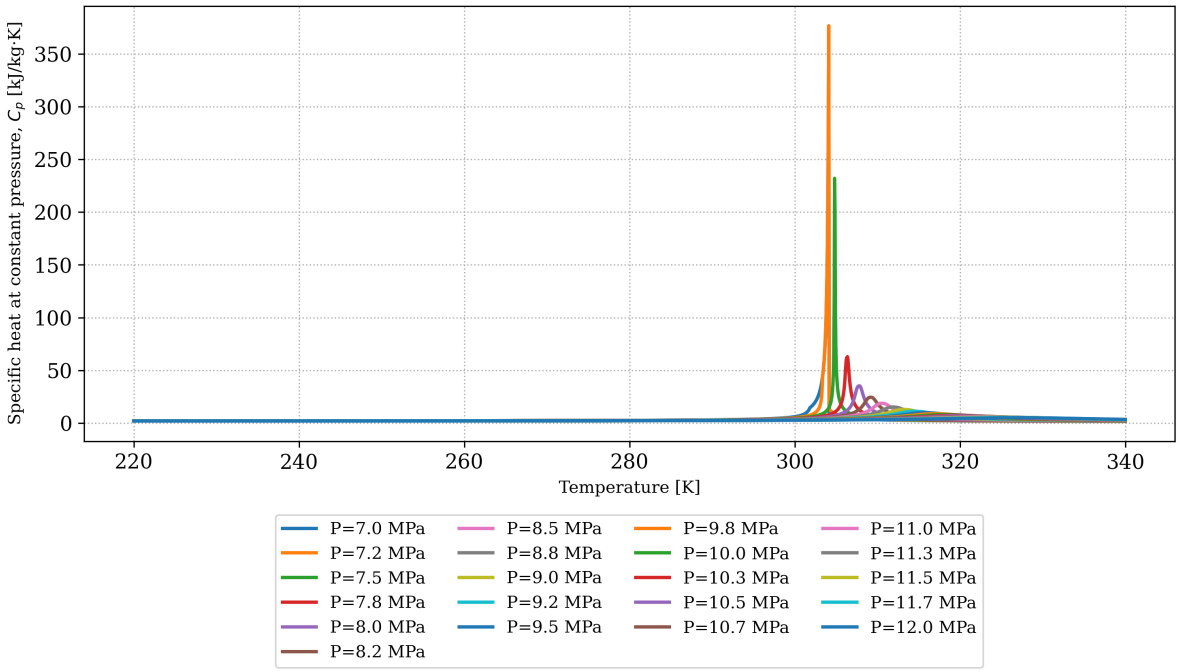

Figure 3.8: 2D plot of specific heat capacity at constant pressure (C_p) as a function of temperature for a wide range of pressures ranging from 7.0 MPa to 12.0 MPa between the temperatures 220 K to 340 K. A sharp increase in C_p is observed near the critical point of CO_2 (T = 304.13 K, P = 7.38 MPa), indicating strong thermodynamic fluctuations in this region. These steep gradients in C_p significantly influence energy transport, turbulent thermal conductivity and enthalpy estimation within the pressure-based coupled solver in *Ansys Fluent*, necessitating smoothing for numerical stability.

a moving window by fitting a polynomial of a specified degree. Consider a set of data points (x_i, y_i) where $i = 1$ to N. The objective is to fit a polynomial of degree p to these points.

The general form of such a polynomial of degree p is given by,

$$y = a_0 + a_1 x + a_2 x^2 + \cdots + a_p x^p$$

Now, consider a window of $2m + 1$ data points centered around x_k. The goal is to compute the coefficients $a_0, a_1, \ldots, a_p$ such that the polynomial provides the best fit to the points within the window. This is done by minimizing the sum of squared differences between the actual data values y_i and the polynomial values y_{ih}.

The objective function to be minimized is expressed as,

$$\text{Minimize} \quad \sum_{i=-m}^{m} \left(y_{k+i} - \sum_{j=0}^{p} a_j x_{k+i}^j \right)^2 \tag{3.47}$$

3.7.8. Implementation in the Present Work

In the present study, the Savitzky–Golay filter was applied to each thermodynamic property surface defined over the pressure–temperature domain. A comprehensive parameter sweep was conducted varying the window sizes and polynomial order.

Figure 3.9 illustrates the effect of varying window size (with a fixed polynomial order of 2) and varying polynomial orders (with a fixed window size of 21) on the smoothed surface of $(\partial\rho/\partial T)_P$ in the liquid region. For the window size variation (top row), a smaller window size (21) provided mild smoothing, effectively removing spurious peaks, while a larger window size (101) led to stronger smoothing but began to attenuate important physical gradients. Excessively large window sizes were found to overly suppress thermodynamic features. For the polynomial order variation (bottom row), increasing the polynomial order improved local fitting accuracy and better preserved physical trends, while lower polynomial orders resulted in excessive attenuation of peak amplitudes. A comprehensive parameter sweep was conducted varying the window sizes and polynomial order and its influence on the final simulation results from *Ansys Fluent* as well as the subsequent selection of optimal smoothing parameters is presented in 4.1.

The resulting smoothed property lookup tables were then stored and subsequently used as input to the User Defined Function (UDF) and User Defined Real Gas Model (UDRGM) in *Ansys Fluent*. While the smoothing process preserves the overall trend and topology of the property distribution, there is a mild attenuation in the peak value of the thermodynamic properties. Though this attenuation may lead to slight deviation in certain output variables, it was deemed acceptable, as it had only a minimal impact on the predicted results. On the other hand, this smoothing step was found to be indispensable for ensuring numerical stability, particularly in these simulations involving rapid expansion from supercritical to subcritical state. In such cases, where the expansion trajectory passes in close proximity / intersects the critical point, the smoothing step was critical in mitigating numerical instabilities and ensuring robust convergence. A discussion on the impact of this filtering on the simulation outcomes is presented in Chapter 4.

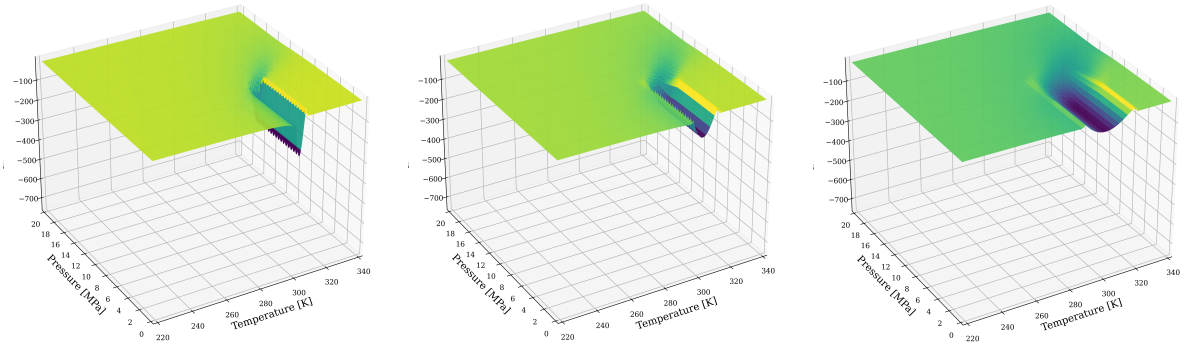

(a) Window size = 21, polynomial order = 2 **(b)** Window size = 51, polynomial order = 2 **(c)** Window size = 101, polynomial order = 2

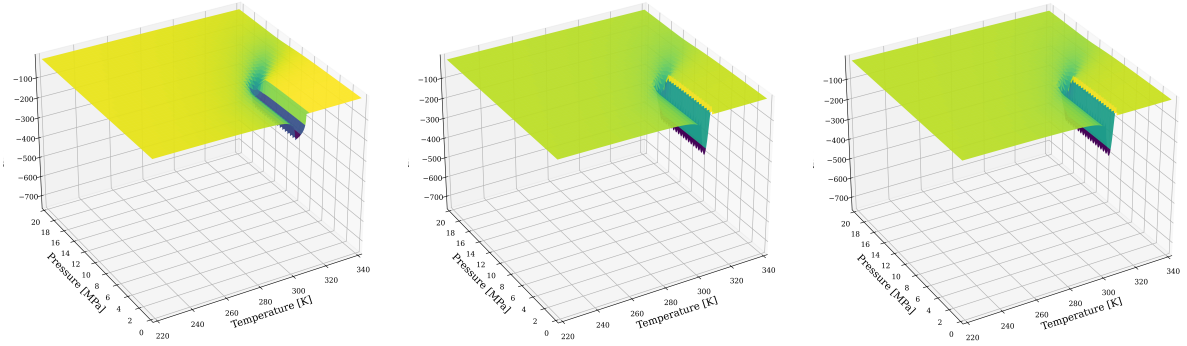

(d) Window size = 21, polynomial order = 1 **(e)** Window size = 21, polynomial order = 2 **(f)** Window size = 21, polynomial order = 3

Figure 3.9: Effect of Savitzky–Golay filter parameters on the smoothing of the raw $(\partial\rho/\partial T)_P$ contour in the liquid region, as shown in Figure 3.7. **Top row:** Variation of window size with polynomial order fixed at 2. Smaller window sizes provide mild smoothing, effectively removing spurious peaks, while larger window sizes result in stronger smoothing but can suppress important thermodynamic gradients. **Bottom row:** Variation of polynomial order with window size fixed at 21. Higher polynomial orders improve local fitting accuracy and preserve physical trends, whereas lower polynomial orders lead to excessive attenuation of peak amplitudes.

3.8. Geometry

As discussed previously in Chapter 2, there is currently no experimental data on the flow behaviour of supercritical carbon dioxide within control valves. However, a limited number of experimental studies have investigated the flow of supercritical carbon dioxide through converging-diverging nozzles. Since they offer a simple, yet meaningful scenario associated with rapid depressurisation of supercritical carbon dioxide, they have been chosen as the computational domain of interest in this study. The modelling strategies and the physical insights identified from this study may serve as basis for further extension to complex geometries such as control valves.

Among the experimental references reviewed in Section 2.6, the experiments conducted by Nakagawa et al. [45] have been selected for the simulation. Two kinds of experimental datasets are available from the author: (1) supersonic expansion of supercritical carbon dioxide with shockwaves and (2) supersonic outflow of carbon dioxide without shockwaves. The present study focuses on the former case due to complex flow features such as shockwaves and rapid phase transitions.

Two computational domains have been employed in this study: a quasi-one-dimensional (quasi-1D) planar domain and a two-dimensional (2D) planar domain. Although the actual nozzle geometry used in the experiments of Nakagawa is three-dimensional, the simplified models, while not capturing every geometric detail of a full 3D model, are expected to provide an accurate representation of the dominant flow physics and deliver results with sufficient accuracy for the objectives of this study. The cross section of the nozzle used in the experiments is rectangular. This enables the use of a planar domain, and the geometric symmetry about the horizontal axis enables further simplification by modelling only one half of the nozzle. A symmetry boundary condition was imposed along the horizontal axis; thus, the number of computational elements required has been halved.

The computational domain used for the simulations, along with the relevant dimensions, is illustrated in the Figure 3.10. A short straight section is included upstream of the converging section to ensure fully developed inlet flow conditions. Similarly, an extended straight section is added downstream of the diverging section, to ensure a smooth application of outlet boundary condition. The length of the downstream section is chosen sufficiently long to prevent numerical artifacts arising due to the specification of outlet static pressure. The inlet and outlet boundary conditions were imposed at the end of these straight sections.

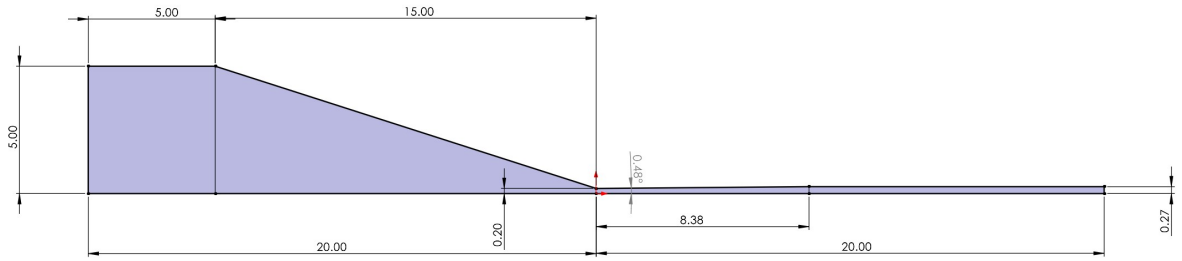

Figure 3.10: Computational domain used in the present simulation, based on the experimental setup of Nakagawa et al. for investigating the supercritical flow of carbon dioxide with shock waves [45].

3.9. Boundary Conditions

The computational domain requires the implementation of four primary boundary conditions: inlet, outlet, wall, and symmetry. The specification of each boundary condition is discussed below.

3.9.1. Inlet and Outlet Conditions

At the inlet of the upstream straight section, the total (stagnation) pressure and the total temperature have been specified to define the thermodynamic state of the flow. At the considered process conditions, carbon dioxide enters the domain in supercritical state, so the vapor fraction is explicitly set to zero to ensure single phase flow at the inlet.

At the outlet, the static pressure boundary condition was imposed at the exit of downstream straight section to facilitate for the proper flow development. In *Ansys Fluent*, the value of specified static pressure is used only when the flow is subsonic. If the flow becomes supersonic locally, then the specified outlet static pressure will no longer be used and the pressure will be extrapolated from the interior cells. [50].

3.9.2. Turbulence Specification

The flow regime for the considered process conditions is turbulent in nature. This requires specification of the turbulent quantities at the inlet and outlet. In this simulation, the turbulence parameters that has been chosen are hydraulic diameter and the turbulent intensity.

Hydraulic diameter is a characteristic length which is used to calculate the non-dimensional Reynolds Number. It is generally used for non-circular sections. It can be defined as the diameter of an equivalent circular tube that will have the same pressure loss as the subjected non-circular section. Hydraulic diameter is generally expressed as,

$$\text{Hydraulic diameter, } D_H = \frac{4A}{S} \tag{3.48}$$

where A is the cross-sectional area, and S is the wetted perimeter (circumferential length) of the cross-section.

The hydraulic diameter for a rectangular cross section is given by the following relation.

$$\text{Hydraulic diameter, } D_H = \frac{2wh}{w+h} \tag{3.49}$$

where
w = width of the nozzle (m),
h = height of the nozzle (m).

Turbulence intensity, denoted by I, is a non-dimensional measure of the strength of turbulence in a flow field. It is defined as the ratio of the root-mean-square (RMS) of the velocity fluctuations, u', to the mean flow velocity, u_{avg}:

$$I \equiv \frac{u'}{u_{\text{avg}}} \tag{3.50}$$

In case of fully-developed pipe or duct flows, an empirical correlation may be used to approximate the core turbulence intensity as a function of the Reynolds number based on the hydraulic diameter, Re_{D_H}. This correlation is given by,

$$I = 0.16 \left(\mathrm{Re}_{D_H}\right)^{-1/8} \tag{3.51}$$

This expression provides a practical estimate of turbulence intensity in the absence of detailed upstream flow measurements.

3.9.3. Wall and Symmetry Conditions

The upper edges of the nozzle was applied with wall boundary condition. For the quasi-1D simulation, a "Specified Shear" wall condition with zero shear stress is applied, effectively approximating inviscid flow behavior by neglecting wall friction. This assumption is justified because the boundary layer effects are negligible in quasi-1D flow approximations. In contrast, for the two-dimensional (2D) simulations, a no-slip wall boundary condition is employed to capture the viscous effects and boundary layer development along the solid walls. This distinction is essential for evaluating the influence of viscous shear on the pressure profile and the phase change.

The lower boundary of the nozzle has been assigned with symmetry boundary condition, taking advantage of the geometric symmetry. This enables simulation of only half of the physical domain. This significantly reduces the computational efforts without compromising the accuracy of the results.

3.9.4. Thermodynamic Setup

The thermodynamic conditions for the simulation were adopted from the experiments conducted by Nakagawa et al. [45] on the flow of supercritical CO_2 with shock waves in a converging-diverging nozzle. Among the various process conditions reported, the case corresponding to an inlet total pressure of 9 MPa and a total temperature of 310.15 K was selected. Under these conditions, carbon dioxide will be in a supercritical state at the inlet. Two different outlet static pressures were considered - 5.14 MPa & 4.82 MPa.

With these process conditions, the phase change was observed to initiate downstream of the throat from saturated liquid conditions. In the experimental setup, temperatures along the nozzle axis were measured using fine wire thermocouples mounted through the nozzle wall and extended into the core flow region along the axis. Owing to the minimal thermal mass, the fine wire thermocouples exhibit minimal flow disturbance and show good thermal response thereby measuring the static temperature of the flow with good accuracy. For the region between the inlet and the throat, the static pressure was estimated from the measured temperatures under the assumption of isentropic expansion. In contrast, for the region between the throat and the outlet, the static pressure was inferred from the measured temperatures assuming saturation conditions. This approach is justified because in the converging section of the throat, CO_2 remained in single phase and underwent quasi isentropic expansion, enabling pressure estimation using isentropic assumption. Downstream of the throat, phase change initiated and two-phase conditions prevailed with the local thermodynamic state closely tied to the saturation conditions, thus making this approach valid.

Table 3.2: Boundary condition specifications used in the simulations. The inlet and wall conditions are identical for both the quasi-1D and 2D geometries, while only the wall conditions differs. Two distinct back pressures were applied for simulations with both geometries.

Quantity [Unit]	Case 1	Case 2
Inlet		
Total Pressure [MPa]	9.00	9.00
Total Temperature [K]	310.15	310.15
Turbulence Intensity [%]	4	4
Hydraulic Diameter [m]	0.0018	0.0018
Outlet		
Static Pressure [MPa]	5.14	4.82
Turbulence Intensity [%]	3	3
Hydraulic Diameter [m]	0.0007	0.0007
Wall		
Quasi-1D Geometry	Zero shear wall	Zero shear wall
2D Geometry	No-slip wall	No-slip wall

3.10. Numerical Setup and Discretization Schemes

3.10.1. Solver Strategy

The pressure-based solver was employed for the present simulations in *Ansys Fluent*. While the density-based solver is generally suited for compressible flows, it is not compatible with the mixture multiphase model. As the present study involves multiphase flow of supercritical carbon dioxide with phase change phenomena, the pressure-based formulation was chosen.

The pressure-velocity coupling was handled using the *Coupled* algorithm. This approach simultaneously solves the momentum and pressure-based continuity equations, enhancing the robustness of the solution and accelerating convergence. This is particularly beneficial in multiphase simulations where strong coupling exists between pressure and velocity fields, such as in cavitating flows.

3.10.2. Spatial Discretization

The spatial discretization schemes used for the present simulations are listed below:

- **Gradient:** Least Squares Cell-Based method was used to compute gradients. This method is robust even for the regions with steep gradients in the property values, thereby ensuring stability of the simulation.
- **Pressure:** The PRESTO! (PREssure STaggering Option) scheme is the default scheme for mixture multiphase model [50]. PRESTO! computes face pressures using pressure values stored at staggered locations, enhancing accuracy and avoiding pressure-velocity decoupling.

- **Momentum, Energy, Turbulence Equations:** The First Order Upwind scheme was initially used for all quantities including density, momentum, energy, volume fraction, turbulent kinetic energy and specific dissipation rate. This was done to aid convergence during the initial stages of simulation. Once a stable solution was obtained, a second-order scheme was used in subsequent runs to improve solution accuracy as it is less dissipative.
- **Volume Fraction:** For the volume fraction equation, only the First Order Upwind scheme is available in *Ansys Fluent* when using the Mixture Model. This limitation is due to formulation of the volume fraction transport equation, which does not support higher-order discretization.

3.10.3. Temporal and Stabilization Settings

The simulations were carried out using steady-state assumptions. However, the Pseudo-Time method was helpful in achieving convergence in the simulations. The *High Order Term Relaxation* option was enabled to improve solution stability by damping high-frequency oscillations in the numerical solution. This is particularly useful in multiphase simulations, where sharp gradients can lead to numerical divergence in the early stages of the simulation.

3.10.4. Convergence and Stability Aids

To achieve initial convergence, especially in cases with strong phase interaction and sharp property gradients (such as in cavitation zones), the simulation was initialized with first-order schemes. This practice helps stabilize early iterations and avoids divergence. Once a preliminary solution was obtained, the solver settings were refined with second-order schemes to improve accuracy.

The residuals were monitored to ensure they settle a relatively constant value preferably below 10^{-3} and also mass balance check was done to ensure a difference of less than 0.01% between inlet and outlet mass flow rates.

A summary of the selected numerical schemes is presented in Table 3.3 and the sequential solution procedure has been outlined in the Figure 3.11.

Table 3.3: Summary of the solver and spatial discretization settings used in the simulations.

Setting	Selected Scheme
Solver Type	Pressure-Based
Pressure-Velocity Coupling	Coupled
Gradient	Least Squares Cell-Based
Pressure	PRESTO!
Momentum	First Order Upwind (initial), Second Order (refined)
Volume Fraction	First Order Upwind
Turbulence Quantities (k, ω)	First Order Upwind (initial), Second Order (refined)
Energy	First Order Upwind (initial), Second Order (refined)
Pseudo-Time Stepping	Global Time Step
High Order Term Relaxation	Enabled

3.11. Meshing Strategy

The meshing operation for this study was carried out using *Pointwise*. Two types of meshes were constructed namely, a quasi-one-dimensional (quasi-1D) mesh and a two-dimensional (2D) mesh. With the flow cross section of the converging-diverging nozzle used by Nakagawa et al. [39] being rectangular, only one half of the rectangle was considered for the computational mesh leveraging the geometric symmetry about the axis. A symmetry boundary condition was imposed along the horizontal axis to reduce the computational effort by half.

The quasi-1D mesh served as the baseline configuration for the simulation setup and mesh independence analysis. In the quasi-1D mesh, the computational grid was generated only in the axial direction, as the flow was assumed to vary primarily along the nozzle axis driven by the pressure difference between the inlet and outlet. The experimental reference by Nakagawa et al. [39] also presented the pressure distribution along the nozzle centreline only. Therefore, axial pressure development along the symmetry line was of primary interest and governed the meshing strategy. Subsequently, the dimensionality was extended to 2D by adapting the same axial mesh resolution as in the quasi-1D mesh and by adding elements in the wall-normal direction.

Due to the simplicity of the geometry, a structured quadrilateral mesh was used for discretizing the computational domain. This makes the mesh better aligned with the primary direction of flow and also minimises the skewness. This greatly helps in reducing the interpolation errors and the computational cost when compared to an unstructured mesh.

Since phase change phenomena were expected to be pronounced near the nozzle throat accompanied by huge gradients in flow parameters, a finer mesh was used in this region. The mesh element size was gradually increased away from the throat to reduce the unnecessary computational cost. Three different mesh configurations were generated by varying the axial resolution and are summarised in Table 3.4. The quasi-1D mesh (Mesh 2) has been illustrated in Figure 3.13.

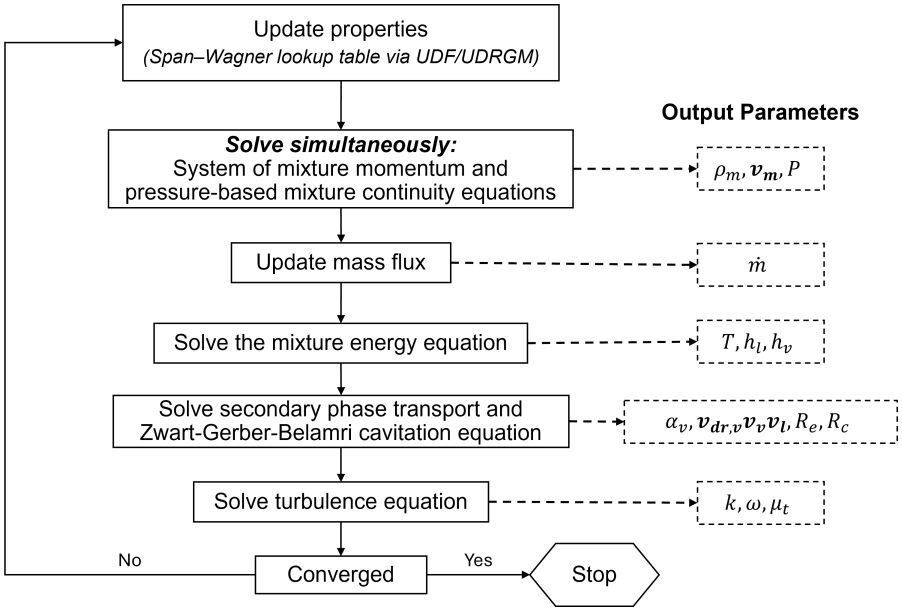

Figure 3.11: Sequential solution procedure for multiphase flow of supercritical CO_2 with cavitation using the pressure-based coupled solver in *Ansys Fluent*. Each step's primary output is shown.

Table 3.4: Axial mesh sizing used in the quasi-1D simulations along with the number of elements.

Mesh	Element size at the throat (mm)	Element size in other regions (mm)	No. of quadrilateral elements
Mesh 1	0.100	0.400	170
Mesh 2	0.050	0.200	342
Mesh 3	0.025	0.100	688

3.11.1. Mesh Independence Study

To study the influence of axial grid resolution on the solution accuracy, a mesh independence study was carried out using the quasi-1D mesh under single-phase flow conditions with the thermodynamic conditions corresponding to Case 1 of Table 3.2.

The pressure distribution along the nozzle axis for all three mesh configurations is shown in Figure 3.12. The mass flow rates obtained from the simulation with each mesh are summarised in the Table 3.5.

Table 3.5: Simulated mass flow rates obtained from single-phase quasi-1D simulations for different mesh resolutions. Mesh 1 and Mesh 2 produced identical mass flow rates, indicating mesh-independent behaviour. Mesh 3 showed a slight deviation due to numerical instabilities introduced by over-refinement near the throat.

Mesh	Simulated Mass Flow Rate (kg/s)
Mesh 1	0.0175
Mesh 2	0.0175
Mesh 3	0.0167

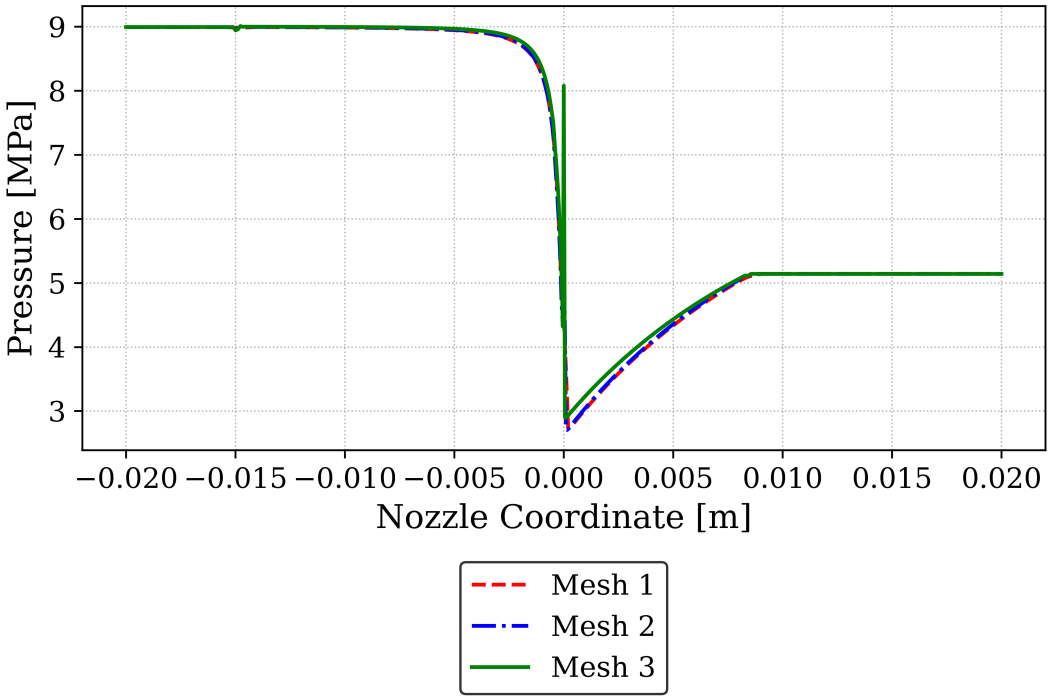

Figure 3.12: Axial pressure distribution for three different quasi-1D mesh resolutions for single-phase simulations. All the meshes show consistent behaviour in the converging section, while Mesh 3 exhibits minor pressure oscillations at the throat. Mesh 1 and Mesh 2 yield nearly indistinguishable pressure profiles, indicating mesh-independence.

It can be observed from Table 3.5 that Mesh 1 and Mesh 2 produced identical mass flow rates indicating mesh independence. However, Mesh 3 showed a slight reduction in the predicted mass flow rate. Additionally, Figure 3.12 shows that the pressure profiles are nearly indistinguishable along the nozzle symmetry axis for Mesh 1 and Mesh 2, while Mesh 3 exhibits pressure oscillations at the throat region. Moreover, in the subsequent two-phase simulations, Mesh 3 encountered divergence when the ZGB cavitation model was enabled. Similar concerns with finer mesh was reported by Stefano [36] in supercritical CO_2 flow simulations. The reason for the pressure wiggles is likely due to the reduction in numerical dissipation (artificial viscosity) with the finer mesh. The first order upwind formulation contains an implicit artificial viscosity term that scales with the local cell spacing Δx. When the axial spacing at the throat is reduced from 0.05 mm (Mesh 2) to 0.025 mm (Mesh 3), the numerical dissipation is halved. At the same time, the Rhie-Chow pressure velocity smoothening term which scales with Δx^2 is also reduced by a factor of 4. Without sufficient stabilizing effect from these terms, small-scale spurious pressure oscillations emerge in the form of wiggles near the regions with steep pressure gradient, such as the throat region.

Among Mesh 1 and 2, equivalent performance was observed in predicting the mass flow rate and pressure distribution. Out of these, Mesh 2 was considered for the subsequent simulations involving mass transfer. This is justified by its higher axial resolution near the throat where the phase transition occurs with sharp variation in flow parameters and in the diverging section where pseudo-shock-waves occur. The enhanced resolution makes Mesh 2 well suited for capturing these complex flow phenomena.

With the axial mesh resolution corresponding to Mesh 2, the mesh was scaled to the second dimension by discretizing the domain in the wall-normal direction. The near wall mesh was constructed with

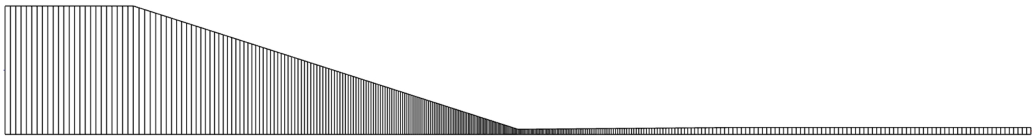

Figure 3.13: Structured quasi-1D mesh (Mesh 2) with discretization along the axial direction only. The mesh is refined near the throat to capture steep gradients, while a coarser distribution is used elsewhere to reduce computational cost.

inflation layers using a first cell height of 1×10^{-6} m. The height of subsequent elements was increased with a growth rate of 1.03 ensuring adequate resolution of the viscous sub-layer. The final 2D mesh consisted of 24,696 structured quadrilateral elements with a maximum area ratio 1.21 indicating smooth transitions and the absence of abrupt cell volume changes. The third dimension of the nozzle (depth into the plane) was specified directly in *Ansys Fluent* under the *Reference Values* panel and set to 0.001 m to match the experimental nozzle flow passage depth. This ensured that the integrated quantities such as mass flow rate were appropriately scaled.

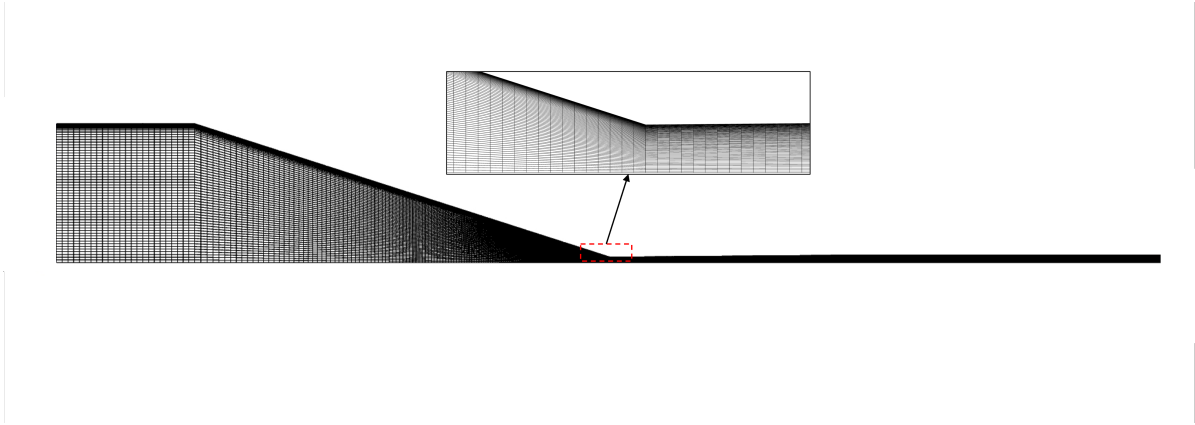

Figure 3.14: Structured 2D mesh with discretization in both axial and wall-normal directions. Inflation layers were applied near the wall to resolve the boundary layer, while axial refinement was maintained similar to the quasi-1D mesh.

The following chapter presents a comprehensive discussion of the simulation results obtained from the computational framework outlined in this chapter, along with the physical interpretation and implications.

4

Results & Discussion

The simulations conducted in this study were structured to replicate the flow behaviour of supercritical carbon dioxide through a converging-diverging nozzle under the thermodynamic conditions from the experimental work of Nakagawa et al. [45]. The inlet thermodynamic conditions were prescribed as a total pressure of 9 MPa and a total temperature of 310.15 K, ensuring that carbon dioxide enters the nozzle in a supercritical state rather than the dense liquid phase used in the previous work of Fluttert et al. [16]. Two different outlet static pressures were used for the simulation namely, 5.14 MPa (Case 1) and 4.82 MPa (Case 2).

All the simulations incorporate the property lookup tables from Span-Wagner Equation of State, smoothed using a Savitzky-Golay filter to suppress the spurious oscillations while maintaining the physical trends. The simulation framework was enhanced by the inclusion of slip velocity between phases, rather than adopting a Homogeneous Equilibrium Model (HEM) formulation, as justified in the Section 4.8. Turbulent effects were incorporated in the ZGB cavitation model to better capture the phase change dynamics. This chapter presents the simulation strategies and key findings obtained from both quasi-one-dimensional and two-dimensional geometries for the two back pressure cases. Surface tension effects were neglected in the simulation as its impact on the results were insignificant and is discussed in detail in Section 4.13.

4.1. Selection of Smoothing Parameters for Savitzky-Golay Filter

As outlined in Section 3.7.7, the performance of Savitzky-Golay filter in processing the thermodynamic data depends on the selection of two parameters - the window size and polynomial order. These parameters control the balance between the suppression of spurious peaks and the preservation of physically meaningful inflection points and gradients in the thermodynamic data.

The window size represents the number of data points used for the smoothing operation. It must be an odd integer, and its value must exceed the value of the polynomial order. A larger window size results in stronger smoothing by averaging over a broader range of data, thereby attenuating the spurious peaks

Table 4.1: Boundary conditions used for the simulation in *Ansys Fluent* to study the effect of smoothing parameters.

Parameter	Value
Inlet total pressure	9.00 MPa
Inlet total temperature	310.15 K
Outlet static pressure	5.14 MPa
Wall	Specified Shear (Zero Shear)

more effectively. However, this can excessively flatten the gradients which may eliminate meaningful inflection points. On the other hand, a very small window size may not cause effective smoothing and the abrupt transitions may still be present in the thermodynamic data, potentially leading to the divergence of the solver during the solution process.

The polynomial order governs the complexity of the curve fitted within the window. A low-order polynomial fits a very smooth curve, but this results in underfitting in the areas of sharp transitions. Whereas higher-order polynomials capture the curvature in data and local inflection points and may still retain some spurious peaks particularly when coupled with smaller window sizes.

To systematically determine optimal smoothing parameters, a comprehensive parameter sweep was conducted by varying both window size and polynomial order. Polynomial orders of 2 and 3 were tested in combination with a wide spectrum of window sizes ranging from 101, 51, 21, and 11. The smoothed lookup tables generated from these configurations were incorporated into the UDF and UDRGM in *Ansys Fluent* to assess their influence on convergence behaviour and simulation results. The simulation was carried out on the quasi-1D geometry with the boundary conditions listed in Table 4.1.

It was observed that,

- By using the smoothed lookup table from a window size of 11, the simulations diverged early in the solution process when the interphase mass transfer was enabled. This is attributed to insufficient smoothing of sharp peaks in the raw data, which introduced numerical instability.
- The lookup tables generated using the window sizes of 21, 51 and 101 all led to stable simulations. Among these, a window size of 21 provided a favourable trade-off as it was sufficiently small to preserve inflection points and local curvature, yet it was able to smooth the abrupt peaks that could affect the solver stability.
- For a fixed window size, increasing the polynomial order from 2 to 3 showed negligible differences in both the simulated mass flow rate and the pressure profiles. This is evident from the simulation results from *Ansys Fluent* in both Table 4.2 and Figure 4.1. Hence, higher polynomial orders were not explored further, as the results exhibited negligible sensitivity beyond order 2 and using higher orders could risk overfitting the thermodynamic data, thereby distorting the underlying physical trends.

Table 4.2: Influence of window size and polynomial order on the simulated mass flow rate. Lookup tables smoothed with smaller window sizes gave better prediction of mass flow rates due to less attenuation of the properties. Change in polynomial order did not show any effect for a given window size.

Window Size	Polynomial Order	Simulated Mass Flow Rate (kg/s)	Experimental Mass Flow Rate (kg/s)
101	2	0.0176	0.0223
101	3	0.0176	
51	2	0.0180	
51	3	0.0180	
21	2	0.0183	
21	3	0.0183	
11	2	Simulation diverged	
11	3	Simulation diverged	

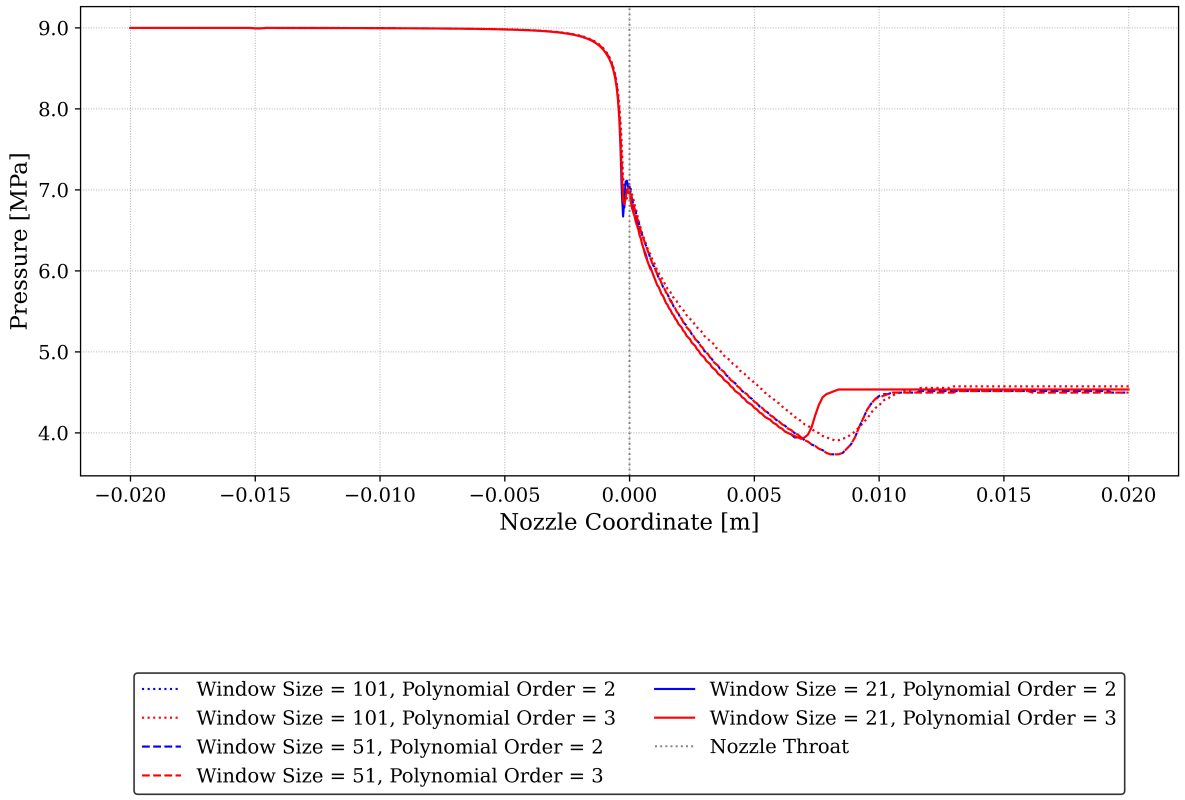

Figure 4.1: Overlay of pressure profiles along the nozzle axis in quasi-1D simulation for different combinations of window size and polynomial order used in the Savitzky–Golay filter. For each window size, polynomial orders of 2 and 3 produce nearly identical results. However, different window sizes yield visibly distinct pressure curves, particularly in the pseudo-shock region.

Based on the analysis, a window size of 21 and a polynomial order of 3 were selected for the final simulations. This configuration offered the smallest window that ensured numerical stability while effectively preserving key thermodynamic inflection points. Among the stable configurations tested, it

also produced the highest predicted mass flow rate, which most closely approached the experimental value as shown in Table 4.2. The Normalised Root Mean Square Deviation (NRMSD) value was calculated for smoothed data corresponding to each combination of window size and polynomial order. A low value of NRMSD indicates a close match between the smoothed and original (raw) *REFPROP* data. The NRMSD values are tabulated in Appendix B. For the widow size of 21 and polynomial order of 3, the NRMSD percentage value for all the smoothed thermophysical properties was less than 1.5 %, with most properties exhibiting deviations less than 1.0 %. Though the smallest window size (11) yielded the lowest NRMSD values, it was excluded from consideration due to numerical instabilities encountered by the solver. A detailed comparison between the simulated and experimental pressure distributions, along with the corresponding mass flow rate and the underlying physical interpretations, is presented in the subsequent sections.

4.2. Overview of Simulation Strategy

As discussed in previous chapters, the flow of supercritical carbon dioxide through a converging–diverging nozzle involves rapid depressurisation accompanied by phase transition from a supercritical fluid to a two-phase mixture comprising vapour and liquid phases. The expansion trajectory in the simulation closely follows the critical point where steep gradients are observed in the thermodynamic and transport properties of carbon dioxide. These abrupt property variations pose significant numerical challenges, particularly in achieving convergence during CFD simulations.

To mitigate this challenge, the thermodynamic data were pre-processed using the Savitzky-Golay filter to remove oscillations and suppress spurious spikes as discussed in the Section 3.7.7. In addition to this pre-processing, certain simulation strategies were implemented to improve the numerical robustness and guide the solver towards convergence.

The initial simulation was performed using a single-phase assumption with mass transfer mechanisms disabled. The simulation was also initiated from a sub-critical inlet temperature of around 300.15 K to avoid a cross-over with the critical point. This facilitated numerical stability and enabled the solver to converge to a physically consistent flow field. The resulting single-phase solutions served as a stable initial condition for the subsequent two-phase simulations.

Once the numerical stability was achieved with the single-phase simulation, the Zwart-Gerber-Belamri (ZGB) cavitation model was activated to model the phase transition from liquid to vapour and vice versa. However, initial runs using the default model coefficients (F_{vap} = 50, F_{cond} = 0.01) led to unphysically rapid condensation and oscillation in the pressure profile downstream of the throat. So, the condensation coefficient was reduced to obtain a result close to the physical process as shown in Figure 4.2. Following this adjustment, the inlet temperature value was increased to the supercritical temperature of 310.15 K in accordance with the experiments of Nakagawa et al. [45].

Subsequently, the evaporation (F_{vap}) and condensation coefficients (F_{cond}) were iteratively tuned to improve the agreement with the experimental pressure data and to accurately capture the dynamics of supercritical CO_2 expansion which will be discussed in the following sections.

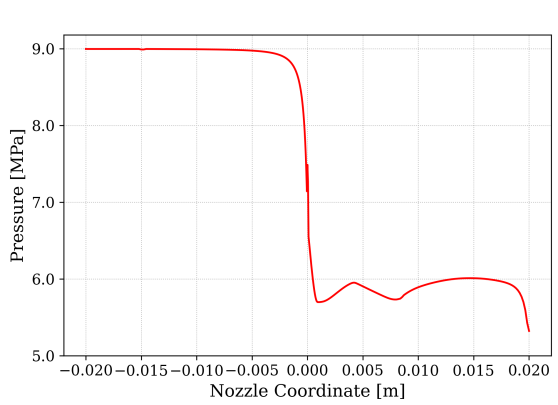

(a) Static pressure distribution at 300.15 K using default cavitation coefficients. Unphysical pressure recovery occurs with oscillations due to rapid phase change.

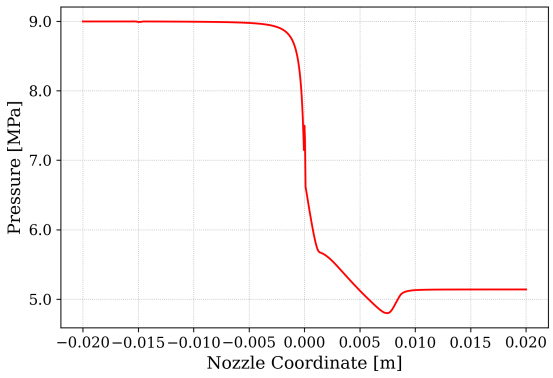

(b) Improved pressure prediction at 310.15 K aft er tuning the value of condensation coefficient, F_{cond} to the order of $F_{cond} = 1 \times 10^{-8}$. Post-processed profile becomes physically representative of the flow in converging diverging nozzle with pseudo-shock waves.

Figure 4.2: Comparison of pressure profiles before and after tuning cavitation model coefficients.

4.3. Pressure Calculation and Post-Processing Methodology

In the experimental study conducted by Nakagawa et al. [45], the pressure distribution across the converging–diverging nozzle was only partially obtained through direct pressure measurements. Pressure probes were used to measure static pressure at the inlet and outlet, while the intermediate pressure distribution along the nozzle was inferred using alternative methods. With the inlet total pressure known, the pressure in the converging section of the nozzle was estimated based on isentropic assumptions. The conditions at the throat was expected to be in saturation conditions. In the diverging section of the nozzle, the pressure values were not directly measured. Instead, the pressure values were calculated from the static temperatures measured using thermocouples. The temperature values were mapped to the corresponding saturated pressures ($P_{sat}(T)$), assuming saturation conditions. These mapped pressure values were only published in the experimental reference. The actual measured temperature profile was not explicitly published, which introduces uncertainty in interpreting and validating the simulation results.

To align with the experimental methodology and enable a meaningful comparison, a revised post-processing strategy was adopted in this study. This approach differs from the conventional practice of directly comparing the static pressure output from the simulation with the experimental pressure curve. Here, the static pressure values were post-processed from the static temperature values computed by *Ansys Fluent*, assuming saturation conditions in the diverging section.

The post-processing approach for pressure can be summarised as follows:

- **Upstream of the throat:** The flow remains in single-phase, supercritical state. Hence, the static pressure values directly obtained from *Ansys Fluent* was used.
- **Downstream of the throat:** In the region where phase transition occurs, static pressure values were computed by mapping the simulated static temperature to the corresponding saturation pressure using the saturation LookUp Tables from Span-Wagner EOS. This assumes local thermodynamic equilibrium in the diverging section, in consistent with the assumptions made in the experimental reference.

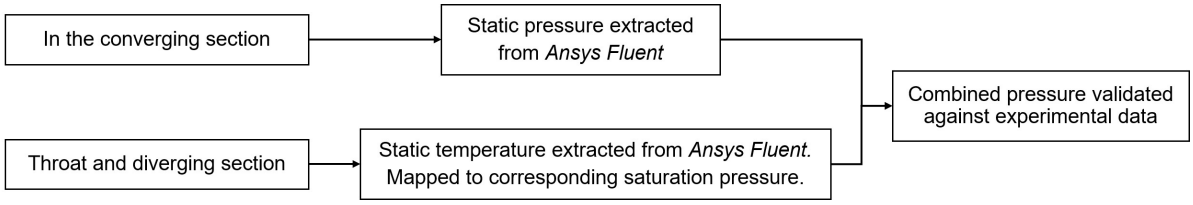

Figure 4.3: Post-processing methodology for pressure reconstruction to align with the experimental approach

This refined post-processing method was found to improve the agreement between the simulated and experimental pressure profile in the regions with two-phase flows. The methodology is illustrated in Figure 4.3.

4.4. Axial Pressure Distribution and Validation With Experiments

The pressure distribution along the axis of symmetry for the quasi-1D and 2D simulations is presented in Figure 4.4. The pressure data were post-processed in accordance with the methodology outlined in Section 4.2. All the pressure plots presented in this section are post-processed pressure plots as per the Figure 4.3. The post-processed pressure plots have been compared with the experimental pressure plots of Nakagawa et al. [45].

4.4.1. Effect of ZGB Cavitation Model Coefficients

Based on the sensitivity analysis and iterative calibration of the cavitation mass transfer coefficients in the ZGB cavitation model, suitable combination of evaporation and condensation coefficients were identified for each back pressure and geometry that yielded the best agreement between the simulated and experimental pressure profiles. The optimal combination differed between the Quasi-1D and 2D configurations due to variations in geometry, boundary conditions and flow dimensionality. The values are tabulated below.

Table 4.3: Optimal cavitation model coefficients used in the simulations for both back pressure cases. The empirical coefficients F_{vap} and F_{cond} were calibrated to achieve best possible agreement with experimental data.

Geometry	**Evaporation Coefficient** (F_{vap})	**Condensation Coefficient** (F_{cond})
Case 1: Back Pressure = 5.14 MPa		
Quasi-1D Simulation	2.0	1×10^{-10}
2D Simulation	2.0	1×10^{-8}
Case 2: Back Pressure = 4.82 MPa		
Quasi-1D Simulation	3.0	1×10^{-9}
2D Simulation	3.0	1×10^{-7}

Optimal evaporation coefficient (F_{vap}): In both back pressure cases, the evaporation coefficient (F_{vap}) required significant reduction from the default value of 50 to a value of 2 for Case 1 and a value of 3 for Case 2. This reduction was done to slow down the rate of vapour generation in the simulation,

which otherwise tends to predict an unrealistically rapid onset of phase change upon reaching saturation conditions.

Physically, this change compensates for the absence of metastable behaviour in the ZGB cavitation model. In reality, the phase transition from supercritical to vapour state is not instantaneous but proceeds via a non-equilibrium process influenced by nucleation energy barriers. The fluid does not rapidly undergo phase transition but remains in a single phase state until the Widom line. The default high value of F_{vap} implicitly causes rapid vapour formation once saturation is reached similar to equilibrium phase transition as described in the Section 2.4.

By reducing F_{vap}, the simulations effectively impose a slower phase transition rate. This is essential to replicate the pressure drop and non-equilibrium phase change behaviour as observed experimentally.

Ideal Coefficient Combination for Quasi-1D Configuration: The optimal combination of cavitation coefficients that produced the best possible match with the experimental pressure distribution, differed based on the back pressure for the same quasi-1D geometry, as shown in Table 4.3 and illustrated in Figures 4.4a and 4.4c. At the higher back pressure of 5.14 MPa (Case 1), the best agreement with experimental data was achieved using $F_{\text{vap}} = 2.0$ and a strongly suppressed condensation coefficient of $F_{\text{cond}} = 1 \times 10^{-10}$. At the lower back pressure of 4.82 MPa (Case 2), the evaporation coefficient was increased to $F_{\text{vap}} = 3.0$ while the condensation coefficient was relaxed to $F_{\text{cond}} = 1 \times 10^{-9}$. Since the quasi-1D geometries employed a zero shear boundary condition, it nearly approximated an inviscid flow behaviour. Additionally, due to the presence of only one mesh element in the transverse direction, there is no momentum transfer happening at the wall and the flow evolves purely in the streamwise direction. Hence, an aggressive suppression of the condensation coefficient was found to be necessary to prevent a rapid vapour collapse (cavitation) in the absence of shear and wall boundary effects. Without condensation being heavily damped, a rapid vapour collapse happened in the simulation, in contrary to the experiment.

Comparing the two back pressure cases, Case 2 required comparatively high values of F_{vap} and F_{cond} to match the experimental results. Because, the reduced back pressure in Case 2 causes a stronger expansion and the flows enters the two-phase regime much earlier. To replicate the rapid onset of phase transition, the evaporation coefficient (F_{vap}) had to be increased from a value of 2 to 3. Similarly, a higher condensation coefficient was required to model the faster vapour collapse and achieve the experimentally observed pressure recovery in the diverging section.

Ideal Coefficient Combination for Two-Dimensional Configuration: For Case 1 (back pressure = 5.14 MPa), the optimal coefficients that produced the best possible match with the experiments were $F_{\text{vap}} = 2.0$ and $F_{\text{cond}} = 1 \times 10^{-8}$. Whereas for Case 2 (back pressure = 4.82 MPa), the evaporation coefficient was increased to $F_{\text{vap}} = 3.0$, and the condensation coefficient was relaxed to $F_{\text{cond}} = 1 \times 10^{-7}$, with the values being slightly higher than that of Case 1, as observed in the quasi-1D geometry. The corresponding axial pressure distribution is illustrated in Figures 4.4b and 4.4d.

In 2D simulations, the inclusion of no-slip boundary condition and well-resolved inflation layer introduced viscous shear and boundary layer development. This viscous dissipation inherently slowed down the vapour collapse, resulting in a better match at a less suppressed condensation coefficient than the quasi-1D case. The pressure recovery also aligned well with the experimentally reported pseudo-shock

wave, where the flow deceleration occurs over a wider region than as an abrupt discontinuity. Thus, the 2D simulation gave a more physically realistic representation of the flow dynamics.

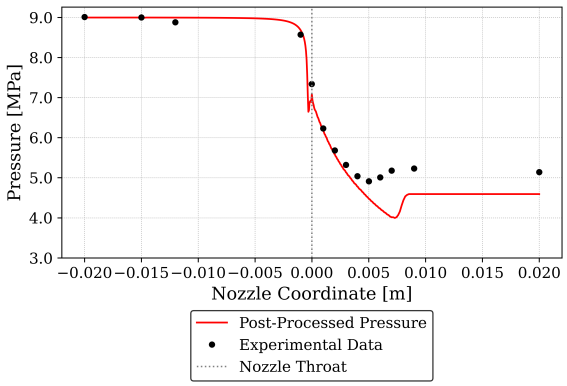

(a) Case 1 (Back pressure = 5.14 MPa): Quasi-1D simulation. $F_{\text{vap}} = 2.0$, $F_{\text{cond}} = 1 \times 10^{-10}$.

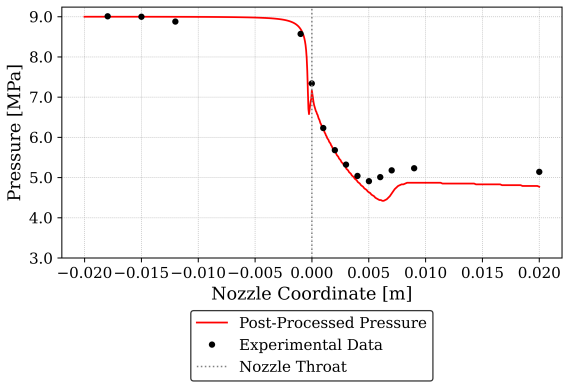

(b) Case 1 (Back pressure = 5.14 MPa): 2D simulation. $F_{\text{vap}} = 2.0$, $F_{\text{cond}} = 1 \times 10^{-8}$.

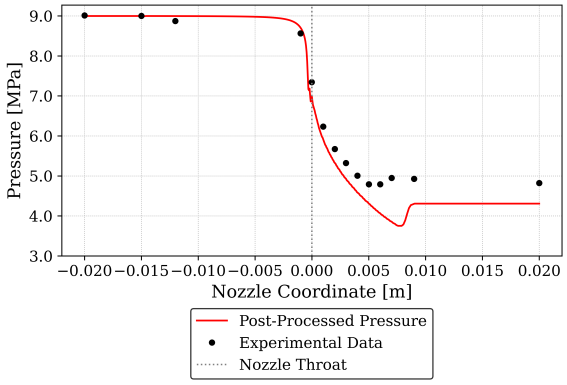

(c) Case 2 (Back pressure = 4.82 MPa): Quasi-1D simulation. $F_{\text{vap}} = 3.0$, $F_{\text{cond}} = 1 \times 10^{-9}$.

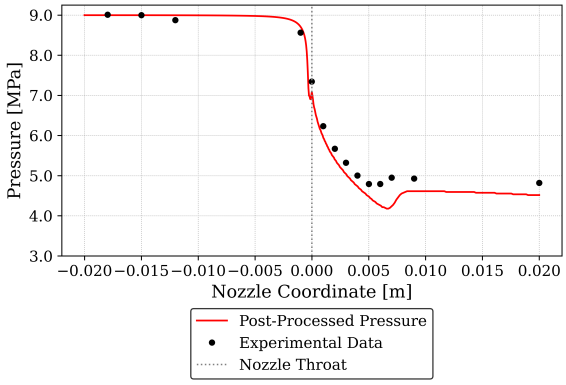

(d) Case 2 (Back pressure = 4.82 MPa): 2D simulation. $F_{\text{vap}} = 3.0$, $F_{\text{cond}} = 1 \times 10^{-7}$.

Figure 4.4: Comparison of axial pressure distributions for quasi-1D and 2D simulations at two back pressure conditions. The pressure profiles were post-processed using static temperature and saturation mapping to replicate the methodology of Nakagawa et al. [45] **Top row:** Case 1 (back pressure = 5.14 MPa). **Bottom row:** Case 2 (back pressure = 4.82 MPa). Experimental data are overlaid as black circular markers for validation. The quasi-1D simulations exhibit stronger depressurisation and quick recovery due to inviscid flow assumptions, requiring aggressive suppression of condensation (F_{cond}) to prevent rapid vapour collapse. In contrast, the 2D simulations incorporate viscous shear effects and boundary layer development, moderating vapour collapse and yielding smoother pressure recovery. At the lower back pressure (Case 2), both F_{vap} and F_{cond} were increased to account for the intensified expansion and accelerated phase transition kinetics.

4.4.2. Comparison of Axial Pressure Distribution in Quasi-1D and 2D simulation

The overall trend in all the geometries and boundary conditions as illustrated in Figure 4.4 exhibit a rapid pressure drop initiating at the throat and continuing in the downstream section, followed by a gradual rise in static pressure. This is a characteristic of choked flow with pseudo-shock wave phenomena. However, distinct differences exist in the pressure profile between the two geometries:

- In the **quasi-1D geometry** (Figures 4.4a and 4.4c), the pressure minimum reaches a much lower value than 2D geometry (approximately 3.99 MPa for Case 1 and 3.75 MPa for Case 2) and the recovery is also quick. This low-pressure reflects the absence of shear and wall effects. The

absence of transverse momentum diffusion resulted in a nearly ideal expansion in the streamwise direction causing the fluid to depressurize more rapidly.

- In the **2D geometry** (Figures 4.4b and 4.4d), the magnitude of the pressure drop is attenuated relative to the quasi-1D case and the pressure recovery is more gradual than in the quasi-1D case. The implementation of no-slip boundary conditions and the boundary layer development leads to viscous shear forces in the flow. The shear effects slow down the fluid near the walls reducing the depressurisation and acceleration of the flow in streamwise direction. This resulted in a pressure profile with better agreement to the experimental profile.

4.4.3. Comparison with Experimental Data

The experimental data from Nakagawa et al. [45] are overlaid as black circular markers in both pressure plots (Figure 4.4) enabling a direct comparison between simulation and measurement.

- The **quasi-1D simulation** (Figures 4.4a and 4.4c), captures the general expansion behaviour with the overall trends. However, it deviates in accurately predicting the magnitude of the pressure drop and the subsequent recovery rate. This is expected given the lack of wall effects and dimensional limitations.
- The **2D simulation** (Figures 4.4b and 4.4d), closely matches the experimental pressure profile. Both the onset and rate of the pressure drop align well with the experimental trend and the downstream recovery lies within the expected range. This consistency validates the physical modelling approach, such as the inclusion of no slip walls, well resolved boundary layers and optimal combination of cavitation coefficients to replicate the metastable behaviour.

In summary, while the quasi-1D model offers computational efficiency and captures the first-order behaviour of supercritical CO_2 expansion, the 2D simulation provides a more realistic pressure profile that better aligns with experimental observations. The use of post-processed pressure mapped from the static temperature further improves the quality of the comparison, especially in the downstream region where direct experimental pressure measurements are not reported in the experimental reference.

4.5. Mass Flow Rate Analysis

Mass flow rate serves as a critical validation parameter in compressible two-phase nozzle flows, as it reflects the combined influence of thermodynamic state, choking conditions and phase transition behaviour. Table 4.4 summarizes the predicted mass flow rates from the quasi-1D and 2D simulations compared with the experimental value reported by Nakagawa et al. [45].

Both the quasi-1D and 2D simulations underpredict the experimental mass flow rate for the two back pressure cases. For Case 1 (back pressure = 5.14 MPa), the quasi-1D and 2D geometries underpredicted the experimental mass flow rate by 15.34 % and 16.27 %, respectively. In Case 2 (back pressure = 4.82 MPa), there was slightly higher deviations of 17.55 % and 18.22 % for the quasi-1D and 2D geometries. The slightly larger underprediction in Case 2 is attributed to the stronger expansion and earlier onset of phase transition at the lower back pressure.

In general, the underprediction is likely due to the combination of modelling assumptions and numerical simplifications as outlined below:

Table 4.4: Comparison of simulated and experimental mass flow rates for both back pressure cases. The simulations underpredict the measured values due to modelling simplifications, including early phase transition onset and filtered thermodynamic data, both of which reduce density and delay choking onset.

Case	Mass Flow Rate [kg/s]	Percentage Deviation from Experiment
Case 1: Back Pressure = 5.14 MPa		
Experiment (Nakagawa et al. [45])	0.0223	–
Quasi-1D Simulation	0.0189	-15.34%
2D Simulation	0.0187	-16.27%
Case 2: Back Pressure = 4.82 MPa		
Experiment (Nakagawa et al. [45])	0.0222	–
Quasi-1D Simulation	0.0183	-17.55%
2D Simulation	0.0182	-18.22%

Absence of Metastable Flow Treatment: The Zwart–Gerber–Belamri cavitation model assumes equilibrium phase transition and does not account for metastable liquid behaviour. In reality, during flows with rapid expansions such as in converging-diverging nozzle, the onset of vapour formation gets delayed. This allows the fluid to remain in single phase metastable state for an extended distance in the downstream of throat. In this state, the fluid density remains higher than that of vapour, aiding higher mass flow rate. In contrast, the current simulation triggers vapour formation prematurely, resulting in lower local density and consequently underpredicting mass flow rate.

Smoothed Equation of State Lookup Table: Although the real-gas thermodynamic properties were incorporated via lookup tables generated using Span-Wagner EOS, the data were smoothed using a Savitzky-Golay filter to ensure numerical stability. This filtering attenuates the sharp gradients and local extrema of thermodynamic properties. This, in turn, affects the prediction of choking conditions, leading to an underestimation of mass flow rate. Nevertheless, the application of smoothing was found to be indispensable for achieving convergence in the supercritical CO_2 simulations presented in this study. To minimise its impact on the solution accuracy, the smoothing was ensured to be kept as minimum as possible (as elaborated in Section 4.1) to preserve critical thermodynamic gradients while maintaining solver stability.

4.6. Velocity Distribution Along Nozzle Axis

Figure 4.5 presents the velocity magnitude along the nozzle axis for both quasi-1D and 2D simulations at two back pressure conditions. In all cases, the velocity increases smoothly through the converging section and exhibits a sharp rise near the throat. This is followed by further acceleration in the diverging section.

The noticeable drop in velocity occurring in the diverging section indicates the presence of a shock wave. However, the deceleration is not abrupt but occurs over a finite spatial region, indicating the presence

of a pseudo-shock structure rather than a sharp normal shock wave (equilibrium shock wave). This behaviour is consistent with the pressure distribution observed in the experiments of Nakagawa et al.[45], where the shock transition in two-phase CO_2 flow appeared as a weak and spatially distributed shock. Such pseudo-shock waves are characteristic of two-phase flows where the rapid flashing process leads to slip (velocity non-equilibrium) between the liquid and vapour phases. This causes the smearing of the shock wave over a broader region instead of forming a localised discontinuity.

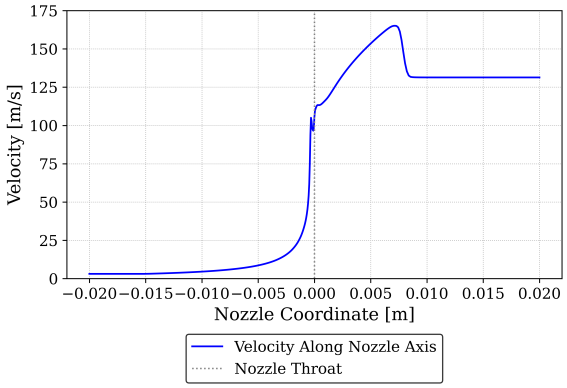

(a) Case 1 (Back pressure = 5.14 MPa): Quasi-1D simulation.

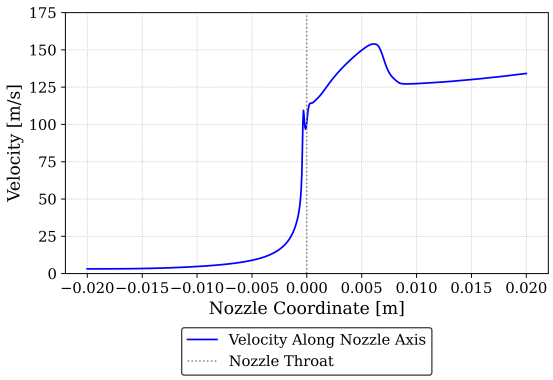

(b) Case 1 (Back pressure = 5.14 MPa): 2D simulation.

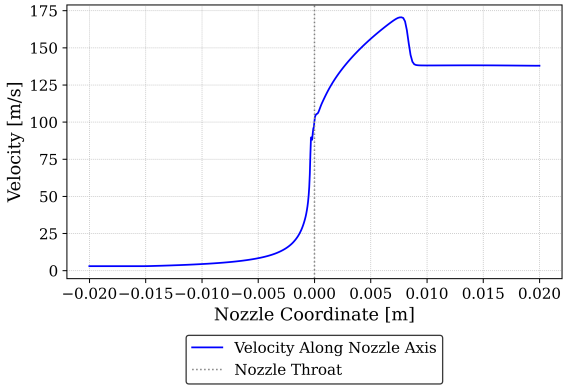

(c) Case 2 (Back pressure = 4.82 MPa): Quasi-1D simulation.

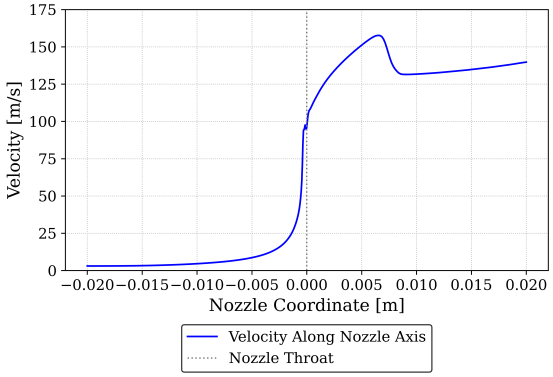

(d) Case 2 (Back pressure = 4.82 MPa): 2D simulation.

Figure 4.5: Axial velocity distributions for quasi-1D and 2D simulations under two back pressure conditions: **Top row:** Case 1 (5.14 MPa); **Bottom row:** Case 2 (4.82 MPa). The profiles illustrate the characteristic acceleration through the converging section and peak velocity shortly after the throat, followed by a deceleration associated with pseudo-shock behaviour in the diverging region. The quasi-1D simulations exhibit steeper velocity rise and sharper deceleration due to inviscid assumptions and absence of wall shear, leading to a more abrupt pseudo-shock. In contrast, the 2D simulations account for viscous and boundary layer effects, resulting in smoother acceleration and a spatially extended pseudo-shock structure. The influence of reduced back pressure in Case 2 enhances expansion and velocity gradients in both configurations.

Quasi-1D Simulation: In the quasi-1D case, the velocity profiles (Figures 4.5a and 4.5c) shows a more pronounced peak of approximately 165.31 m/s in Case 1 and 170.66 m/s in Case 2, occurring shortly after the throat. This elevated velocity is due to the absence of wall resistance due to zero shear walls. This enables the flow to undergo a nearly inviscid expansion, purely driven by the pressure gradients along the streamwise direction.

This idealised expansion is also reflected in the behaviour across the shock region, where the velocity drop occurs abruptly over a narrow axial distance. The lack of physical damping mechanisms such as

viscous shear results in a sharper and more discontinuous pseudo-shock compared to the 2D simulations.

Comparing the two back pressure conditions, Case 2 exhibits a higher peak velocity due to higher pressure ratio between the inlet and outlet when compared to Case 1. This causes more pronounced expansion through the nozzle resulting in stronger flow acceleration.

2D Simulation: In the 2D simulation (Figures 4.5b and 4.5d), the peak velocities are slightly lower than those predicted in the quasi-1D simulations, reaching approximately 153 m/s for Case 1 (back pressure = 5.14 MPa) and 158 m/s for Case 2 (back pressure = 4.82 MPa). This reduction in peak velocity is attributed to the use of no-slip boundary conditions and the inclusion of well-resolved boundary layers, which introduce viscous shear and retard the flow near the wall.

In contrast to the quasi-1D simulations, the velocity drop across the shock region in the 2D simulations is more gradual and distributed over a larger axial distance. The presence of wall effects and viscous dissipation spreads out the shock, resulting in a more physically realistic representation of pseudo-shock behaviour as observed in the experiments of Nakagawa et al. [45].

4.6.1. Velocity Contour Analysis

Figures 4.6, 4.7 and 4.8 display the velocity magnitude contours for both simulations, enabling the visualisation of spatial velocity distribution along with wall interactions.

Quasi-1D simulation: The velocity contour for the quasi-1D simulation reveals no velocity gradient in the transverse direction, which is expected due to the use of slip boundary conditions and a single element along the cross-stream direction. This eliminates the possibility of capturing the boundary layer development in the flow.

The velocity is uniformly distributed in the wall-normal direction. In a narrow region, downstream of the throat, a high-velocity core is visible. This subsequent deceleration is spatially distributed as previously observed in the corresponding line plots (Figures 4.5a and 4.5c), representative of the pseudo-shockwave.

2D simulation: In contrast to quasi-1D simulation, the 2D velocity contour reveals a clear velocity gradient due to the inclusion of the no-slip boundary condition. The inflation layer enable the well resolved boundary layer development (Figures 4.7b and 4.8b) with zero velocity at the wall and gradually increasing along the wall-normal direction towards the freestream.

Due to the viscous shear, the velocity remains significantly lower near the wall while the free stream accelerates and then decelerates across a wide region in the diverging section, indicating a pseudo-shock structure (Figures 4.7a and 4.8a). Unlike the quasi-1D case, the deceleration across the pseudo-shock is spatially distributed over a larger axial distance, as previously shown in Figures 4.5b and 4.5d. This broadening of the pseudo-shock results from viscous dissipation and wall effects. This behaviour is more consistent with experimental observations and highlights the importance of incorporating viscous and multidimensional effects in simulating two-phase CO_2 nozzle flows with shockwaves.

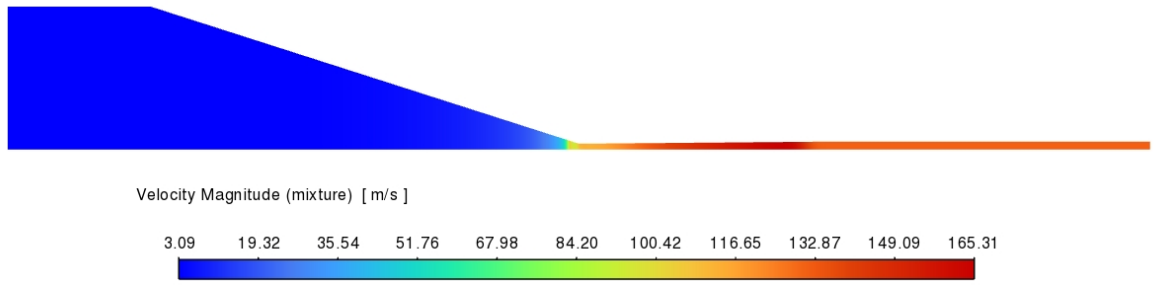

(a) Case 1 (Back pressure = 5.14 MPa): Quasi-1D simulation.

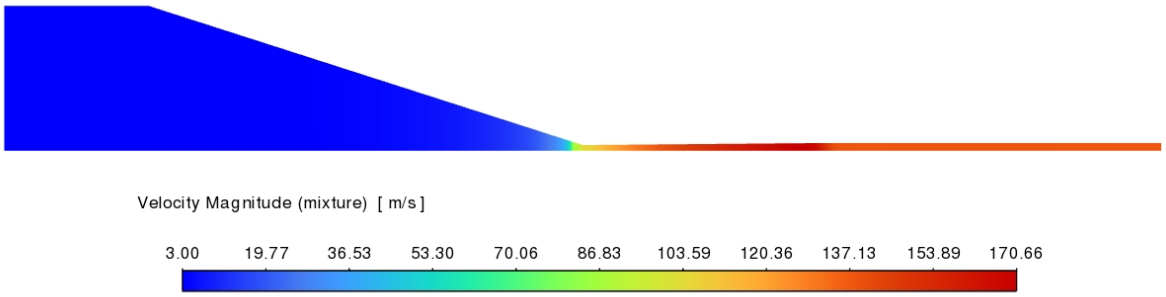

(b) Case 2 (Back pressure = 4.82 MPa): Quasi-1D simulation.

Figure 4.6: Velocity magnitude contours for the quasi-1D simulations at two back pressure conditions. **Top:** Case 1 (back pressure = 5.14 MPa). **Bottom:** Case 2 (back pressure = 4.82 MPa). Both cases exhibit idealised streamwise acceleration and abrupt deceleration across the pseudo-shock region due to the inviscid flow assumptions.

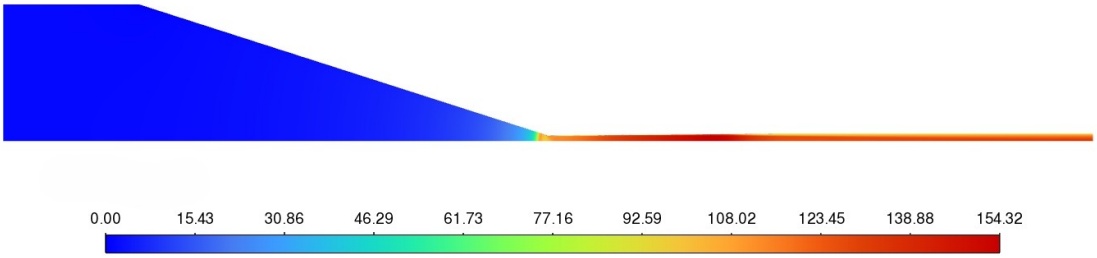

(a) Full view of velocity magnitude contour for Case 1 (back pressure = 5.14 MPa).

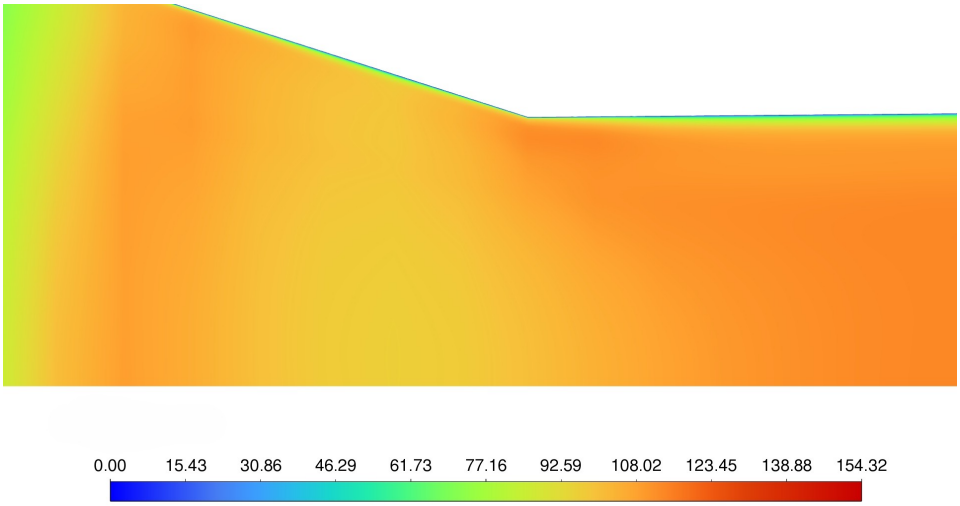

(b) Zoomed-in view near the throat region highlighting boundary layer development for Case 1.

Figure 4.7: Velocity magnitude contours from the 2D simulation for Case 1, showing boundary layer growth and spatially distributed pseudo-shock structure in the diverging section.

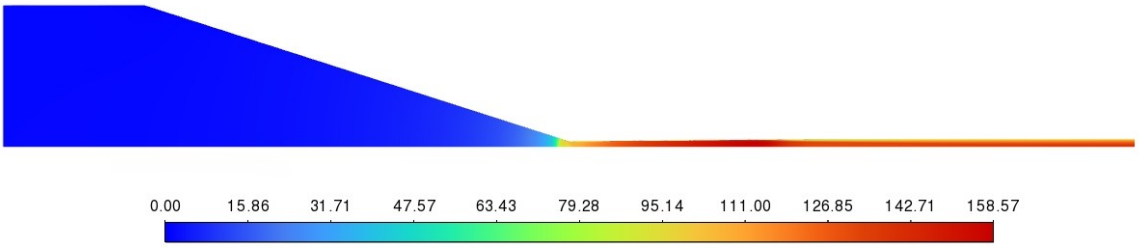

(a) Full view of velocity magnitude contour for Case 2 (back pressure = 4.82 MPa).

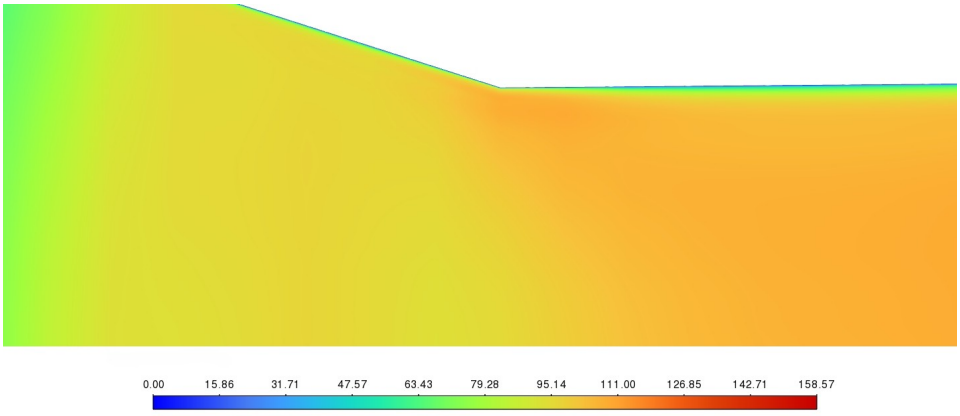

(b) Zoomed-in view near the throat region highlighting boundary layer development for Case 2.

Figure 4.8: Velocity magnitude contours from the 2D simulation for Case 2, showing boundary layer growth and spatially distributed pseudo-shock structure in the diverging section.

4.7. Mach Number Distribution Along Nozzle Axis

The Mach number (M) is a key parameter for characterising the compressible flow behaviour in converging–diverging nozzles. It is defined as the ratio of the local flow velocity (u) to the local speed of sound (a):

$$M = \frac{u}{a} \tag{4.1}$$

However, in the present study, the two-phase speed of sound was computed using Wood's formulation (Equation 2.7) which is essentially a harmonic mean of the speed of sound in liquid and gas phase. Figure 4.9 illustrates the Mach number distribution along the nozzle axis for both quasi-1D and 2D simulations under the two back pressure cases.

Quasi-1D simulations: In the quasi-1D simulations (Figures 4.9a and 4.9c), the Mach number increases steadily through the converging section and rises sharply near the throat. However, sonic condition (M=1) is not reached at the throat but is reached slightly downstream of the throat, attaining peak Mach numbers of approximately $M = 1.03$ for Case 1 and $M = 1.07$ for Case 2. This supersonic regime exists over a short distance following which the flow undergoes deceleration across the pseudo-shock region and exits the nozzle in a subsonic state.

2D simulations: The 2D simulations (Figures 4.9b and 4.9d) exhibit similar qualitative trends. In 2D simulations, the peak Mach numbers are slightly lower than those in the quasi-1D case, with values of $M \approx 0.98$ for Case 1 and $M \approx 1.00$ for Case 2. This reduction is attributed to the inclusion of no-slip boundary conditions and the development of a boundary layer which introduces viscous dissipation and retards the flow near the walls. The pseudo-shock structure in the 2D simulation is more gradual and distributed over a longer axial distance, consistent with the pressure and velocity profiles as discussed in the previous sections.

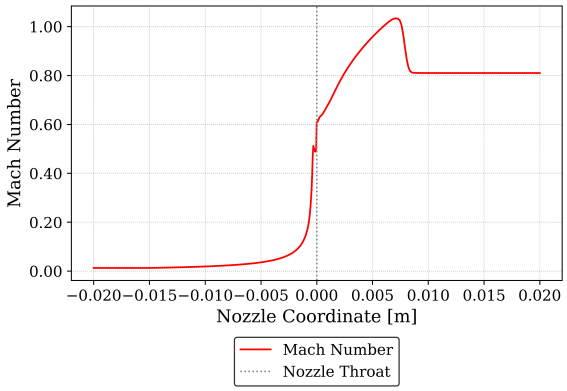

(a) Case 1 (Back pressure = 5.14 MPa): Quasi-1D simulation.

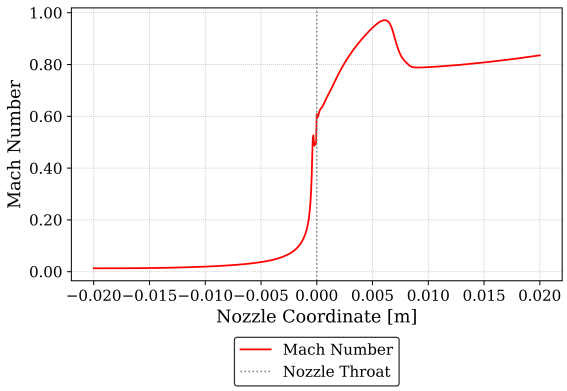

(b) Case 1 (Back pressure = 5.14 MPa): 2D simulation.

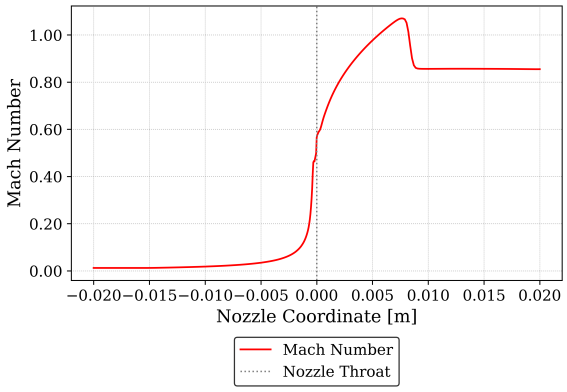

(c) Case 2 (Back pressure = 4.82 MPa): Quasi-1D simulation.

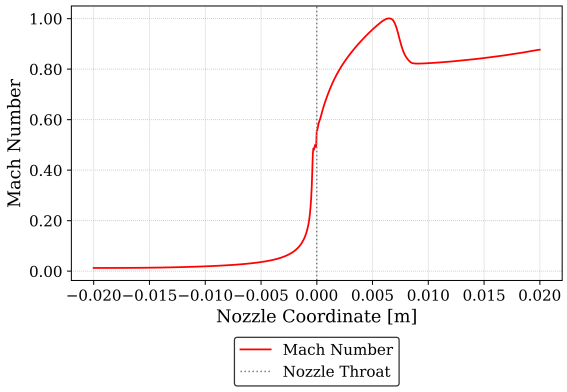

(d) Case 2 (Back pressure = 4.82 MPa): 2D simulation.

Figure 4.9: Axial Mach number distributions for quasi-1D and 2D simulations under two back pressure conditions: **Top row:** Case 1 (5.14 MPa); **Bottom row:** Case 2 (4.82 MPa). The profiles show the transition from subsonic to supersonic flow downstream of the throat, followed by deceleration across a pseudo-shock. The sonic conditions are reached slightly downstream of the throat due to flashing and mixture speed of sound reduction. The 2D results exhibit a more spatially extended pseudo-shock due to wall shear and viscous dissipation. The stronger expansion in Case 2 leads to higher peak Mach number in both geometries.

From all the simulated cases, it is evident that the flow does not reach sonic conditions ($M = 1$) at the

geometric throat. However, the Mach number increases in the diverging section of the nozzle immediately downstream of the throat. This is due to flashing, which induces a transition to two-phase flow starting from the throat. The resulting phase change causes a significant reduction in the fluid density, causing the velocity to increase in the diverging section by the conservation of mass. Furthermore, the speed of sound in a two-phase mixture is significantly lower than in a single phase medium. The combination of the increasing velocity and the reduction in speed of sound has resulted in an increase in Mach number in the diverging section immediately downstream of the throat even though the flow remains subsonic at the throat.

4.8. Slip Velocity Between Phases Along the Nozzle Axis

The current simulation framework allows for the existence of a relative velocity between the liquid and vapour phases in contrast to the Homogeneous Equilibrium Model (HEM) adopted in previous work, which assumes mechanical equilibrium. In flashing flows, the newly formed vapour bubbles accelerate at different rates than the surrounding liquid due to their significantly lower density and inertia. Additionally, the steep gradients in pressure and velocity due to shocks can also cause decoupling between the phases. This non-equilibrium treatment enables more accurate modelling of flow behaviour during rapid phase transition.

Figure 4.10 presents the axial slip velocity profiles for both the quasi-1D and 2D simulations for both the back pressure cases. In this study, the slip velocity u_{slip} has been considered as the difference between vapour phase u_v and liquid phase velocities u_l.

$$u_{\text{slip}} = u_v - u_l \tag{4.2}$$

Quasi-1D Simulations: The slip velocity remains zero in the converging section due to single-phase flow. The slip velocity profiles exhibit sharp oscillations near the throat where rapid depressurisation occurs and the phase change is initiated. Positive slip velocities are observed immediately downstream of the throat, indicating that the low-density vapour accelerates more rapidly than the surrounding liquid as flashing begins. Further downstream, negative slip velocities develop in the pseudo-shock region. This signifies that the vapour is decelerating more strongly than the liquid due to drag and condensation effects. Beyond this region, the slip velocity rapidly approaches zero as the phases equilibrate with each other.

2D Simulations: In the 2D simulations, the slip velocity magnitude is slightly higher than the quasi-1D counterparts. The inclusion of boundary layers and viscous shear causes the interphase velocity differences to sustain over a longer axial distance. The 2D simulation also exhibits a persistent, small slip velocity at the outlet due to shear near the walls resulting from the boundary layer effect.

These significant differences in the velocity between the phases highlight the importance of accounting for the slip between the phases, thus enabling a more physically realistic representation of the flow. Neglecting slip velocity (as in HEM) would enforce mechanical equilibrium, leading to less accurate predictions of flow behaviour in regions of rapid phase change and pseudo-shock formation. The pseudo-shock observed in the present two-phase simulations arises from relaxation effects. Since the

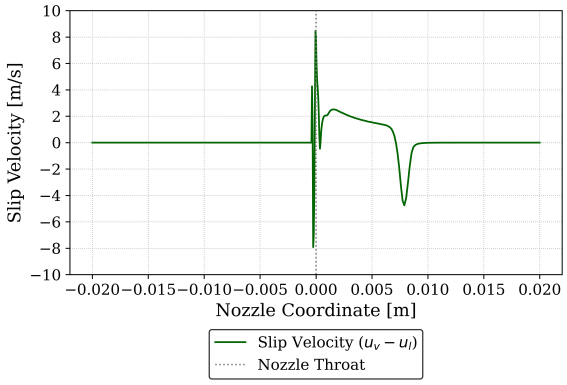

(a) Case 1 (Back pressure = 5.14 MPa): Quasi-1D simulation.

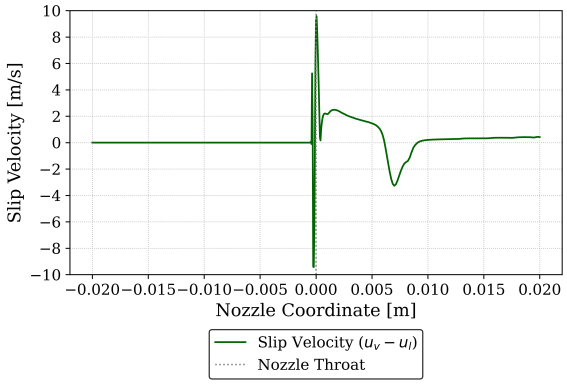

(b) Case 1 (Back pressure = 5.14 MPa): 2D simulation.

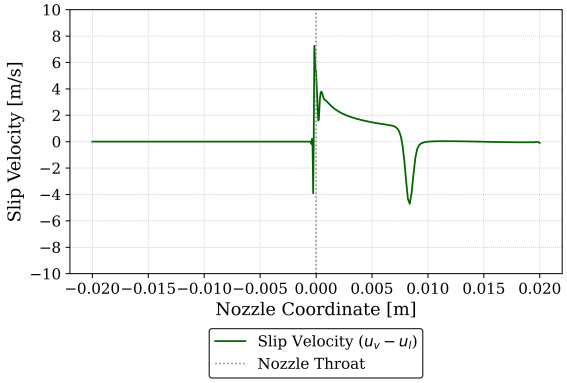

(c) Case 2 (Back pressure = 4.82 MPa): Quasi-1D simulation.

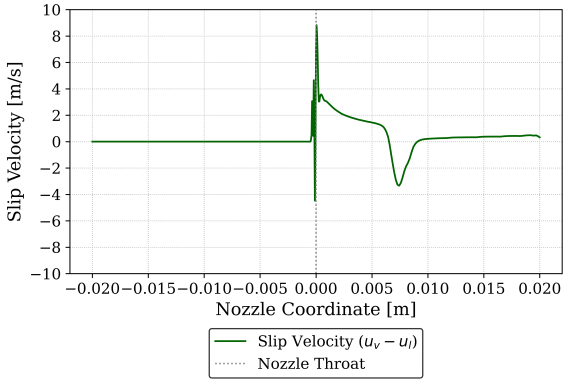

(d) Case 2 (Back pressure = 4.82 MPa): 2D simulation.

Figure 4.10: Comparison of axial slip velocity profiles between quasi-1D and 2D simulations for two back pressure conditions. **Top row:** Case 1 (back pressure = 5.14 MPa). **Bottom row:** Case 2 (back pressure = 4.82 MPa). The slip velocity is computed as the difference between vapour and liquid phase velocities $(u_v - u_l)$, enabling the identification of regions where the two phases exhibit relative acceleration and deceleration. Negative slip develops further downstream in the pseudo-shock region, reflecting stronger vapour deceleration due to condensation.

liquid and vapour phases accelerate and decelerate at different rates, a slip velocity field develops, delaying inter-phase momentum equilibrium. This momentum exchange occurs over a finite length scale, which inhibits the formation of an abrupt normal shock (as observed in single-phase flows). Instead, the pressure recovery is distributed axially, giving rise to a spatially extended pseudo-shock structure. Also, accounting for the slip between phases resulted in a physically realistic distribution of vapour fraction, which will be outlined in Section 4.9.1. Hence, all simulations in this study have been carried out by allowing slip between the phases.

4.9. Vapour Fraction Distribution

The mass-based vapour fraction along the nozzle axis for both the quasi-1D and 2D simulations is presented in Figure 4.11. In *Ansys Fluent*, the vapour fraction is computed on a volumetric basis using the Zwart–Gerber–Belamri cavitation model. However, due to the specific treatment of the Widom line in the present study, the directly reported vapour volume fraction (α_v) is not directly representative of physical phase change.

The Widom line, also referred to as the pseudo-boiling curve, delineates a boundary separating liquid-like and vapour-like behaviour in supercritical fluids. Although no true phase change occurs across this line, it provides a more realistic framework for modelling pseudo-phase change behaviour during the rapid expansion of CO_2 from a supercritical state. In the current simulation, the Widom line was incorporated into the ZGB cavitation model to account for this transition. However, this creates a limitation, which is, whenever the expansion path crosses the Widom line in the supercritical region, the model predicts artificial vapour formation even though no actual phase transition occurs.

As a result, the vapour fraction predicted by *Ansys Fluent* requires post-processing to obtain physically meaningful values. In this study, the vapour fraction was recalculated based on the enthalpy of each thermodynamic state using the relation:

$$x_{\text{mass}} = \frac{h - h_f}{h_g - h_f} \tag{4.3}$$

where h is the specific enthalpy of the fluid, h_f and h_g are the saturated liquid and vapour enthalpies respectively, obtained from the Span–Wagner equation of state. This approach ensures that the vapour fraction reflects only the true phase change that occurs along the saturation curve.

In all the simulations, the vapour fraction remains zero throughout the converging section, indicating a single-phase supercritical liquid regime. The vapour fraction rises steeply near the throat, indicating the onset of flashing due to local pressure drop as the flow expands into the two-phase regime. Downstream of the throat, the vapour fraction reaches a plateau as the expansion continues.

However, in the diverging section corresponding to the pseudo-shock region, there is a slight reduction in the value of vapour fraction. This behaviour is due to the static pressure recovery. As the pressure rises above the vaporisation pressure, some of the vapour re-condenses into the liquid phase, leading to a slight decrease in vapour fraction.

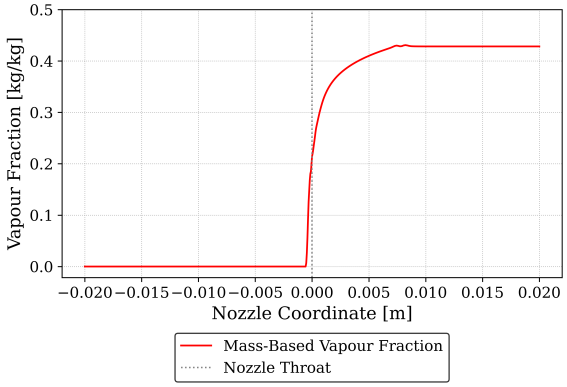

(a) Case 1 (Back pressure = 5.14 MPa): Quasi-1D simulation.

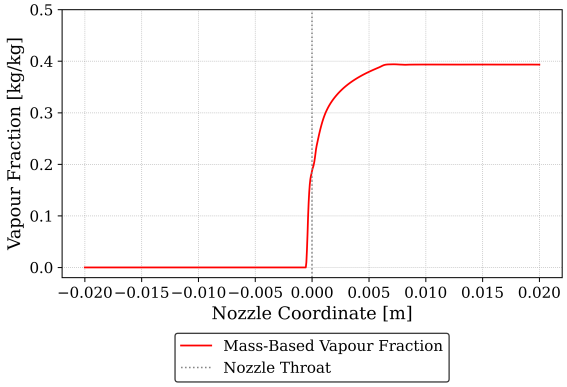

(b) Case 1 (Back pressure = 5.14 MPa): 2D simulation.

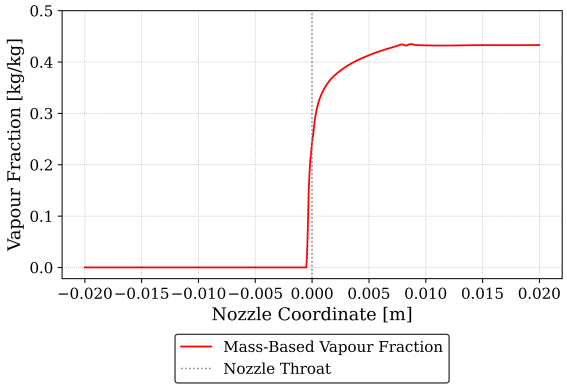

(c) Case 2 (Back pressure = 4.82 MPa): Quasi-1D simulation.

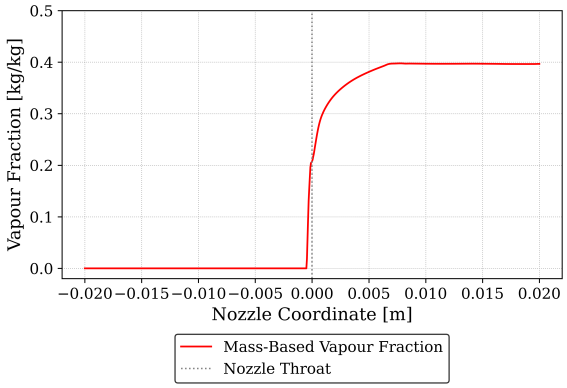

(d) Case 2 (Back pressure = 4.82 MPa): 2D simulation.

Figure 4.11: Axial distribution of mass-based vapour fraction for quasi-1D and 2D simulations under two back pressure conditions: **Top row:** Case 1 (5.14 MPa); **Bottom row:** Case 2 (4.82 MPa). In both cases, vapour formation begins sharply near the throat, corresponding to rapid depressurisation and flashing. The vapour fraction increases downstream and saturates in the diverging section as expansion proceeds. Slight reductions in vapour fraction are observed near the pseudo-shock region, where pressure recovery leads to partial re-condensation.

4.9.1. 2D Contour Analysis of Vapour Fraction Distribution

The contour plots of the vapour fraction from the 2D simulations for Case 1 and 2 are presented in Figures 4.12a and 4.12b respectively. The vapour fraction values shown correspond to mass basis. In the converging section of the nozzle, the vapour fraction remains zero, indicating the supercritical state. Near the throat, the vapour fraction begins to rise indicating the onset of two-phase flow within the system. This behaviour is consistent with the trends discussed earlier in Section 4.9.

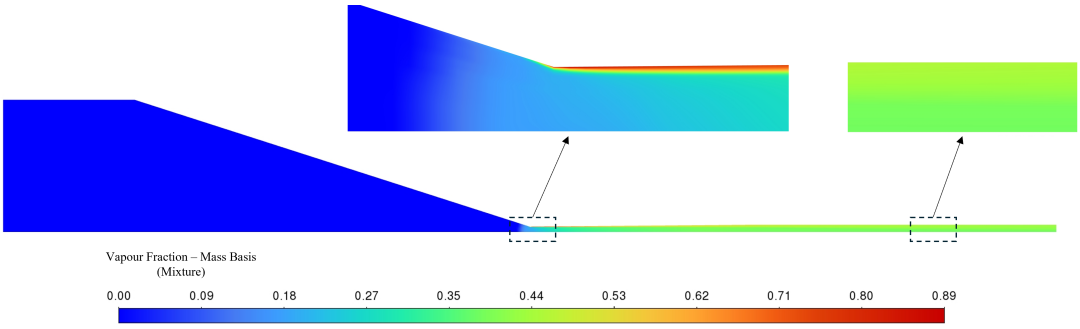

(a) Case 1 (Back pressure = 5.14 MPa): 2D simulation.

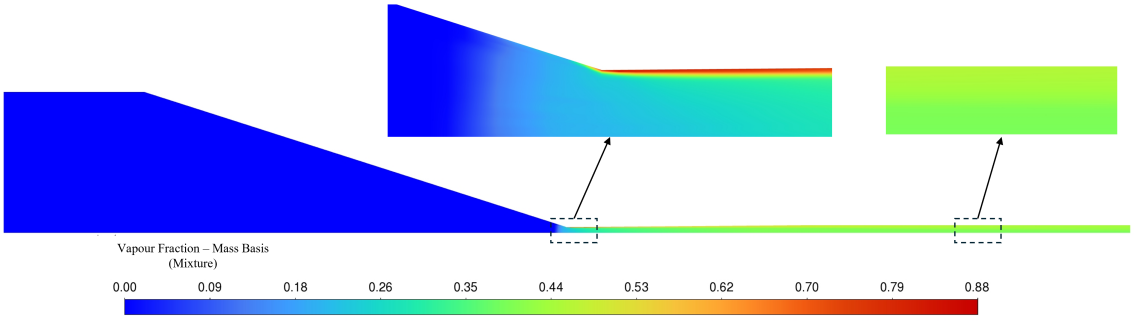

(b) Case 2 (Back pressure = 4.82 MPa): 2D simulation.

Figure 4.12: Mass-based vapour fraction contours from 2D simulations revealing the onset and evolution of phase change in the converging-diverging nozzle. The inclusion of slip between liquid and vapour phases results in higher vapour fraction near the walls immediately downstream of the throat, as the dense liquid phase with higher inertia occupies the core flow while the vapour phase occupies the annular region. Further downstream, as the flow develops, the vapour fraction distribution becomes nearly uniform in the radial direction.

In both the cases, it can be observed that in the diverging section, immediately downstream of the throat, the vapour fraction is relatively high near the walls compared to the freestream region along the nozzle axis. This behaviour is attributed to the mechanical non-equilibrium effect caused by slip between the liquid and vapour phases (mechanical non-equilibrium). Immediately downstream of the throat, the denser liquid phase due to its higher inertia and longer relaxation times is unable to rapidly adapt to the diverging geometry. As the two phase mixture expands, the liquid phase tends to occupy

the region close to nozzle axis forming a characteristic core flow. Consequently, the less dense vapour phase occupies the regions closer to the walls with higher vapour fraction. This forms an annular region close to the walls as consistent with the experimental observations reported by Maxwell et al. [77]. However, further downstream in the diverging section as the flow develops, the vapour fraction distribution becomes nearly uniform along the radial direction as observed from the zoomed contours near the outlet in Figure 4.12.

It is important to note that this radial variation in the vapour fraction downstream of the throat is captured only when slip velocity between phases is accounted for in the simulation framework. In contrast, if the slip between the phases is neglected (as in the previous simulation framework), this physical behaviour cannot be captured. This is evident from Figure 4.13 where the vapour fraction distribution near the walls does not show elevated values compared to that of the core flow. Therefore, the inclusion of slip velocity in multiphase flow modelling of rapidly expanding flows is essential to accurately resolve the actual flow physics.

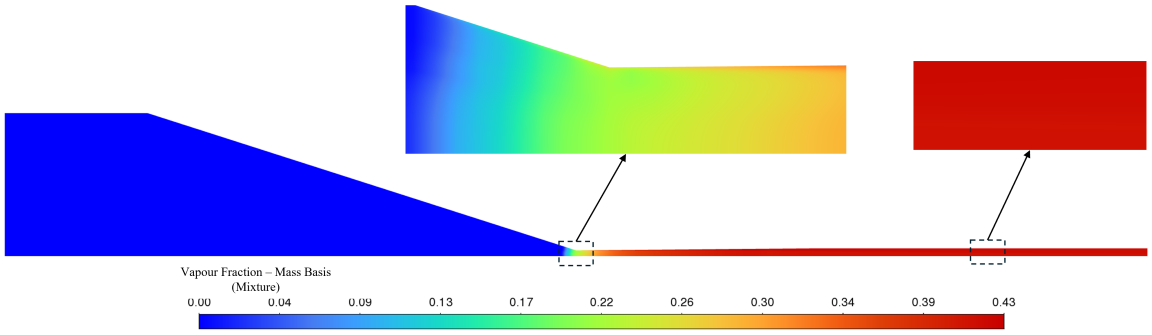

Figure 4.13: Mass-based vapour fraction contours from 2D simulations for back pressure of 5.14 MPa (Case 1). In this simulation, slip between the liquid and vapour phases was not considered resulting in the assumption of mechanical equilibrium between phases as in previous simulation framework. This simplification led to a more uniform vapour fraction distribution across the radial direction immediately downstream of the nozzle throat, in contrast to the significant radial variations observed in experiments and in simulations that account for slip effects.

4.10. Pressure - Temperature Diagram of the Expansion Process Along the Nozzle Axis

The pressure-temperature expansion paths for both quasi-1D and 2D simulations are illustrated in Figure 4.14 under the two back pressure conditions. The expansion paths are plotted against the saturation line and Widom line of CO_2, along with the critical point and the inlet and outlet thermodynamic states. The saturation line delineates the two-phase boundary, while the Widom line delineates the liquid-like and vapour-like states in the supercritical region.

In all the simulations, temperature values were obtained directly from *Ansys Fluent*. The static pressure values upstream of the throat were taken directly from *Fluent*, whereas downstream pressures were post-processed using the simulated static temperatures and mapped to the corresponding saturation pressures, as described in Section 4.3.

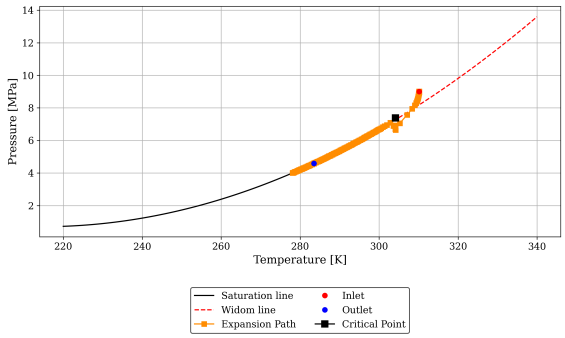

(a) Case 1 (Back pressure = 5.14 MPa): Quasi-1D simulation.

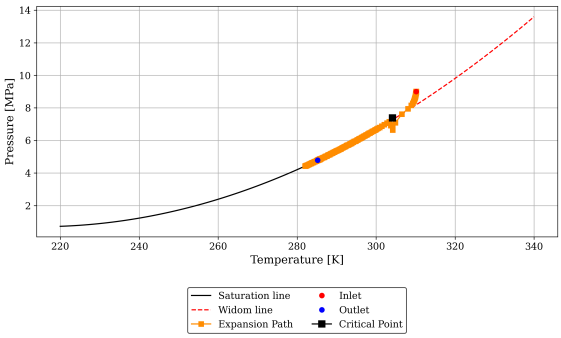

(b) Case 1 (Back pressure = 5.14 MPa): 2D simulation.

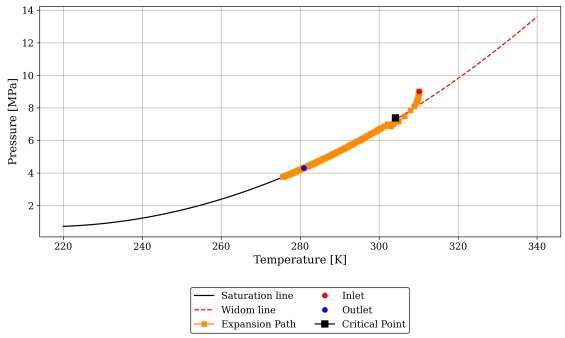

(c) Case 2 (Back pressure = 4.82 MPa): Quasi-1D simulation.

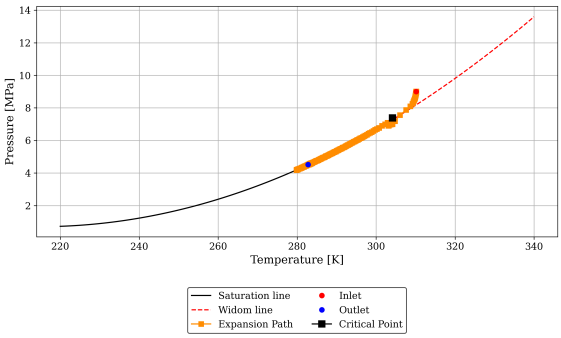

(d) Case 2 (Back pressure = 4.82 MPa): 2D simulation.

Figure 4.14: Pressure–temperature (P–T) expansion paths of CO_2 along the nozzle axis for quasi-1D and 2D simulations under two back pressure conditions. **Top row:** Case 1 (5.14 MPa). **Bottom row:** Case 2 (4.82 MPa). Each path is plotted against the saturation and Widom line. The location of the critical point provides thermodynamic context. Inlet and outlet states are also marked for reference. The expansion initiates in the supercritical region and crosses the Widom line before aligning with the saturation line downstream of the throat, signifying the onset of two-phase flow. Minor oscillations near the critical region arise from steep thermophysical gradients but do not affect the overall trend. The close coupling of the expansion path with the saturation line downstream confirms the consistency of the thermodynamic states with vapour fraction evolution presented in Figure 4.11.

In all the cases, the expansion begins in a supercritical state and progresses towards the two-phase region. The use of both the saturation and Widom lines in the ZGB cavitation model enables the simulation to capture the pseudo-phase transition behaviour during rapid depressurisation. Without incorporating the Widom line, the expansion path tends to deviate unphysically, following an isothermal trajectory, directly entering the vapour phase, inconsistent with the experimental observations. The Widom line corrects for the pseudo-phase transition behaviour that occurs before reaching the saturation dome in supercritical fluids.

Starting from the throat and until the outlet, the $P-T$ expansion path is coupled to the saturation line, indicating two-phase flow in the system. This behaviour is consistent with the vapour fraction values obtained in the simulation as shown in Figure 4.11. In the vicinity of the critical point, minor oscillations were observed in the expansion path due to the pressure fluctuations arising from the steep gradients in thermodynamic properties. However, these fluctuations were not found to affect the overall expansion trend and were not observed downstream of the throat.

4.11. Temperature - Specific Entropy Diagram of the Expansion Process Along the Nozzle Axis

The expansion process of supercritical carbon dioxide for both quasi-1D and 2D simulations is depicted in the temperature-specific entropy (T-s) diagram shown in Figure 4.15. The saturation dome separates the single-phase region (outside the dome) from the two-phase regions (inside the dome) of the carbon dioxide. The left and right boundaries of the dome represent the saturated liquid and vapour lines, respectively. The critical point lies at the apex of the dome, where the saturated liquid and vapour lines converge. This serves as the boundary between the supercritical and sub-critical regions.

The iso-quality lines are overlaid on the T-s diagram which indicate the lines of constant mass based vapour fraction. The static temperature values for the expansion path have been directly obtained from *Ansys Fluent*. The specific entropy values were computed using *CoolProp* and plotted.

The ideal expansion process in a converging-diverging nozzle is isentropic in nature, with entropy remaining constant throughout the expansion process. However, in the physical process and these simulations, the process is observed to be non-isentropic as shown by the deviation of the process towards higher entropy values from the isentropic expansion path. This deviation arises due to real gas effects and the irreversibilities introduced in the process due to viscous dissipation. The rise in entropy close to the outlet corresponds to the pseudo-shock region, where the abrupt pressure recovery generates further irreversibility.

The expansion starts from a supercritical state (outside the saturation dome) and ventures into the two-phase region, entering the saturated liquid domain as consistent with the observations of Nakagawa et al. in the experiments [45]. As the depressurisation continues, the vapour fraction of the fluid is found to increase gradually along the expansion path. The vapour fraction values inferred from the T-s diagrams were found to correlate with those calculated from the enthalpy values in Figure 4.11.

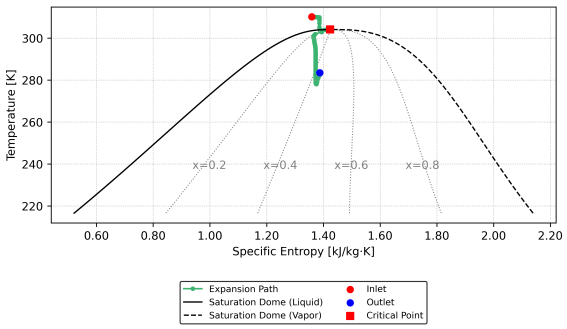

(a) Case 1 (Back pressure = 5.14 MPa): Quasi-1D simulation.

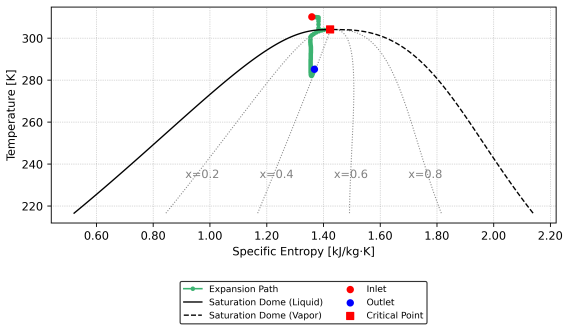

(b) Case 1 (Back pressure = 5.14 MPa): 2D simulation.

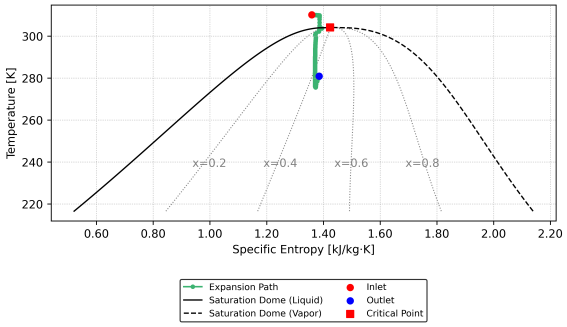

(c) Case 2 (Back pressure = 4.82 MPa): Quasi-1D simulation.

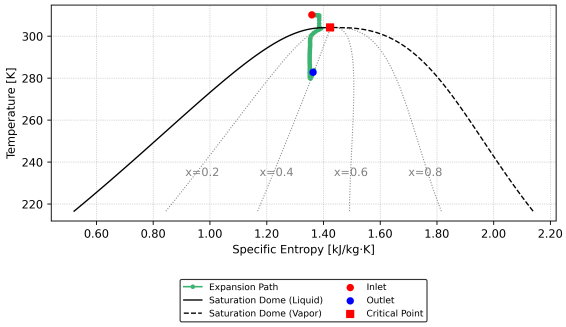

(d) Case 2 (Back pressure = 4.82 MPa): 2D simulation.

Figure 4.15: Temperature–specific entropy (T–s) expansion paths of CO_2 for quasi-1D and 2D simulations under two back pressure conditions. **Top row:** Case 1 (5.14 MPa). **Bottom row:** Case 2 (4.82 MPa). The saturation dome is constructed from the Span–Wagner equation of state, with iso-quality lines indicating constant vapour fractions overlaid for reference. The expansion begins in the supercritical region and traverses into the two-phase domain as the flow depressurises through the nozzle. The entry into the dome indicates the onset of flashing, where vapour starts to form due to local pressure drop. The quasi-1D and 2D paths both show a continuous rise in entropy, confirming the non-isentropic nature of the expansion, primarily due to viscous dissipation, real gas effects and interfacial momentum exchange. The vapour quality along the path aligns with the mass-based vapour fraction profiles discussed earlier (see Figure 4.11), further validating the accuracy of the thermodynamic modelling.

4.12. Joule–Thomson Coefficient Along the Nozzle Axis

The rate of change of temperature with respect to pressure during an isenthalpic process is quantified using the Joule-Thomson (JT) coefficient and is generally defined as,

$$\mu_{JT} = \left(\frac{\partial T}{\partial P}\right)_h \tag{4.4}$$

In this study, μ_{JT} was computed using an equivalent thermodynamic identity as follows,

$$\mu_{JT} = -\frac{1}{c_p}\left(\frac{\partial h}{\partial P}\right)_T \tag{4.5}$$

This formulation is convenient for numerical implementation, because the thermodynamic properties such as c_p and $(\partial h/\partial P)_T$ can be directly extracted from the thermodynamic fluid property libraries using the Span-Wagner equation of state. The values of these properties in the two-phase region were computed as the mass fraction weighted mixture values as defined by the following equations.

$$c_{p,\text{mix}} = x_{\text{mass}} \cdot c_{p,v} + (1 - x_{\text{mass}}) \cdot c_{p,l} \tag{4.6}$$

$$\left(\frac{\partial h}{\partial P}\right)_{\text{mix}} = x_{\text{mass}} \cdot \left(\frac{\partial h}{\partial P}\right)_v + (1 - x_{\text{mass}}) \cdot \left(\frac{\partial h}{\partial P}\right)_l \tag{4.7}$$

A positive values of μ_{JT} indicates that the fluid undergoes cooling during the expansion process and a negative value implies that it heats up during the expansion. For the range of temperatures and pressures investigated in this study, CO_2 exhibits a positive value of Joule Thomson coefficient, indicating cooling during the expansion process [19].

Figure 4.16 presents the computed values of JT coefficient along the nozzle expansion path for both quasi-1D and 2D simulations. The simulations begin at supercritical inlet conditions (9 MPa, 310.15 K), and the fluid undergoes flashing in the diverging section starting from the throat. Case 1 corresponds to an outlet pressure of 5.14 MPa, while Case 2 is for 4.82 MPa. The values of Joule-Thomson coefficient remain positive throughout the expansion, consistent with the physical behaviour of carbon dioxide.

Across all simulations, the JT coefficient initially increases from approximately 4 K/MPa to 5 K/MPa in the supercritical region. This is associated with sensible cooling as the fluid expands without any phase change. In the proximity of the critical point, minor fluctuations are observed in the JT coefficient which is attributed to the sharp variation of c_p values.

As the expansion enters the two-phase region, the JT coefficient values stabilise to a nearly constant value of approximately 5 K/MPa. This is because in the two-phase region the temperature values are coupled to the values of saturation pressure. The drop in pressure causes evaporation in the system which is accompanied by the release of latent heat. Hence, saturation cooling is observed in this region.

The plateau value of the Joule-Thomson coefficient can be helpful in providing a first-order estimate of the temperature drop during the rapid depressurisation of supercritical carbon dioxide. This can aid in the preliminary material selection and design considerations for the flow control devices.

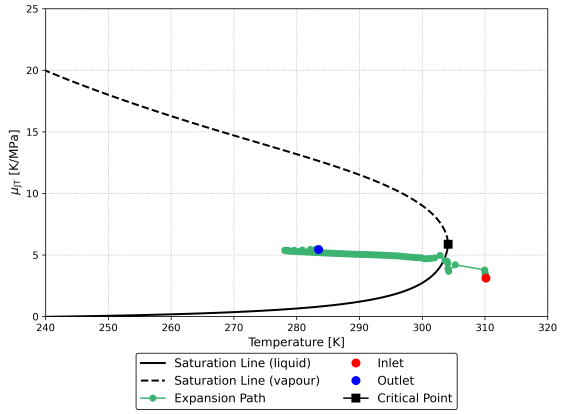

(a) Case 1 (Back pressure = 5.14 MPa): Quasi-1D simulation.

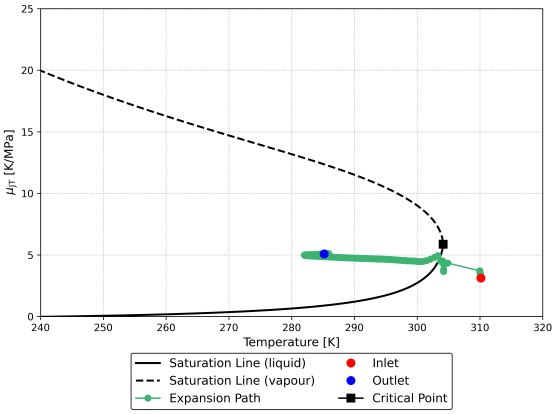

(b) Case 1 (Back pressure = 5.14 MPa): 2D simulation.

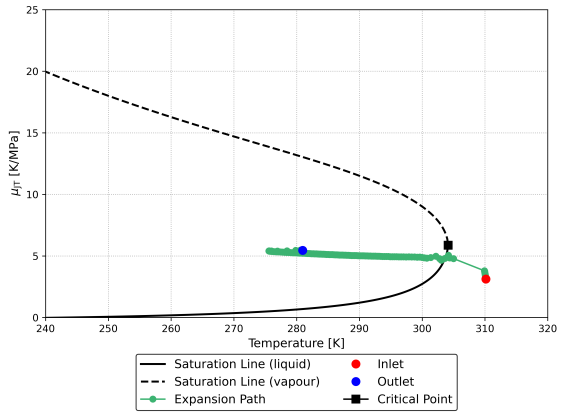

(c) Case 2 (Back pressure = 4.82 MPa): Quasi-1D simulation.

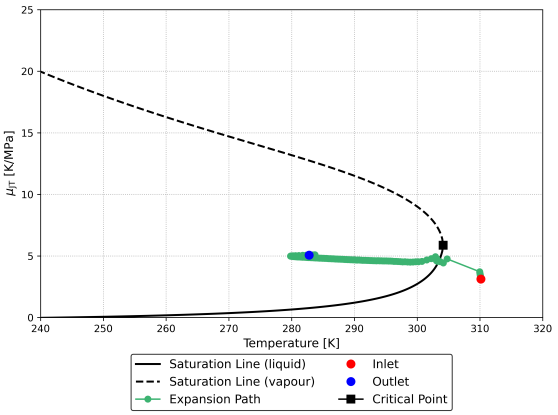

(d) Case 2 (Back pressure = 4.82 MPa): 2D simulation.

Figure 4.16: Joule–Thomson coefficient (μ_{JT}) variation along the expansion path for quasi-1D and 2D simulations, overlaid on the saturation dome of CO_2. **Top row:** Case 1 (back pressure = 5.14 MPa); **Bottom row:** Case 2 (back pressure = 4.82 MPa). The expansion begins from supercritical conditions near the critical point and proceeds toward the two-phase region. The JT coefficient remains positive throughout, indicating that CO_2 undergoes cooling during isenthalpic expansion. In the supercritical region, the increase in μ_{JT} reflects sensible cooling, while its plateau in the two-phase region corresponds to saturation-controlled temperature drop. Minor fluctuations near the critical point arise due to large variations in c_p.

4.13. Effect of Surface Tension

The simulations presented in the previous sections did not include the surface tension effects. To assess the role of surface tension in the expansion dynamics of supercritical CO_2, the simulations (corresponding to Case 1) were performed both with and without surface tension enabled. The Continuum Surface Stress (CSS) model was used in *Ansys Fluent*, which incorporates surface tension as a conservative surface stress tensor as described in Section 3.3. The surface tension coefficient was defined using the Brock and Bird correlation.

At the inlet temperature of 310.15 K, CO_2 is in a supercritical state where the phase boundaries do not exist and the surface tension is theoretically zero. Even in the diverging section where two-phase flow exists, the surface tension is extremely low, with a magnitude of 3 mN $\cdot$ m^{-1} This makes the effect of surface tension very low compared to other dominant forces.

The comparison of post-processed pressure profiles from the quasi-1D simulation for Case 1 (back pressure = 5.14 MPa) with and without surface tension is shown in Figure 4.17. The near-perfect overlap of both the pressure profiles confirms that the presence of surface tension does not significantly alter the pressure distribution and the shock behaviour.

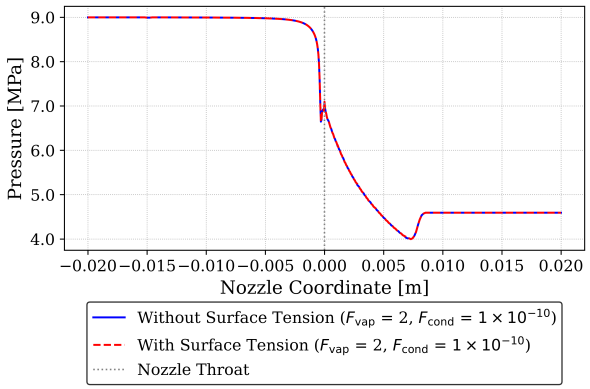

Figure 4.17: Comparison of post-processed pressure profiles along the nozzle axis with and without surface tension effects in the quasi-1D simulation. The overlap of the curves demonstrates that surface tension has negligible influence under the current operating conditions.

The behaviour of the pressure distribution is physically consistent with the low surface tension of CO_2, whose values are too small to affect the overall pressure distribution. Thus, the exclusion of surface tension not only simplifies the numerical model but also reduces the computational cost without affecting the accuracy of the simulations. Hence, the surface tension can be neglected for similar flow regimes.

4.14. Effect of Bubble Radius in ZGB Cavitation Model

The selection of an appropriate bubble radius is a critical parameter in the ZGB cavitation model, as it directly influences the rate of phase change. As discussed in Sub-Section 3.6.2, the default bubble radius prescribed by *Ansys Fluent* in ZGB cavitation model is 1×10^{-6} m and the same value has been employed in all the simulations discussed in the study. Whereas, the estimated critical bubble radius at the throat where phase change process is initiated in this geometry was calculated to be 1.13×10^{-7} m (at 304 K). This value, however represents only the minimum radius for thermodynamic stability and

physically the bubble grows in size beyond the critical radius once the nucleation is initiated. Since, the ZGB model assumes a constant bubble radius throughout the phase change process and does not dynamically account for bubble growth, the use of default radius prescribed by *Ansys Fluent* remains a reasonable approximation as long as the value is equal to or larger than the critical bubble radius and lies within a physically admissible range.

To explore the sensitivity of the ZGB cavitation model to this parameter, simulations were conducted using two different bubble radii: the default value of 1×10^{-6} m and the critical radius of 1.13×10^{-7} m. In both cases, the evaporation and condensation coefficients were initially held constant ($F_{\text{vap}} = 2$, $F_{\text{cond}} = 1 \times 10^{-08}$) to study the effect of bubble radius alone.

The governing mass transfer rates in the ZGB cavitation model are defined as follows:

$$R_e = F_{\text{vap}} \frac{3\alpha_{\text{nuc}}(1-\alpha_v)\rho_v}{R_B} \sqrt{\frac{2}{3} \cdot \frac{P_v - P}{\rho_l}} \tag{4.8}$$

Whereas when the local pressure increases above the vapour pressure of the liquid (P > P_v) condensation occurs,

$$R_c = F_{\text{cond}} \frac{3\alpha_v \rho_v}{R_B} \sqrt{\frac{2}{3} \cdot \frac{P - P_v}{\rho_l}} \tag{4.9}$$

where:

- R_B is the bubble radius, which is by default considered as 1×10^{-6} m (here an additional radius of 1.13×10^{-7} was also considered)
- α_{nuc} is nucleation site volume fraction, typically 5×10^{-4}
- F_{vap} is the empirical evaporation coefficient
- F_{cond} is the empirical condensation coefficient
- ρ_l is the liquid density
- P_v is the vapor pressure (saturation pressure)
- P is the local pressure
- α_v is the vapour volume fraction

As illustrated in Figure 4.18, the pressure profiles resulting from the two radii exhibit noticeable differences. Specifically, the smaller bubble radius leads to a more aggressive pressure drop and a steeper recovery. This behaviour is directly attributable to the governing equations (Equations 4.8 and 4.9) in the ZGB model, where the mass transfer rates for evaporation and condensation are inversely proportional to the bubble radius. For a given volume fraction, smaller bubbles will have more surface area for mass transfer than larger bubbles. Thus, a reduction in the value of bubble radius used in the cavitation model leads to an amplified rate of phase transition, which in turn affects the pressure evolution in the nozzle.

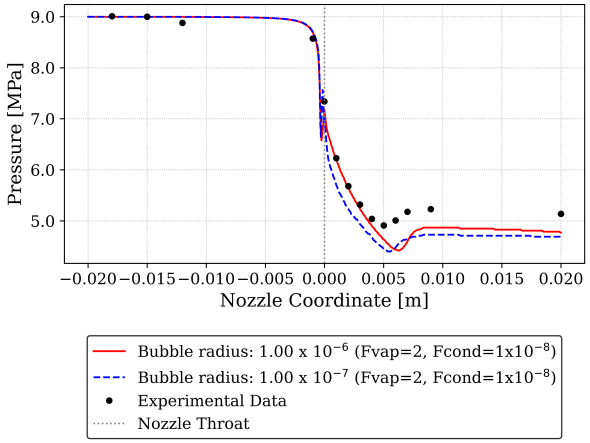

Figure 4.18: Effect of bubble radius on axial pressure distribution in the quasi-1D simulation, using empirical coefficients $F_{\text{vap}} = 2$ and $F_{\text{cond}} = 1 \times 10^{-08}$. The experimental pressure profile has been overlayed with black markers.

To compensate for this rapid phase change behaviour with a smaller bubble radius, a second simulation was performed in which the empirical coefficients were scaled appropriately. Given the inverse relationship between bubble radius and the phase change rates, the reduction of bubble radius by a factor of 10 was counterbalanced by reducing the empirical coefficients by the same factor ($F_{\text{vap}} = 0.2$, $F_{\text{cond}} = 1 \times 10^{-09}$). The resulting pressure profiles are shown in Figure 4.19.

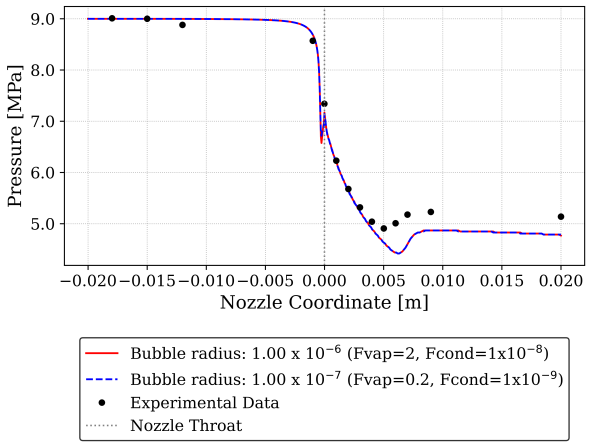

Figure 4.19: Pressure profiles along the nozzle axis in quasi-1D simulation after tuning empirical coefficients to compensate for reduced bubble radius. For the baseline case, a bubble radius of 1×10^{-6} m was used with $F_{\text{vap}} = 2$ and $F_{\text{cond}} = 1 \times 10^{-08}$. For the critical radius case (1.13×10^{-7} m), the coefficients have to be proportionally scaled down to $F_{\text{vap}} = 0.2$ and $F_{\text{cond}} = 1 \times 10^{-09}$ to offset the amplified phase transition rate. The tuned profile for the smaller radius shows strong agreement with the baseline and thus with the experimental profile, demonstrating that appropriate calibration of empirical coefficients can restore consistency in pressure predictions.

As observed, the adjusted pressure profile with $R_b = 1.13 \times 10^{-7}$ m aligns closely with the baseline case using the default radius, thereby restoring agreement with experimental trends. This demonstrates the flexibility of the ZGB cavitation model in accommodating variations in physical parameters, provided the empirical coefficients are appropriately tuned.

It is important to note that the ZGB model assumes a constant bubble radius and relies on tuning of

empirical coefficients to mimic the metastable behaviour. In summary, any bubble radius greater than or equal to the critical value can be used within the ZGB framework, provided the empirical coefficients are calibrated accordingly to match the experimental profile. This highlights both the model's flexibility and its limitation of reliance on empirical cavitation coefficient tuning to accurately simulate the phase change behaviour.

In summary, the application of the Savitzky–Golay filter proved to be crucial in achieving numerically converged solutions for simulation supercritical CO_2 flows which are particularly prone to divergence due to the steep thermodynamic gradients near the critical point. Although the smoothing process introduced a slight attenuation of the thermodynamic properties, its impact on the overall results was minimal as evident from the results. The predicted mass flux exhibited a moderate deviation from experimental values but the error percentages were less than 20 % and were comparable to the mass flux errors reported by Hammer et al. [55] for phase transition models that do not explicitly account for metastable behaviour. Furthermore, the simulated pressure profiles closely aligned with experimental pressure profiles of [45].

The inclusion of slip velocity between phases was also found to be essential in accurately capturing the phase transition dynamics. Surface tension effects were shown to have a negligible influence on the overall flow behaviour. The observations from this work provided valuable insights into the supercritical carbon dioxide simulations. The identified limitations gave a good basis for the potential improvements in the modelling strategies and will be discussed in Chapter 6.

5

Conclusion

This study explored the phase transition dynamics of supercritical carbon dioxide during rapid depressurisation in a converging-diverging nozzle, a simplified yet representative geometry for control valves, due to its direct relevance to CO_2 depressurisation process within the CCS infrastructure. Building upon the foundational work of Bob Fluttert [16], which provided valuable insights into flashing behaviour under dense liquid conditions, the present study extended the simulation framework to cover supercritical inlet states. This extension necessitated the adoption of numerical strategies to address the steep thermodynamic gradients near the critical point and to ensure solver robustness.

A key enhancement was the implementation of the Span-Wagner equation of state from *REFPROP* via a non-uniform lookup table with increased grid refinement close to the critical temperature and pressure, where abrupt variations in the thermodynamic properties are observed. This approach was coupled with the application of a Savitzky-Golay filter to suppress the spurious peaks in the thermodynamic data, without compromising the thermodynamic fidelity. This combined approach mitigates the numerical stability issues encountered by the solver during the solution process. Furthermore, the mixture multiphase model was enhanced by relaxing the Homogeneous Equilibrium assumptions and incorporating interphase slip velocity to capture mechanical non-equilibrium. The Zwart-Gerber-Belamri cavitation model was adapted and modified to include the turbulence effects. The non-equilibrium phase transition process, as physically observed during the rapid depressurisation process was replicated in the simulation by calibrating the cavitation coefficients.

The simulations were performed using both quasi-one-dimensional and two-dimensional planar geometries with the thermodynamic conditions corresponding to the experiments of Nakagawa et al. [45]. Comparison of simulation results with the experimental data highlighted the necessity of mechanical non-equilibrium in accurately capturing the onset and evolution of the vapour fraction. The 2D simulations incorporating no-slip boundary conditions and viscous effects demonstrated better agreement with experimental results in terms of pressure distribution, pseudo-shock behaviour and vapour distribution. The influence of surface tension was investigated and was found to be negligible owing to the intrinsically low surface tension of CO_2 in the investigated thermodynamic conditions. Additionally, a

sensitivity analysis of the bubble radius within the cavitation model was conducted to better understand its impact on the phase transition behaviour.

The simulated mass flow rates were found to slightly underpredict the experimental values due to two factors. Firstly, the smoothing operation has resulted in mild attenuation of the thermodynamic properties. Secondly, the present simulation does not explicitly account for the metastable effects and instead assumes near-instantaneous thermodynamic equilibrium once the saturation conditions are reached. Together, these factors contribute to a premature onset of flashing and a reduction in the fluid's density near the critical point, thereby lowering the predicted mass flow rate. Despite these limitations, the overall trends in results such as axial pressure distribution, velocity profiles and vapour fraction evolution remain consistent with experimental observations, demonstrating that the proposed modelling framework captures the key physical phenomena and offers a reliable foundation for further investigations.

In summary, this study presents a robust, scalable and physically consistent computational methodology for simulating the depressurisation of supercritical CO_2 through converging-diverging nozzles, which can be extended to more complex valve geometries in CCS systems. This framework lays the groundwork for future developments in predictive modelling of supercritical phase transitions, supporting the flow assurance and reliability of flow control devices in CCS applications.

6

Recommendations

This study has resulted in a robust framework for simulating supercritical CO_2 flows, building upon the earlier work of Bob Fluttert [16]. The following recommendations are proposed to extend this work and further enhance the modelling of supercritical CO_2 flows in control valves for carbon capture and storage applications.

The Zwart–Gerber–Belamri (ZGB) cavitation model employed in this study does not explicitly account for the metastable states in the fluid. Consequently, the empirical cavitation coefficients (F_{vap} and F_{cond}) had to be iteratively tuned to align with experimental results. While a parametric study across a wide range of test cases could provide heuristics for selecting appropriate coefficients, this approach may lack flexibility for new geometries and boundary conditions. Future studies could explore advanced models that account for the detailed physics of nucleation, such as the Homogeneous Flashing Model (HFM) [63]. This model is capable of predicting homogeneous nucleation with high accuracy via Classical Nucleation Theory. However, it relies on empirical assumptions for heterogeneous nucleation, as it is highly dependent on geometrical features such as surface roughness. Moreover, implementation of HFM models would require custom solvers.

The present study utilised an Euler–Euler approach, where both phases are treated as interpenetrating continua. While this approach offers a balance between computational efficiency and accuracy, the Euler–Lagrange framework provides a more detailed representation by modelling the nucleating phase as discrete particles within a continuous flow field for the primary phase. Although this method is computationally more expensive, it can capture the detailed dynamics of bubble growth and collapse with higher fidelity and may be explored in future work.

To address numerical instabilities near the critical point, a Savitzky–Golay filter was applied to smooth abrupt variations in the thermodynamic property lookup tables. Although this filtering introduced a minor attenuation of thermodynamic peaks, there was a good agreement between the simulation and experimental results. An alternative strategy worth exploring is the implementation of Quasi-Symmetric Sampling (QSS) [78]. This is an adaptive sampling technique that avoids placing grid points directly on

thermodynamic singularities and applies finer resolution in regions of steep property variation. Although QSS inherently reduces abrupt variations without requiring post-processing smoothing, it can also introduce some attenuation in the data. A comparative study between QSS-based property tables and Savitzky–Golay filtered tables could be carried out to assess their relative accuracy and computational performance.

The RANS turbulence model used in this study offered a good balance between accuracy and computational cost. More advanced turbulence models available in *Ansys Fluent* such as the Reynolds Stress Model (RSM) or hybrid approaches like Scale-Adaptive Simulation (SAS) and Detached Eddy Simulation (DES) may be investigated. These models may better capture turbulence phase interactions in rapid expansions and pseudo-shock regions, offering deeper insights into flow physics.

This study focused on quasi-1D and 2D converging–diverging nozzles as a simplified starting case. To better replicate the actual operating scenario, future simulations could be extended to full three-dimensional control valve geometries considering the trim components such as seat ring, cage and plug. This would enable the assessment of complex flow patterns within the valve. However, there is a lack of experimental references to validate such 2D and 3D simulations. Experimental campaigns at facilities such as the Colorado CO_2 Flow Loop at TNO could be conducted to generate data for validating the computational framework.

References

[1] European Commission. *Proposal for a Council Decision on the position to be adopted on behalf of the European Union within the EU-UK Joint Committee on the determination of the conditions for participation in Union programmes by the United Kingdom*. https://eur-lex.europa.eu/legal-content/EN/TXT/?uri=COM%3A2024%3A63%3AFIN. Accessed: 2024-12-13. 2024.

[2] European Commission. *Commission Staff Working Document: Impact Assessment Accompanying the Proposal for a Council Decision on the Position to be Adopted on Behalf of the European Union within the EU-UK Joint Committee*. https://eur-lex.europa.eu/legal-content/EN/TXT/?uri=CELEX%3A52024SC0063. Accessed: 2024-12-13. 2024.

[3] P.R. Shukla et al., eds. *Climate Change 2022: Mitigation of Climate Change*. Contribution of Working Group III to the Sixth Assessment Report of the Intergovernmental Panel on Climate Change. Cambridge, UK and New York, NY, USA: Cambridge University Press, 2022. doi: 10.1017/9781009157926.

[4] European Commission. *Commission Staff Working Document: Impact Assessment Report - Part 1: Accompanying the Document*. https://eur-lex.europa.eu/legal-content/EN/TXT/HTML/?uri=SWD%3A2024%3A63%3AFIN. Accessed: 2024-12-13. 2024.

[5] Global CCS Institute. *Global Status of CCS 2022*. Tech. rep. Accessed: 2024-12-15. Global CCS Institute, 2022. url: %5Curl%7Bhttps://status22.globalccsinstitute.com/wp-content/uploads/2023/03/GCCSI_Global-Report-2022_PDF_FINAL-01-03-23.pdf%7D.

[6] Global CCS Institute. *CCS in Europe: Regional Overview*. Tech. rep. Accessed: 2024-12-15. Global CCS Institute, 2023. url: %5Curl%7Bhttps://www.globalccsinstitute.com/wp-content/uploads/2023/11/CCS-in-Europe-Regional-Overview-Global-CCS-Institute-pdf.pdf%7D.

[7] Porthos CO_2. *Porthos: CO_2 Transport and Storage in Rotterdam*. Accessed: 2024-12-15. 2024. url: %5Curl%7Bhttps://www.porthosco2.nl/en/%7D.

[8] Statista. *Netherlands: CO2 emissions 1960-2022*. Accessed: 2025-01-07. 2025. url: https://www.statista.com/statistics/449784/co2-emissions-netherlands/.

[9] *Project Timeline - Porthos*. https://www.porthosco2.nl/en/project/. Accessed: 2025-01-03.

[10] Haixia Wang, Jusheng Chen, and Qingling Li. “A review of pipeline transportation technology of carbon dioxide”. In: *IOP conference series: earth and environmental science*. Vol. 310. 3. IOP Publishing. 2019, p. 032033.

[11] Bjørn H Morland, Arne Dugstad, and Gaute Svenningsen. “Corrosion of carbon steel in dense phase CO2 with water above and below the solubility limit”. In: *Energy Procedia* 114 (2017), pp. 6752–6765.

[12] Kenneth René Simonsen, Dennis Severin Hansen, and Simon Pedersen. “Challenges in CO2 transportation: Trends and perspectives”. In: *Renewable and Sustainable Energy Reviews* 191 (2024), p. 114149.

[13] Lone Klinkby et al. “Simulating rapidly fluctuating CO2 flow into the Vedsted CO2 pipeline, injection well and reservoir”. In: *Energy Procedia* 4 (2011), pp. 4291–4298.

[14] Pamela Shirley and Paul Myles. *Quality guidelines for energy system studies: CO2 impurity design parameters*. Tech. rep. National Energy Technology Laboratory (NETL), Pittsburgh, PA, Morgantown, WV …, 2019.

[15] Emerson Automation Solutions. *Control Valve Flashing*. `https://www.emerson.com/en-sg/automation/valves/controlvalves/control-valve-flashing`. Accessed: 2025-07-18. 2025.

[16] Bob Fluttert. “A Numerical Study of the Behaviour of Carbon Dioxide in Control Valves for Optimising Carbon Sequestration”. Accessed: 2025-01-02. Master’s Thesis. Delft University of Technology, 2022. url: `https://repository.tudelft.nl/record/uuid:8db0c4bd-746b-48c5-9d6c-ed68e07843cd`.

[17] Victor E Onyebuchi et al. “A systematic review of key challenges of CO2 transport via pipelines”. In: *Renewable and Sustainable Energy Reviews* 81 (2018), pp. 2563–2583.

[18] Takakazu Suzuki et al. “Conceptual design of CO2 transportation system for CCS”. In: *Energy Procedia* 37 (2013), pp. 2989–2996.

[19] JR Roebuck, TA Murrell, and EE Miller. “The Joule-Thomson effect in carbon dioxide”. In: *Journal of the American Chemical Society* 64.2 (1942), pp. 400–411.

[20] SR De Groot and A Michels. “The Joule—Thomson effect and the specific heat at constant pressure of carbon dioxide”. In: *Physica* 14.4 (1948), pp. 218–222.

[21] Donna Price. “Thermodynamic Functions of Carbon Dioxide. Joule-Thomson Coefficient, Isochoric Heat Capacity, and Isentropic Behavior at 100° to 1000° C. and 50 to 1400 Bars”. In: *Industrial & Engineering Chemistry Chemical & Engineering Data Series* 1.1 (1956), pp. 83–86.

[22] Ding-Yu Peng and Donald B Robinson. “A new two-constant equation of state”. In: *Industrial & Engineering Chemistry Fundamentals* 15.1 (1976), pp. 59–64.

[23] Kenneth S Pitzer and S Michael Sterner. “Equations of state valid continuously from zero to extreme pressures for H2O and CO2”. In: *The Journal of chemical physics* 101.4 (1994), pp. 3111–3116.

[24] Roland Span and Wolfgang Wagner. “A new equation of state for carbon dioxide covering the fluid region from the triple-point temperature to 1100 K at pressures up to 800 MPa”. In: *Journal of physical and chemical reference data* 25.6 (1996), pp. 1509–1596.

[25] Alexandra Metallinou Log et al. “Depressurization of CO2 in a pipe: Effect of initial state on non-equilibrium two-phase flow”. In: *International Journal of Multiphase Flow* 170 (2024), p. 104624.

[26] Tatiana Flechas, Delphine M Laboureur, and Charles J Glover. “A 2-D CFD model for the decompression of carbon dioxide pipelines using the Peng-Robinson and the Span-Wagner equation of state”. In: *Process Safety and Environmental Protection* 140 (2020), pp. 299–313.

[27] Katherine Bartels and Adam Harmon. “Choked Flow in Control Valves”. In: *InTech* (Aug. 2021). url: https://www.isa.org/intech-home/2021/august-2021/departments/choked-flow-in-control-valves.

[28] Hong-Son Pham et al. “A numerical study of cavitation and bubble dynamics in liquid CO2 near the critical point”. In: *International Journal of Heat and Mass Transfer* 102 (2016), pp. 174–185.

[29] RM Pratt. “Thermodynamic properties involving derivatives using the Peng-Robinson equation of state”. In: *Chemical Engineering Education* 35.2 (2001), pp. 112–115.

[30] Tore FlÅtten, Alexandre Morin, and Svend Tollak Munkejord. “On solutions to equilibrium problems for systems of stiffened gases”. In: *SIAM Journal on Applied Mathematics* 71.1 (2011), pp. 41–67.

[31] Michael Colarossi et al. “Multidimensional modeling of condensing two-phase ejector flow”. In: *International journal of refrigeration* 35.2 (2012), pp. 290–299.

[32] Yu Fang et al. “An accurate and efficient look-up table equation of state for two-phase compressible flow simulations of carbon dioxide”. In: *Industrial & Engineering Chemistry Research* 57.22 (2018), pp. 7676–7691.

[33] Peter J Linstrom and William G Mallard. “The NIST Chemistry WebBook: A chemical data resource on the internet”. In: *Journal of Chemical & Engineering Data* 46.5 (2001), pp. 1059–1063.

[34] CLME Lettieri, DDME Yang, and ZZME Spakovszky. “An investigation of condensation effects in supercritical carbon dioxide compressors”. In: *Journal of Engineering for Gas Turbines and Power* 137.8 (2015), p. 082602.

[35] N Shamsundar and John H Lienhard. “Equations of state and spinodal lines—A review”. In: *Nuclear Engineering and Design* 141.1-2 (1993), pp. 269–287.

[36] STEFANO ZANZI. “Numerical simulation of condensing CO2 supersonic flows at high pressure”. In: (2017).

[37] Claudio Lettieri et al. “Characterization of nonequilibrium condensation of supercritical carbon dioxide in a de laval nozzle”. In: *Journal of Engineering for Gas Turbines and Power* 140.4 (2018), p. 041701.

[38] Alessandro Romei and Giacomo Persico. “Computational fluid-dynamic modelling of two-phase compressible flows of carbon dioxide in supercritical conditions”. In: *Applied Thermal Engineering* 190 (2021), p. 116816.

[39] Masafumi Nakagawa, Menandro Serrano Berana, and Akinori Kishine. “Supersonic two-phase flow of CO2 through converging–diverging nozzles for the ejector refrigeration cycle”. In: *International journal of refrigeration* 32.6 (2009), pp. 1195–1202.

[40] Marcelo Castier. “Thermodynamic speed of sound in multiphase systems”. In: *Fluid phase equilibria* 306.2 (2011), pp. 204–211.

[41] Marica Pelanti and Keh-Ming Shyue. “A numerical model for multiphase liquid–vapor–gas flows with interfaces and cavitation”. In: *International journal of multiphase flow* 113 (2019), pp. 208–230.

[42] Tore Flåtten and Halvor Lund. “Relaxation two-phase flow models and the subcharacteristic condition”. In: *Mathematical Models and Methods in Applied Sciences* 21.12 (2011), pp. 2379–2407.

[43] A. B. Wood. *A Textbook of Sound: Being an Account of the Physics of Vibrations with Special Reference to Recent Theoretical and Technical Developments*. New York: The Macmillan Company, 1941.

[44] Christopher E Brennen. “Fundamentals of Multiphase Flow”. In: *Cambridge Ltd* (2005).

[45] Masafumi Nakagawa, Menandro Serrano Serrano, and Atsushi Harada. “Shock waves in supersonic two-phase flow of CO2 in converging-diverging nozzles”. In: (2008).

[46] TNO - Rijswijk Centre for Sustainable Geo-energy (RCSG). *Innovate Geo-energy at RCSG*. Accessed: 2025-01-14. 2025. url: https://www.tno.nl/en/innovate-geo-energy-rcsg/?utm_medium=social&utm_content=video&utm_campaign=EMT-RCSG&utm_source=linkedin.

[47] V Babu. “Quasi One Dimensional Flows”. In: *Fundamentals of Gas Dynamics*. Springer, 2020, pp. 69–102.

[48] Marco De Lorenzo et al. “Benchmark of Delayed Equilibrium Model (DEM) and classic two-phase critical flow models against experimental data”. In: *International Journal of Multiphase Flow* 92 (2017), pp. 112–130.

[49] Michal Palacz et al. “Application range of the HEM approach for CO2 expansion inside two-phase ejectors for supermarket refrigeration systems”. In: *International Journal of Refrigeration* 59 (2015), pp. 251–258.

[50] ANSYS, Inc. *Ansys Fluent Theory Guide 2021 R2*. Available online: https://www.ansys.com. ANSYS, Inc. Canonsburg, PA, USA, 2021.

[51] Yafei Li and Jianqiang Deng. “Numerical investigation on the performance of transcritical CO2 two-phase ejector with a novel non-equilibrium CFD model”. In: *Energy* 238 (2022), p. 121995.

[52] Giuseppe Petruccelli et al. “Numerical Investigation of Two-Phase Shock Waves in CO2 Flows Using a Modified Hertz–Knudsen Model”. In: *Journal of Engineering for Gas Turbines and Power* 147.3 (2025).

[53] Guojie Zhang et al. “A novel carbon dioxide capture technology (CCT) based on non-equilibrium condensation characteristics: Numerical modelling, nozzle design and structure optimization”. In: *Energy* 286 (2024), p. 129603.

[54] Svend Tollak Munkejord et al. “Depressurization of CO2 in a pipe: High-resolution pressure and temperature data and comparison with model predictions”. In: *Energy* 211 (2020), p. 118560.

[55] Morten Hammer et al. “Experiments and modelling of choked flow of CO2 in orifices and nozzles”. In: *International Journal of Multiphase Flow* 156 (2022), p. 104201.

[56] James C Hesson and Ralph E Peck. “Flow of two-phase carbon dioxide through orifices”. In: *AIChE Journal* 4.2 (1958), pp. 207–210.

[57] Krzysztof Banasiak and Armin Hafner. “Mathematical modelling of supersonic two-phase R744 flows through converging–diverging nozzles: The effects of phase transition models”. In: *Applied Thermal Engineering* 51.1-2 (2013), pp. 635–643.

[58] Marco De Lorenzo. “Modelling and numerical simulation of metastable two-phase flows”. PhD thesis. Université Paris Saclay (COmUE), 2018.

[59] P Downar-Zapolski et al. “The non-equilibrium relaxation model for one-dimensional flashing liquid flow”. In: *International journal of multiphase flow* 22.3 (1996), pp. 473–483.

[60] Wojciech Angielczyk et al. “1-D modeling of supersonic carbon dioxide two-phase flow through ejector motive nozzle”. In: (2010).

[61] Antoine Metsue, Sébastien Poncet, and Yann Bartosiewicz. “A homogeneous relaxation model algorithm in density-based formulation with novel tabulated method for the modeling of CO2 flashing nozzles”. In: *International Journal of Refrigeration* 161 (2024), pp. 188–201.

[62] Øivind Wilhelmsen and Ailo Aasen. “Choked liquid flow in nozzles: Crossover from heterogeneous to homogeneous cavitation and insensitivity to depressurization rate”. In: *Chemical Engineering Science* 248 (2022), p. 117176.

[63] Alexandra Metallinou Log, Morten Hammer, and Svend Tollak Munkejord. “A flashing flow model for the rapid depressurization of CO2 in a pipe accounting for bubble nucleation and growth”. In: *International Journal of Multiphase Flow* 171 (2024), p. 104666.

[64] TS Shin and OC Jones. “Nucleation and flashing in nozzles—1. A distributed nucleation model”. In: *International journal of multiphase flow* 19.6 (1993), pp. 943–964.

[65] Mikko Manninen, Veikko Taivassalo, and Sirpa Kallio. “On the mixture model for multiphase flow”. In: (1996).

[66] James R Brock and R Byron Bird. “Surface tension and the principle of corresponding states”. In: *AIChE Journal* 1.2 (1955), pp. 174–177.

[67] Jeremiah U Brackbill, Douglas B Kothe, and Charles Zemach. “A continuum method for modeling surface tension”. In: *Journal of computational physics* 100.2 (1992), pp. 335–354.

[68] Florian R Menter. “Two-equation eddy-viscosity turbulence models for engineering applications”. In: *AIAA journal* 32.8 (1994), pp. 1598–1605.

[69] NASA Langley Research Center. *SST Turbulence Model*. `https://turbmodels.larc.nasa.gov/sst.html`. Accessed: 2025-04-25. 2025.

[70] Christopher E Brennen. *Cavitation and bubble dynamics*. Cambridge university press, 2014.

[71] Philip J Zwart, Andrew G Gerber, Thabet Belamri, et al. “A two-phase flow model for predicting cavitation dynamics”. In: *Fifth International Conference on Multiphase Flow.–Yokohama, Japan.–2004*. 2004.

[72] Limei Xu et al. “Relation between the Widom line and the dynamic crossover in systems with a liquid–liquid phase transition”. In: *Proceedings of the National Academy of Sciences* 102.46 (2005), pp. 16558–16562.

[73] DT Banuti, M Raju, and M Ihme. “Similarity law for Widom lines and coexistence lines”. In: *Physical Review E* 95.5 (2017), p. 052120.

[74] J-M Buchlin. “Industrial Two-phase Flow CFD, May 23-27, 2005”. In: *(No Title)* (2005).

[75] Francesco Giacomelli, Federico Mazzelli, and Adriano Milazzo. “A novel CFD approach for the computation of R744 flashing nozzles in compressible and metastable conditions”. In: *Energy* 162 (2018), pp. 1092–1105.

[76] Abraham Savitzky and Marcel JE Golay. “Smoothing and differentiation of data by simplified least squares procedures”. In: *Analytical Chemistry* 36.8 (1964), pp. 1627–1639.

[77] Maxwell Brunhart et al. “Investigation of cavitation and vapor shedding mechanisms in a Venturi nozzle”. In: *Physics of Fluids* 32.8 (2020).

[78] Wenyang Shao et al. “Accuracy study and stability control of a property-table-based CFD strategy for modeling SCO2 compressors working near the critical point of the fluid”. In: *Applied Thermal Engineering* 183 (2021), p. 116222.

A

Source Codes

This appendix presents the source code used for assigning the smoothed thermophysical properties from the lookup tables. Also, the source code for modelling the surface tension of CO_2 has been given in this Section.

Listing A.1: User-Defined Function for Thermophysical Property Assignment of Liquid Phase CO_2 in ANSYS Fluent Using REFPROP-Based Lookup Tables

```
1
2  /* User Defined Functions for Liquid Properties, Cp / H of Liquid and saturation / spinodal
       temperatures. Parameters defined here include the dimension of the LuT for saturation/
       spinodal line, the size of the CP/H LuT. The size of the liquid LuTs and the number of
       properties that need to be read from those LuTs (density, sound speed, viscosity and
       thermal conductivity)*/
3
4  #include "udf.h"
5  #define DIM_SAT_LUT 700
6  #define DIM_SPIN_LUT 700
7  #define NUM_SAT 5
8  #define DIM_CP_H_LUT 700
9  #define DISCR_PROPR_T 700
10 #define DISCR_PROPR_P 700
11 #define REF_ENTH_CO2 -3.935e8 / 44.00995 /* -3.935e8 * 44.00995/1000 Std state enthalpy in
       fluent times molecular weight / 1000 */
12 #define NUMPROP_LIQ 4
13
14 static real Tarr_liq [DISCR_PROPR_T];
15 static real Parr_liq [DISCR_PROPR_P];
16 static real prop_liq [NUMPROP_LIQ][DISCR_PROPR_T][DISCR_PROPR_P];
17 static real DT_liq, DP_liq, Pmin_liq, Pmax_liq, Tmin_liq, Tmax_liq;
18
```

```
/*Assuming Sat& Spin LuT have the same dimension, storing the relevant properties in a matrix*/


static real Parr_sat [NUM_SAT][DIM_SAT_LUT], Tarr_sat[NUM_SAT][DIM_SAT_LUT];
static real Ptr[NUM_SAT], Pcr[NUM_SAT], Ttr[NUM_SAT], Tcr[NUM_SAT], DP_sat[NUM_SAT], DT_sat[
    NUM_SAT];

static real Tarr_cp [DIM_CP_H_LUT];
static real propcp_liq [2][DIM_CP_H_LUT];
static real DT_cp, Tmin_cp, Tmax_cp;

char *namefile[NUMPROP_LIQ], *satname[NUM_SAT], *cpname, *Tname, *Pname;

real Interpolation(real P, real T,int index);

/* If variables are to be initialised and accessible by other macros, the 'on de 'mand macro
    must be used.
 Execute on loading was shown to be invalid and lead to errors - the de fine property macro
    could not handle the
 data initialisation. */

/* Operate a substitution of spin_clip with the desired string(wil_clip or sat_int for
    instance) to switch to the desired set
 of LuTs as generated by the ASCII_genscript */

DEFINE_ON_DEMAND(lutload)
{

int i, j, k;
FILE *Tpoint, *Ppoint, *Fpoint;
namefile [0] = ".\\lutsat_clip\\dens_l_sat_clip";
namefile [1] = ".\\lutsat_clip\\speed_l_sat_clip";
namefile [2] = ".\\lutsat_clip\\cond_l_sat_clip";
namefile [3] = ".\\lutsat_clip\\visco_l_sat_clip";
Tname = ".\\lutsat_clip\\temparr";
Pname = ".\\lutsat_clip\\pressarr";
satname [0] = "sat_lut";
satname [1] = "spin_lut";
satname [2] = "spinliq_lut";
satname [3] = "wilson_vap_lut";
satname [4] = "wilson_liq_lut";
cpname = "cp_h_liq_lut";

/*Reading T, P, LuT and assigning constants*/

Tpoint = fopen (Tname, "r+");
Ppoint = fopen (Pname, "r+");
```

```
if (Tpoint == NULL || Ppoint == NULL)
{ Error ("Could not reach T - P liquidarrays!"); }

for (i=0; i<DISCR_PROPR_T; i++)
    {fscanf (Tpoint, "%lf", &Tarr_liq [i]);}
fclose (Tpoint);

for (i=0; i<DISCR_PROPR_P; i++)
    {fscanf (Ppoint, "%lf", &Parr_liq [i]);}
fclose (Ppoint);

Message("T-P arrays loaded! \n");


Tmin_liq = Tarr_liq [0];
Pmin_liq = Parr_liq [0];
Tmax_liq = Tarr_liq [DISCR_PROPR_T - 1];
Pmax_liq = Parr_liq [DISCR_PROPR_P - 1];

Message("Tmin: %lf \n", Tmin_liq);
Message("Tmax: %lf \n", Tmax_liq);
Message("Pmin: %lf \n", Pmin_liq);
Message("Pmin: %lf \n", Pmax_liq);

for(k = 0; k < NUMPROP_LIQ; k++)
{
    Fpoint = fopen (namefile [k], "r+");
    if (Fpoint == NULL)
    {
        Error ("Could not reach %d LUT! \n", k);
    }
    for (i=0; i<DISCR_PROPR_T; i++)
    {
        for (j=0; j<DISCR_PROPR_P; j++)
        {
            fscanf (Fpoint, "%lf", &prop_liq [k][j][i]);
        }
    }
    fclose (Fpoint);
    Message("First element: %f \n", prop_liq[k][0][0]);
    Message("Last element : %f \n", prop_liq[k][DISCR_PROPR_P - 1][DISCR_PROPR_T - 1]);
    Message ("LuT %d loaded! \n", k);
}

Message ("Property LuT loading ended! \n");

/*SAT_LuT - SPIN_LuTload*/
```

```
for (i = 0; i < NUM_SAT; i++)
{
    Fpoint = fopen (satname [i], "r+");

    if (Fpoint == NULL)
    {
        Error ("'Couldnt find saturation LuT %d!", i);
    }

    for(j = 0; j<DIM_SAT_LUT; j++)
    {
        fscanf (Fpoint, "%lf", &Tarr_sat [i][j]);
    }

    for(j = 0; j<DIM_SAT_LUT; j++)
    {
        fscanf (Fpoint, "%lf", &Parr_sat [i][j]);
    }

    fclose (Fpoint);

    Ptr [i] = Parr_sat [i][0];
    Pcr [i] = Parr_sat [i][DIM_SAT_LUT - 1];
    Ttr [i] = Tarr_sat [i][0];
    Tcr [i] = Tarr_sat [i][DIM_SAT_LUT - 1];
    DP_sat [i] = Parr_sat [i][1] - Parr_sat [i][0];
    DT_sat [i] = Tarr_sat [i][1] - Tarr_sat [i][0];

    Message("P_trip: %lf \n", Ptr[i]);
    Message("P_crit: %lf  \n", Pcr[i]);
    Message("T_trip: %lf  \n", Ttr[i]);
    Message("T_crit: %lf  \n", Tcr[i]);
    Message("DP_sat: %lf  \n", DP_sat[i]);
    Message("DT_sat: %lf  \n", DT_sat[i]);

    Message ("Saturation LUT %d loaded! \n", i);
}

/*CP - H LuT load
Reading T, P, LuT and assigning constants*/

Fpoint = fopen (cpname, "r+");
if (Fpoint == NULL)
{
    Error ("Pointer could not reach CP-H LuT! \n");
}

```

```
for (i = 0; i < DIM_CP_H_LUT; i++)
{
    fscanf (Fpoint, "%lf", &Tarr_cp [i]);
}
    Message ("T array for CP LuT loaded!\n");
    Message("Tmin: %lf \n", Tarr_cp[0]);
    Message("Tmax: %lf \n", Tarr_cp[DIM_CP_H_LUT - 1]);

/*for (i = 0; i < 2; i++)
{*/
for (j = 0; j < DIM_CP_H_LUT; j++)
{
    fscanf(Fpoint, "%lf", &propcp_liq[0][j]);
}
    Message("CP lut loaded! \n");
    Message("First element: %f \n", propcp_liq[0][0]);
    Message("Last element : %f \n", propcp_liq[0][DIM_CP_H_LUT - 1]);

for (j = 0; j < DIM_CP_H_LUT; j++)
{
    fscanf(Fpoint, "%lf", &propcp_liq[1][j]);
}

    fclose(Fpoint);
    Message("H lut loaded! \n");
    Message("First element: %f \n", propcp_liq[1][0]);
    Message("Last element : %f \n", propcp_liq[1][DIM_CP_H_LUT - 1]);
/*}*/

DT_cp = Tarr_cp [1] - Tarr_cp [0];
Tmin_cp = Tarr_cp [0];
Tmax_cp = Tarr_cp [DIM_CP_H_LUT - 1];
}

int find_index_liq(double val, real* arr, int len) {
    int i;
    for (i = 0; i < len - 1; i++) {
        if (val >= arr[i] && val < arr[i + 1]) {
            return i;
        }
    }
    return len - 2; // clamp to valid range
}


/*Interpolationfunction*/
real Interpolation(real P, real T, int index)
```

```
{
    int indTlow, indThigh, indPlow, indPhigh;

    if (T <= Tarr_liq[0]) {
        indTlow = indThigh = 0;
    }
    else if (T >= Tarr_liq[DISCR_PROPR_T - 1]) {
        indTlow = indThigh = DISCR_PROPR_T - 1;
    }
    else {
        indTlow = find_index_liq(T, Tarr_liq, DISCR_PROPR_T);
        indThigh = indTlow + 1;
    }

    if (P <= Parr_liq[0]) {
        indPlow = indPhigh = 0;
    }
    else if (P >= Parr_liq[DISCR_PROPR_P - 1]) {
        indPlow = indPhigh = DISCR_PROPR_P - 1;
    }
    else {
        indPlow = find_index_liq(P, Parr_liq, DISCR_PROPR_P);
        indPhigh = indPlow + 1;
    }

    real Tlow = Tarr_liq[indTlow];
    real Thigh = Tarr_liq[indThigh];
    real Plow = Parr_liq[indPlow];
    real Phigh = Parr_liq[indPhigh];

    real A = prop_liq[index][indTlow][indPlow];
    real B = prop_liq[index][indThigh][indPlow];
    real C = prop_liq[index][indTlow][indPhigh];
    real D = prop_liq[index][indThigh][indPhigh];

    real f_Tlow, f_Thigh, Interpolated;

    if (indTlow == indThigh && indPlow == indPhigh) {
        Interpolated = A;
    }
    else if (indTlow == indThigh) {
        Interpolated = (Phigh - P) / (Phigh - Plow) * A + (P - Plow) / (Phigh - Plow) * C;
    }
    else if (indPlow == indPhigh) {
        Interpolated = (Thigh - T) / (Thigh - Tlow) * A + (T - Tlow) / (Thigh - Tlow) * B;
    }
    else {
```

```
249         f_Tlow = (Phigh - P) / (Phigh - Plow) * A + (P - Plow) / (Phigh - Plow) * C;
250         f_Thigh = (Phigh - P) / (Phigh - Plow) * B + (P - Plow) / (Phigh - Plow) * D;
251         Interpolated = (Thigh - T) / (Thigh - Tlow) * f_Tlow + (T - Tlow) / (Thigh - Tlow) *
        f_Thigh;
252     }
253
254     return Interpolated;
255 }
256
257
258 real Interpolation_sat (real press, int i)
259
260 {
261 real sattemp;
262
263 if (press < Ptr [i])
264 {   sattemp = Ttr [i]; }
265 else if (press > Pcr [i])
266 {   sattemp = Tcr [i]; }
267 else
268 {
269     int indPlow = floor ((press - Ptr [i]) / (DP_sat [i]));
270     int indPhigh = ceil ((press - Ptr [i]) / (DP_sat [i]));
271
272     if (indPlow == indPhigh)
273     {   sattemp = Tarr_sat [i][indPlow]; }
274     else
275     {
276     real Plow = Parr_sat [i][indPlow];
277     real Phigh = Parr_sat [i][indPhigh];
278     real Tlow = Tarr_sat [i][indPlow];
279     real Thigh = Tarr_sat [i][indPhigh];
280
281     sattemp = (press - Plow) / DP_sat[i] * Thigh + (Phigh - press) / DP_sat[i] * Tlow;
282     }
283 }
284 return sattemp;
285 }
286
287 real Interpolation_sat_cav(real temp, int i)
288
289 {
290     real satpress;
291
292     if (temp < Ttr[i])
293     {
294         satpress = Ptr[i];
```

```
    }
    else if (temp > Tcr[i])
    {
        satpress = Pcr[i];
    }
    else
    {
        int indTlow = floor((temp - Ttr[i]) / (DT_sat[i]));
        int indThigh = ceil((temp - Ttr[i]) / (DT_sat[i]));

        if (indTlow == indThigh)
        {
            satpress = Parr_sat[i][indTlow];
        }
        else
        {
            real Plow = Parr_sat[i][indTlow];
            real Phigh = Parr_sat[i][indThigh];
            real Tlow = Tarr_sat[i][indTlow];
            real Thigh = Tarr_sat[i][indThigh];

            satpress = (temp - Tlow) / DT_sat[i] * Phigh + (Thigh - temp) / DT_sat[i] * Plow;
        }
    }
    return satpress;
}

/*Defining properties for Liquid phase */

DEFINE_PROPERTY(LIQ_DENSITY, c, t)
{
int index = 0;
real Press_read = C_P(c,t);
real Temp_read = C_T(c,t);

real prop = Interpolation (Press_read, Temp_read, index);
return prop;
}

DEFINE_PROPERTY(LIQ_SSPEED, c, t)
{
int index = 1;
real Press_read = C_P(c,t);
real Temp_read = C_T(c,t);

real prop = Interpolation (Press_read, Temp_read, index);
return prop;
```

```
}

DEFINE_PROPERTY(LIQ_K, c, t)
{
int index = 2;
real Press_read = C_P(c,t);
real Temp_read = C_T(c,t);

real prop = Interpolation (Press_read, Temp_read, index);
return prop;
}

DEFINE_PROPERTY(LIQ_VISCO, c, t)
{
int index = 3;
real Press_read = C_P(c,t);
real Temp_read = C_T(c,t);

real prop = Interpolation (Press_read, Temp_read, index);
return prop;
}

DEFINE_SPECIFIC_HEAT(LIQ_CP, T, Tref, h, yi)
{
/* Interpolation section : must be carried out twice*/
int i, indTlow, indThigh;

if (T < Tmin_cp)
{   indTlow = 0;
    indThigh = 0;}
else if (T > Tmax_cp)
{   indTlow = DIM_CP_H_LUT - 1;
    indThigh = DIM_CP_H_LUT - 1; }
else
{   indTlow = floor((T - Tmin_cp) / DT_cp);
    indThigh = ceil((T - Tmin_cp) / DT_cp); }

real A, B;
real Tlow, Thigh;
real Interpolated [2];

Tlow = Tarr_cp [indTlow];
Thigh = Tarr_cp [indThigh];

/*Interpolation must be carried out twice : first gives CP, second gives absolute enthalpy
 Calculation of sensible enthalpy will be obtained through subtraction of a constant*/

```

```
for(i = 0; i < 2; i++)
{
    A = propcp_liq [i][indTlow];
    B = propcp_liq [i][indThigh];

/* Handling case where T might exactly be on the array->linear interpolation or no
    interpolation at all*/
    if (indTlow == indThigh)
    {
        Interpolated [i] = A;
    }
    else
    {   /*Standard: linear interpolation*/
        Interpolated [i] = (Thigh - T) / DT_cp * A + (T - Tlow) / DT_cp * B;
    }
}

*h = Interpolated [1] - REF_ENTH_CO2;


return Interpolated [0];
}

/*Defining properties for evaporation/condensation on temperature basis */

DEFINE_PROPERTY(SAT_TEMP, c, t)
{
    real press = C_P(c, t);
    int index = 0;
    real sattemp = Interpolation_sat(press, index);
    return sattemp;
}

DEFINE_PROPERTY(SPIN_TEMP, c, t)
{
    real press = C_P(c, t);
    int index = 1;
    real spintemp = Interpolation_sat(press, index);
    return spintemp;
}

DEFINE_PROPERTY(SPINLIQ_TEMP, c, t)
{
    real press = C_P(c, t);
    int index = 2;
    real spinliqtemp = Interpolation_sat(press, index);
    return spinliqtemp;
```

```
435 }
436
437 DEFINE_PROPERTY(WILSON_VAP_TEMP, c, t)
438 {
439     real press = C_P(c, t);
440     int index = 3;
441     real wiltemp = Interpolation_sat(press, index);
442     return wiltemp;
443 }
444
445 DEFINE_PROPERTY(WILSON_LIQ_TEMP, c, t)
446 {
447     real press = C_P(c, t);
448     int index = 4;
449     real williqtemp = Interpolation_sat(press, index);
450     return williqtemp;
451 }
452
453 /*Defining properties for cavitation on pressure basis */
454
455 DEFINE_PROPERTY(SAT_PRESS, c, t)
456 {
457     real temp = C_T(c, t);
458     int index = 0;
459     real satpress = Interpolation_sat_cav(temp, index);
460     return satpress;
461 }
462
463 DEFINE_PROPERTY(SPIN_PRESS, c, t)
464 {
465     real temp = C_T(c, t);
466     int index = 1;
467     real spinpress = Interpolation_sat_cav(temp, index);
468     return spinpress;
469 }
470
471 DEFINE_PROPERTY(SPINLIQ_PRESS, c, t)
472 {
473     real temp = C_T(c, t);
474     int index = 2;
475     real spinliqpress = Interpolation_sat_cav(temp, index);
476     return spinliqpress;
477 }
478
479 DEFINE_PROPERTY(WILSON_VAP_PRESS, c, t)
480 {
481     real temp = C_T(c, t);
```

```
482     int index = 3;
483     real wilpress = Interpolation_sat_cav(temp, index);
484     return wilpress;
485 }
486
487 DEFINE_PROPERTY(WILSON_LIQ_PRESS, c, t)
488 {
489     real temp = C_T(c, t);
490     int index = 4;
491     real williqpress = Interpolation_sat_cav(temp, index);
492     return williqpress;
493 }
```

Listing A.2: User Defined Real Gas Model (UDRGM) for Thermophysical Property Assignment of Vapour Phase CO_2 in ANSYS Fluent Using REFPROP-Based Lookup Tables

```
1
2  /*User Defined Real Gas Model for Real Gas Properties of Vapour Phase of CO2*/
3  /*
4   WindowsWarning!!! Including udf.h is for getting definitions for
5                     ANSYSFLUENT constructs such as Domain. You must
6                     NOT reference any ANSYSFLUENT globals directly from
7                     within this module nor link this against any ANSYS
8                     FLUENT libs, doing so will cause dependencies on a
9                     specific ANSYSFLUENT binary such as fl551.exe and
10                    thus 'wont be version independent.
11 */
12 #include "udf.h"
13 #include "stdio.h"
14 #include "ctype.h"
15 #include "stdarg.h"
16
17 /*
18 #if RP_DOUBLE
19 #define SMALL 1.e-20
20 #else
21 #define SMALL 1.e-10
22 #endif
23 */
24
25
26 /*Here the LuT size and number of properties is de fined (11 in total)*/
27 #define DISCR_T 700
28 #define DISCR_P 700
29 #define NUMPROP 11
30
31 static int (*usersMessage)(const char *,...);
32 static void (*usersError)(const char *,...);
```

```
33
34 /*Declaration of static variables, including pointer to array char for file paths sent as
       names to FOPEN*/
35 static double DT, DP, Tmin, Pmin, Tmax, Pmax;
36 static double properties [NUMPROP] [DISCR_T] [DISCR_P];
37 static double Tarr [DISCR_T];
38 static double Parr [DISCR_P];
39 static char *namefile [NUMPROP];
40 static char *Tname, *Pname;
41
42 double Interpolant(double T, double P, int index);
43
44
45 DEFINE_ON_DEMAND(I_do_nothing)
46 {
47 }
48
49 void CO2MONOLUT_error(int err, char *f, char *msg)
50 {
51     if (err)
52         usersError("CO2MONOLUT_error (%d) from function: %s\n%s\n" ,err,f,msg);
53 }
54
55 /* Operate a substitution of spin_clip with the desired string (wil_clip or sat_int for
       instance) to switch to the desired set
56  of LuTs as generated by the ASCII_genscript*/
57
58 void CO2MONOLUT_Setup(Domain *domain, cxboolean vapor_phase, char *species_list,
59     int(*messagefunc)(const char *format, ...),
60     void (*errorfunc)(const char *format, ...))
61 {   /*Use this function for any initialization or model setups*/
62     usersMessage = messagefunc;
63     usersError = errorfunc;
64     usersMessage("\nLoading spin_clip Library: %s\n", species_list);
65     namefile [0] = ".\\lutsat_clip\\dens_v_sat_clip";
66     namefile [1] = ".\\lutsat_clip\\cp_v_sat_clip";
67     namefile [2] = ".\\lutsat_clip\\enth_v_sat_clip";
68     namefile [3] = ".\\lutsat_clip\\entr_v_sat_clip";
69     namefile [4] = ".\\lutsat_clip\\speed_v_sat_clip";
70     namefile [5] = ".\\lutsat_clip\\visco_v_sat_clip";
71     namefile [6] = ".\\lutsat_clip\\cond_v_sat_clip";
72     namefile [7] = ".\\lutsat_clip\\rhot_v_sat_clip";
73     namefile [8] = ".\\lutsat_clip\\rhop_v_sat_clip";
74     namefile [9] = ".\\lutsat_clip\\entht_v_sat_clip";
75     namefile [10] = ".\\lutsat_clip\\enthp_v_sat_clip";
76     Tname = ".\\lutsat_clip\\temparr";
77     Pname = ".\\lutsat_clip\\pressarr";
```

```
78      FILE *Tpoint, *Ppoint, *Fpoint;
79      Tpoint = fopen (Tname, "r+");
80      Ppoint = fopen (Pname, "r+");
81
82      int i, j, q;
83
84      /*Reading T, P*/
85
86      for (i=0; i<DISCR_T; i++)
87          {fscanf (Tpoint, "%lf", &Tarr [i]);}
88          fclose (Tpoint);
89      for (i=0; i<DISCR_P; i++)
90          {fscanf (Ppoint, "%lf", &Parr [i]);}
91          fclose (Ppoint);
92
93      Message ("T and P arrays loaded \n");
94
95      Tmin = Tarr [0];
96      Pmin = Parr [0];
97      Tmax = Tarr [DISCR_T - 1];
98      Pmax = Parr [DISCR_P - 1];
99
100     Message("Tmin: %lf \n", Tmin);
101     Message("Tmax: %lf \n", Tmax);
102     Message("Pmin: %lf \n", Pmin);
103     Message("Pmin: %lf \n", Pmax);
104
105     /* Reading properties from ASCII tables*/
106     for(i=0; i<NUMPROP; i++)
107         {
108         Fpoint = fopen (namefile[i], "r+");
109         for(j=0; j<DISCR_T; j++)
110         {
111             for(q=0; q<DISCR_P; q++)
112             {
113                 fscanf (Fpoint, "%lf", &properties [i][q][j]);
114             }
115         }
116         Message("First element: %lf \n", properties[i][0][0]);
117         Message("Last element : %lf \n", properties[i][DISCR_P - 1][DISCR_T - 1]);
118         Message ("LuT %d loaded \n", i);
119         fclose (Fpoint);
120         }
121
122 }
123
124 /* NB position of function declaration must be BEFORE the function itself is called*/
```

```
125
126 int find_index(double val, double* arr, int len) {
127     int i;
128     for (i = 0; i < len - 1; i++) {
129         if (val >= arr[i] && val < arr[i + 1]) {
130             return i;
131         }
132     }
133     return len - 2; // fallback to last valid interval
134 }
135
136 double Interpolant(double T, double P, int index)
137 {
138     int indTlow, indThigh, indPlow, indPhigh;
139
140     if (T <= Tarr[0]) {
141         indTlow = indThigh = 0;
142     }
143     else if (T >= Tarr[DISCR_T - 1]) {
144         indTlow = indThigh = DISCR_T - 1;
145     }
146     else {
147         indTlow = find_index(T, Tarr, DISCR_T);
148         indThigh = indTlow + 1;
149     }
150
151     if (P <= Parr[0]) {
152         indPlow = indPhigh = 0;
153     }
154     else if (P >= Parr[DISCR_P - 1]) {
155         indPlow = indPhigh = DISCR_P - 1;
156     }
157     else {
158         indPlow = find_index(P, Parr, DISCR_P);
159         indPhigh = indPlow + 1;
160     }
161
162     double Tlow = Tarr[indTlow];
163     double Thigh = Tarr[indThigh];
164     double Plow = Parr[indPlow];
165     double Phigh = Parr[indPhigh];
166
167     double A = properties[index][indTlow][indPlow];
168     double B = properties[index][indThigh][indPlow];
169     double C = properties[index][indTlow][indPhigh];
170     double D = properties[index][indThigh][indPhigh];
171
```

```
    double f_Tlow, f_Thigh, result;

    if (indTlow == indThigh && indPlow == indPhigh) {
        result = A;
    }
    else if (indTlow == indThigh) {
        result = (Phigh - P) / (Phigh - Plow) * A + (P - Plow) / (Phigh - Plow) * C;
    }
    else if (indPlow == indPhigh) {
        result = (Thigh - T) / (Thigh - Tlow) * A + (T - Tlow) / (Thigh - Tlow) * B;
    }
    else {
        f_Tlow = (Phigh - P) / (Phigh - Plow) * A + (P - Plow) / (Phigh - Plow) * C;
        f_Thigh = (Phigh - P) / (Phigh - Plow) * B + (P - Plow) / (Phigh - Plow) * D;
        result = (Thigh - T) / (Thigh - Tlow) * f_Tlow + (T - Tlow) / (Thigh - Tlow) * f_Thigh;

    }


    return result;
}



double CO2MONOLUT_density (cell_t cell, Thread *thread, cxboolean vapor_phase, double T,
    double P, double yi[])
{
    int ind = 0;
    double r = Interpolant (T, P, ind);
    return r;/*(Kg/m^3)*/
}

double CO2MONOLUT_specific_heat(cell_t cell, Thread *thread, double T, double density, double
    P, double yi[])
{
    int ind = 1;
    double cp = Interpolant (T, P, ind);
    return cp; /*(J/Kg/K)*/
}

double CO2MONOLUT_enthalpy(cell_t cell, Thread *thread, double T, double density, double P,
    double yi[])
{
    int ind = 2;
    double h = Interpolant (T, P, ind);
    return h; /*(J/Kg)*/
}
```

```
215
216 double CO2MONOLUT_entropy(cell_t cell, Thread *thread, double T, double density, double P,
        double yi[])
217 {
218     int ind = 3;
219     double s = Interpolant (T, P, ind);
220     return s; /*(J/Kg/K)*/
221 }
222
223 double CO2MONOLUT_mw(double yi[])
224 {
225     double MW = 44.01;
226     return MW; /*(Kg/Kmol)*/
227 }
228
229 double CO2MONOLUT_speed_of_sound(cell_t cell, Thread *thread, double T, double density, double
         P, double yi[])
230 {
231     int ind = 4;
232     double a = Interpolant (T, P, ind);
233     return a; /*m/s*/
234 }
235
236 double CO2MONOLUT_viscosity(cell_t cell, Thread *thread, double T, double density, double P,
        double yi[])
237 {
238     int ind = 5;
239     double mu = Interpolant (T, P, ind);
240     return mu;  /*(Kg/m/s)*/
241 }
242
243 double CO2MONOLUT_thermal_conductivity(cell_t cell, Thread *thread, double T, double density,
        double P, double yi[])
244 {
245     int ind = 6;
246     double kt = Interpolant (T, P, ind);
247     return kt; /*W/m/K*/
248 }
249
250 double CO2MONOLUT_rho_t(cell_t cell, Thread *thread, double T, double density, double P,
        double yi[])
251 {
252     int ind = 7;
253     double drdT = Interpolant (T, P, ind);
254     return drdT; /*(Kg/m^3/K)*/
255 }
256
```

```
257 double CO2MONOLUT_rho_p(cell_t cell, Thread *thread, double T, double density, double P,
        double yi[])
258 {
259     int ind = 8;
260     double drdp = Interpolant (T, P, ind);
261     return drdp; /*(Kg/m^3/Pa)*/
262 }
263
264 double CO2MONOLUT_enthalpy_t(cell_t cell, Thread *thread, double T, double density, double P,
        double yi[])
265 {
266     int ind = 9;
267     double dhdT = Interpolant (T, P, ind);
268     return dhdT; /*J/(Kg.K)*/
269 }
270
271 double CO2MONOLUT_enthalpy_p (cell_t cell, Thread *thread, double T, double density, double P,
         double yi[])
272 {
273     int ind = 10;
274     double dhdp = Interpolant(T, P, ind);
275     return dhdp; /*J/(Kg.Pascal)*/
276 }
277
278 /*********************************************************************/
279 /*Auxiliary Mixture Functions*/
280 /*********************************************************************/
281
282 UDF_EXPORT RGAS_Functions RealGasFunctionList =
283 {
284     CO2MONOLUT_Setup,                   /*initialize*/
285     CO2MONOLUT_density,                 /*density*/
286     CO2MONOLUT_enthalpy,                /*enthalpy*/
287     CO2MONOLUT_entropy,                 /*entropy*/
288     CO2MONOLUT_specific_heat,           /*specific_heat*/
289     CO2MONOLUT_mw,                      /*molecular_weight*/
290     CO2MONOLUT_speed_of_sound,          /*speed_of_sound*/
291     CO2MONOLUT_viscosity,               /*viscosity*/
292     CO2MONOLUT_thermal_conductivity,    /*thermal_conductivity*/
293     CO2MONOLUT_rho_t,                   /*drho/dT|constp*/
294     CO2MONOLUT_rho_p,                   /*drho/dp|constT*/
295     CO2MONOLUT_enthalpy_t,              /*dh/dT|constp*/
296     CO2MONOLUT_enthalpy_p               /*dh/dp|constT*/
297 };
298 /*********************************************************************/
```

Listing A.3: User Defined Function (UDF) for surface tension of CO_2 in ANSYS Fluent using Brock Bird Surface Tension Model

```

#include "udf.h"
#include <math.h>

/* Brock & Bird Surface Tension Model */

/* Defining critical properties */
#define Pc_CO2   7.3773e6     /* Pa      */
#define Tc_CO2   304.1282     /* K       */
#define vc_CO2   2.15e-3     /* m^3/kg  */

/* Defining the values of gas constant */
#define R_univ   8.314462618 /* J/(mol.K) */
#define M_CO2    44.009e-3    /* kg/mol  */
#define R_CO2    (R_univ/M_CO2) /* J/(kg.K) */

/* Calculation of critical compressibilty factor */
#define Zc_CO2   (Pc_CO2 * vc_CO2 / (R_CO2 * Tc_CO2))

/* Exracting the cell temperature and calculating the corresponding reduced temperature value
    */
DEFINE_PROPERTY(brock_bird_surface_tension, c, t)
{
    real T = C_T(c, t);
    real T_r = T / Tc_CO2; /* Reduced temperature */

    /* Checking if the cell is in critical or super-critical state */
    if (T_r >= 1.0)
    {
        /* Assuming a very small value to avoid division by zero */
        return 1.0e-6; /* Minimum value from experiment was 7.0e-5 N/m */
    }
    else
    {
        /* Brock & Bird surface tension equation */
        return (-0.951 + (0.432 / Zc_CO2)) * pow(1.0 - T_r, 11.0 / 9.0) * cbrt(Pc_CO2 * Pc_CO2
     * Tc_CO2);
    }
}
```

B

Normalised Root Mean Square Deviation Calculation for Smoothed Data

The Normalised Root Mean Square Deviation (NRMSD) quantifies how close the smoothed data remains to the original raw data. A low value of NRMSD indicates a close match between the raw and smoothed data, indicating preservation of physical accuracy. While the Root Mean Square Deviation (RMSD) quantifies the absolute difference between smoothed and original data, it is sensitive to the magnitude and units of the property being evaluated. In contrast, NRMSD expresses this deviation relative to the range of the original data, enabling scale-independent comparison across different thermodynamic properties. This makes NRMSD a more suitable metric for assessing smoothing performance in multi-property datasets

$$\text{NRMSD } [\%] = \frac{\sqrt{\frac{1}{N}\sum_{i=1}^{N}\left(x_i - \hat{x}_i\right)^2}}{\max(x) - \min(x)} \times 100 \tag{B.1}$$

where:

- x_i is the original (raw) *REFPROP* data value at index i
- $\hat{x}_i$ is the smoothed data value at the same index i
- N is the total number of data points
- $\max(x)$ and $\min(x)$ are the maximum and minimum values in the original data set

The calculated NRMSD values for the smoothed data corresponding to each window size and polynomial order combination is presented in the following tables.

Table B.1: NRMSD for Savitzky–Golay smoothing with the window size (w) and polynomial order (p) combination of (w=101,p=2), (w=101,p=3), (w=51,p=2), (w=51,p=3)

Property	(w=101, p=2) NRMSD [%]	(w=101, p=3) NRMSD [%]	(w=51, p=2) NRMSD [%]	(w=51, p=3) NRMSD [%]
Density, Vapour	3.35	3.35	2.35	2.35
Density, Liquid	1.32	1.32	0.87	0.87
Specific Enthalpy, Vapour (h)	2.49	2.49	1.74	1.74
Specific Enthalpy, Liquid (h)	1.14	1.14	0.76	0.76
Entropy, Vapour	2.20	2.20	1.49	1.49
Entropy, Liquid	1.21	1.21	0.78	0.78
C_p, Vapour	0.25	0.25	0.22	0.22
C_p, Liquid	0.50	0.50	0.44	0.44
Speed of Sound, Vapour	2.32	2.32	1.63	1.63
Speed of Sound, Liquid	0.58	0.58	0.32	0.32
Viscosity, Vapour	2.23	2.23	1.55	1.55
Viscosity, Liquid	0.61	0.61	0.28	0.28
Thermal Conductivity, Vapour	1.38	1.38	0.97	0.97
Thermal Conductivity, Liquid	1.28	1.28	1.01	1.01
$\frac{d\rho}{dT}$, Vapour	0.24	0.24	0.22	0.22
$\frac{d\rho}{dT}$, Liquid	0.61	0.61	0.53	0.53
$\frac{d\rho}{dP}$, Vapour	0.25	0.25	0.22	0.22
$\frac{d\rho}{dP}$, Liquid	0.55	0.55	0.48	0.48
$\frac{dh}{dT}$ @ const P, Vapour	0.25	0.25	0.22	0.22
$\frac{dh}{dT}$ @ const P, Liquid	0.50	0.50	0.44	0.44
$\frac{dh}{dP}$ @ const T, Vapour	0.25	0.25	0.23	0.23
$\frac{dh}{dP}$ @ const T, Liquid	0.45	0.45	0.40	0.40

Table B.2: NRMSD for Savitzky–Golay smoothing with the window size (w) and polynomial order (p) combination of (w=21,p=2), (w=21,p=3), (w=11,p=2), (w=11,p=3)

Property	(w=21, p=2) NRMSD [%]	(w=21, p=3) NRMSD [%]	(w=11, p=2) NRMSD [%]	(w=11, p=3) NRMSD [%]
Density, Vapour	1.49	1.49	1.06	1.06
Density, Liquid	0.53	0.53	0.37	0.37
Specific Enthalpy, Vapour (h)	1.10	1.10	0.78	0.78
Specific Enthalpy, Liquid (h)	0.47	0.47	0.33	0.33
Entropy, Vapour	0.91	0.91	0.63	0.63
Entropy, Liquid	0.45	0.45	0.30	0.30
C_p, Vapour	0.19	0.19	0.17	0.17
C_p, Liquid	0.35	0.35	0.29	0.29
Speed of Sound, Vapour	1.03	1.03	0.73	0.73
Speed of Sound, Liquid	0.18	0.18	0.12	0.12
Viscosity, Vapour	0.98	0.98	0.70	0.70
Viscosity, Liquid	0.13	0.13	0.09	0.09
Thermal Conductivity, Vapour	0.62	0.62	0.44	0.44
Thermal Conductivity, Liquid	0.70	0.70	0.52	0.52
$\frac{d\rho}{dT}$, Vapour	0.20	0.20	0.18	0.18
$\frac{d\rho}{dT}$, Liquid	0.42	0.42	0.34	0.34
$\frac{d\rho}{dP}$, Vapour	0.20	0.20	0.17	0.17
$\frac{d\rho}{dP}$, Liquid	0.38	0.38	0.31	0.31
$\frac{dh}{dT}$ @ const P, Vapour	0.19	0.19	0.17	0.17
$\frac{dh}{dT}$ @ const P, Liquid	0.35	0.35	0.29	0.29
$\frac{dh}{dP}$ @ const T, Vapour	0.20	0.20	0.17	0.17
$\frac{dh}{dP}$ @ const T, Liquid	0.32	0.32	0.27	0.27